Simula SpringerBriefs on Computing 20
Reports on Computational Physiology

Kimberly J. McCabe *Editor*

Computational Physiology

Simula Summer School 2024/2025 – Student Reports

simula

OPEN ACCESS

Springer

Simula SpringerBriefs on Computing

Reports on Computational Physiology

Volume 20

In 2016, Springer and Simula launched an Open Access series called the Simula SpringerBriefs on Computing. This series aims to provide concise introductions to the research areas in which Simula specializes: scientific computing, software engineering, communication systems, machine learning and cybersecurity. These books are written for graduate students, researchers, professionals and others who are keenly interested in the science of computing, and each volume presents a compact, state-of-the-art disciplinary overview and raises essential critical questions in the field.

Simula's focus on computational physiology has grown considerably over the last decade, with the development of multi-scale mathematical models of excitable tissues (brain and heart) that are becoming increasingly complex and accurate. This subseries represents a new branch of the SimulaSpringer Briefs that is specifically focused on computational physiology. Each volume in the series will introduce and explore one or more sub-fields of computational physiology, and present models and tools developed to address the fundamental research questions of the field. Whenever possible, the software used will be made publicly available.

By publishing the Simula SpringerBriefs on Computing and the sub-series on computational physiology, Simula Research Laboratory acts on its mandate of emphasizing research education. Books in the series are published by invitation from one of the editors, and authors interested in publishing in the series are encouraged to contact any member of the editorial board.

Kimberly J. McCabe
Editor

Computational Physiology

Simula Summer School 2024/2025 – Student Reports

simula

Springer

Editor
Kimberly J. McCabe
Simula Research Laboratory
Oslo, Norway

ISSN 2512-1677 ISSN 2512-1685 (electronic)
Simula SpringerBriefs on Computing
ISSN 2730-7735 ISSN 2730-7743 (electronic)
Reports on Computational Physiology
ISBN 978-3-032-28825-7 ISBN 978-3-032-28826-4 (eBook)
https://doi.org/10.1007/978-3-032-28826-4

This work was supported by Simula Research Laboratory.

This Springer imprint is published by the registered company Springer Nature Switzerland AG
The registered company address is: Gewerbestrasse 11, 6330 Cham, Switzerland

Series Foreword

The series *Simula SpringerBriefs on Computing* was established in 2016, with the aim of publishing compact introductions and state-of-the-art overviews of select fields in computing. Research is increasingly interdisciplinary, and students and experienced researchers both often face the need to learn the foundations, tools, and methods of a new field. This process can be demanding, and typically involves extensive reading of multidisciplinary publications with different notations, terminologies and styles of presentation. The briefs in this series are meant to ease the process by explaining important concepts and theories in a specific interdisciplinary field without assuming extensive disciplinary knowledge and by outlining open research challenges and posing critical questions in the field.

Simula has a major research program in computational physiology that includes a long and close collaboration with the University of California (UC) San Diego. To reflect this research focus, we established in 2020 a new subseries entitled *Simula Springer Briefs on Computing - Reports on Computational Physiology*. The subseries includes both introductory and advanced texts on select fields of computational physiology, designed to advance interdisciplinary scientific literacy and promote effective communication and collaboration in the field. This subseries is also the outlet for collections of reports from the annual Summer School in Computational Physiology, organized by Simula, University of Oslo, and UC San Diego. The school starts in June each year with students spending two weeks in Oslo learning the principles underlying mathematical models commonly used in studying the heart and the brain. During their stay in Oslo, students are assigned a research project to work on over the summer. In August, they travel to San Diego for another week of training and project work, and a final presentation of their findings. Every year, we have been impressed by the students' creativity and we often see results that could lead to a scientific publication. Starting with the 2021 edition of the summer school, we have taken the course one step further by having each team conclude their project with a scientific report that can pass rigorous peer review as a publication in this new series.

All items in the main series and the subseries are published within the SpringerOpen framework, as this will allow authors to use the series to publish

an initial version of their manuscript that could subsequently evolve into a full-scale book on a broader theme. Since the briefs are freely available online, the authors do not receive any direct income from the sales; however, remuneration is provided for every completed manuscript. Briefs are written on the basis of an invitation from a member of the editorial board.

Suggestions for possible topics are most welcome, and interested authors are encouraged to contact a member of the editorial board.

March 2023

Dr. Joakim Sundnes
sundnes@simula.no

Dr. Kimberly J. McCabe
kimberly@simula.no

Dr. Andrew McCulloch
amcculloch@ucsd.edu

Dr. Aslak Tveito
aslak@simula.no

Preface

Since 2014, we have organized an annual summer school in computational physiology. The school starts in June each year and the graduate students spend two weeks in Oslo learning the principles underlying mathematical models commonly used in studying the heart and the brain. At the end of their stay in Oslo, the students are assigned a research project to work on over the summer. In August the students travel to the University of California, San Diego to present their findings. Each year, we have been duly impressed by the students' progress and we have often seen that the results contain the rudiments of a scientific paper.

Starting in the 2021 edition of the summer school, we have taken the course one step further and aim to conclude every project with a scientific report that passes rigorous peer review as a publication in this new series called *Simula SpringerBriefs on Computing – reports on computational physiology*. The chapters in this SpringerBrief represent reports from both the 2024 and 2025 edition of the summer school.

One advantage of this course adjustment is that we have the opportunity to introduce students to scientific writing. To ensure the students get the best introduction in the shortest amount of time, we have commissioned a professional introduction to science communication by Nature. The students participate in a *Nature Masterclasses* workshop in order to strengthen skills in high quality scientific writing and publishing. The workshop is tailored to publications in the field of computational physiology and allows students to gather real-time feedback on their reports.

We would like to emphasise that the contributions in this series are brief reports based on the intensive research projects assigned during the summer school. Each report addresses a specific problem of importance in physiology and presents a succinct summary of the findings (8-15 pages). We do not require that results represent new scientific results; rather, they can reproduce or supplement earlier computational studies or experimental findings. The physiological question under consideration should be clearly formulated, the mathematical models should be defined in a manner readable by others at the same level of expertise, and the software used should, if possible, be made publicly available. All reports in this series are subjected to peer-review by other supervisors in the program.

We would like to express our gratitude for the very fruitful collaboration with Springer -Nature and in particular with Dr. Martin Peters, the Executive Editor for Mathematics, Computational Science and Engineering.

The editors of *Simula SpringerBriefs on Computing – Reports on Computational Physiology*:

Oslo, Norway
October 2025

Kimberly J McCabe
Andrew D McCulloch
Aslak Tveito
Joakim Sundnes

Acknowledgements

The Simula Summer School in Computational Physiology requires the support of many scientists contributing their time to give lectures and advise projects for the students. We would like to thank the lecturers and project advisors for their expertise and willing participation in the course: Brian Aguado, Hermenegild Arevalo, Jørgen Dokken, Andrew Edwards, Henrik Finsberg, Nickolas Forsch, Emmet Francis, Alessandro Gatti, Nicolai Haug, Zeinab Jahed, Vira Kravets, Christopher Lee, Mikkel Lepperød, Molly Maleckar, Maria Hernandez Mesa, Kimberly McCabe, Andrew McCulloch, Giulia Monopoli, Padmini Rangamani, Marie Rognes, Joakim Sundnes, Aslak Tveito, and Daniela Valdez-Jasso.

Administrative support for the school was provided by Kimberly McCabe, Nickolas Forsch, Rachel Thomas, Stian Engen, and Hanie Tampus. At UCSD, we received vital administrative support from Jennifer Stowe.

The Simula Summer School in Computational Physiology is supported through the Simula-UiO-UCSD Research PhD Training Programme (SUURPh), an endeavour funded by the Norwegian Ministry of Education and Research. Additional financial support is derived from SIMBER, an INTPART mobility grant from the Norwegian Research Council. The school also received funding from Digital Life Norway (DLN) to support student mobility.

Contents

Chapter 1
Sex-Specific Effects of Doxorubicin on Cardiac Electromechanical Function: A Simulation-Based Study

Hannah Zukowski, Jule Bender, Anna Qi, and Hermenegild Arevalo

Abstract Doxorubicin (DOX) is a common chemotherapeutic agent associated with cardiotoxicity, exhibiting sex-specific differences in response. This study used computational simulations to investigate the effects of DOX on ventricular myocyte excitation-contraction coupling in male and female populations. The simulations evaluated the effects of DOX on action potential duration (APD90), calcium transients, and contractile function. DOX had a similar effect on both the male and female population models; In the male model, DOX treatment increased APD90 by 31%, calcium transient relaxation time by 41%, and had no effect on peak intracellular calcium concentration. In the female model, DOX treatment increased APD90 by 32%, calcium transient relaxation time by 34%, and increased peak intracellular calcium concentration by 7%. Healthy simulation differences were observed, with the healthy female simulation showing an 84% higher peak calcium concentration, 13% longer relaxation time, and 7% prolonged APD90 compared to the healthy male simulation. The healthy male and female simulation differences may contribute to females' greater susceptibility to DOX-induced cardiotoxicity due to increased calcium loading. This suggests that sex-specific dosing or additional treatments could be necessary to reduce the risk of calcium overload and related dysfunctions, such as early afterdepolarizations, delayed afterdepolarizations, or apoptosis. Overall, the study underscores the importance of personalized, sex-specific treatment strategies in managing the cardiac effects of DOX in cancer therapy.

Hannah Zukowski
Department of Physiology and Membrane Biology, University of California Davis, USA

Jule Bender
Institute of Biomedical Engineering, Karlsruhe Institute of Technology (KIT), Germany

Anna Qi
Department of Bioengineering, University of California San Diego, USA

Hermenegild Arevalo (corresponding author)
Department of Computational Physiology, Simula Research Laboratory, Norway e-mail: hermenegild@simula.no

K. J. McCabe, *Computational Physiology*, Simula SpringerBriefs on Computing 20, https://doi.org/10.1007/978-3-032-28826-4_1

1.1 Introduction

Anthracyclines are among the most widely utilized chemotherapy drugs for treating various types of cancer in both pediatric and adult patients. Doxorubicin (DOX) is a frequently used chemotherapeutic agent and is classified as an essential cytotoxic medicine by the World Health Organization [1]. It is estimated that approximately 50-60% of cancer survivors have been treated with at least one anthracycline drug. However, anthracycline-induced cardiotoxicity (AIC) presents significant side effects, ranging from asymptomatic declines in cardiac function to heart failure. Chronic AIC leads to irreversible cardiomyopathy, arrhythmias, and eventual heart failure, posing a major clinical concern [2, 3, 4].

Sex is also a significant risk factor for doxorubicin induced cardiotoxicity; females are 1.9 times more likely to develop doxorubicin induced cardiotoxicity than males [5]. Female's heightened risk for cardiotoxicity may be attributed to several factors, including a higher percentage of body fat, which could lead to poor anthracycline absorption and consequently higher intra-cardiac concentrations. Additionally, sex-specific differences in the expression of the multidrug-resistance gene, which regulates cellular excretion of anthracyclines, and variations in anthracycline pharmacokinetics—such as lower clearance rates in females—may further contribute to this disparity. Moreover, there is evidence suggesting that females may have an increased susceptibility to myocardial damage from anthracyclines [5].

Though doxorubicin cardiotoxicity is a well-accepted condition, the variation in affected population's outcomes remains unclear. Individuals experience varying effects of doxorubicin-induced cardiotoxicity which may depend on factors such as age, sex, and genetic predispositions. There is a critical need to understand the variability in cardiotoxicity across different patient demographics in order to develop personalized treatment protocols, minimize the risk of severe cardiac side effects, and maximize the efficacy of anthracycline-based chemotherapy.

In this project, we aim to explore the effects of doxorubicin on ventricular myocyte excitation-contraction coupling, a fundamental process in cardiac function. Additionally, this study seeks to investigate the sex-specific differences in the response to doxorubicin, focusing on how these effects may vary between male and female populations at both the cellular and tissue scales. By addressing these questions, we hope to uncover preliminary insights into the differential impact of doxorubicin, which could inform more tailored therapeutic approaches to improve outcomes for patients undergoing treatment.

1.2 Methods

Ionic current and flux scaling factors derived from experimental data were applied to relevant currents to account for acute effects of doxorubicin and male and female populations [7, 8]. Simulations were conducted using the coupled electro-mechanics solver simcardems [6] for six different parameter setups. The effects of doxorubicin

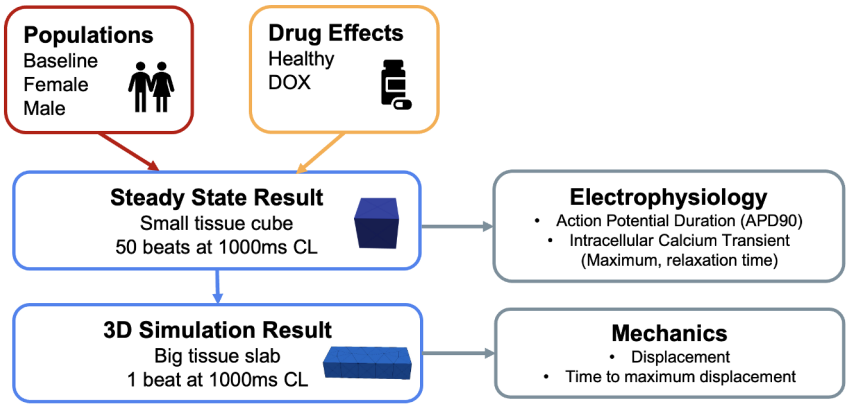

Fig. 1.1: Simulation setup. Healthy and doxorubicin (DOX) treated conditions were simulated for three population models (baseline, male, female) on a small tissue cube for 50 beats and one a larger tissue slab for 1 beat using simcardems [6]. Results of the steady state on the small tissue slab were used as initial values on the larger tissue slab. Action potential duration and intracellular calcium transient were analyzed at the center of the small tissue cube, contraction was analyzed on the large tissue slab. All simulations were performed at a cycle length (CL) of 1000ms.

were evaluated by analyzing action potential duration, intracellular calcium dynamics, and contractile function. A flowchart outlining the simulation process is provided in Figure 1.1.

1.2.1 Modeling Sex Differences and Doxorubicin

Doxorubicin scaling factors for *IRel*, *IUp*, *ICaL*, *INaCa*, *INaK*, *IKr*, and *ILeak* were selected based on consensus values derived from experimental data by Fernandez-Chaz et al. [7] and are presented in Table 1.1. To account for sex differences, scaling factors for *GNa, Gtos, GCaL, GKr, GKs, GK1, GNCX, PNaK, GKb, GpCa, GJup*, and *calm* for one female and one male model were included; both models were randomly selected from a larger cohort of population models by Llopis-Lorente et al. [8] (Table 1.2).

1.2.2 Electromechanical Simulations Using Simcardems

Simcardems is a cardiac electro-mechanics solver developed by Finsberg et. al. to study drug safety and efficacy [6]. The coupled cell model includes the O'Hara Rudy

model [9] for the electrophysiology and the Land model [10] for the mechanics and is implemented within the pre-existing FEniCS environment. Simulations were performed for all 6 models (*baseline-healthy, baseline-DOX, male-healthy, male-DOX, female-healthy, female-DOX*) over 50 beats at a cycle length of 1000ms to reach steady state on a small cube (1 nm × 1 nm × 1 nm, mechanics resolution: 1nm, electrophysiology resolution: 0.5nm). Initial values to conduct further simulations on a larger tissue slab (5 mm × 2 mm × 1 mm, mechanics resolution: 1mm, electrophysiology resolution: 0.5mm) for one beat at a cycle length of 1000ms for four models (*male-healthy, male-DOX, female-healthy, female-DOX*) were extracted from the last steady state beat on the small tissue cube.

1.2.3 Evaluation of Doxorubicin Induced Effects on Electrophysiology and Mechanics

The effects of doxorubicin on the action potential and the intracellular calcium transient were compared to experimental data at the center of the small tissue cube. Action potential duration was assessed at 90% repolarization, while intracellular calcium concentration was based on its peak value and the relaxation time was based on the time required to recover to 10% of the peak calcium concentration. Contraction was analyzed in terms of maximum displacement and time to maximum displacement at the center of the large tissue slab, as well as through time-series data.

	GNa	Gtos	GCaL	GKr	GKs	GK1	GNCX	PNaK	GKb	GpCa	GJup	calm
Male	1.438	1.348	0.846	0.864	1.058	1.063	1.025	0.302	0.800	0.971	0.959	1.050
Female	1.140	0.850	1.580	0.930	0.791	0.537	0.813	0.296	1.770	1.003	0.938	1.438

Table 1.1: Scaling factors for one male and one female population randomly chosen from larger population model cohort by Llopis-Lorente et al. [8]

	IRel	*IUp*	*ICaL*	*INaCa*	*INaK*	*IKr*	*SR ILeak Scalar*
DOX	+60%	-30%	+40%	-40%	-20%	-40%	2

Table 1.2: Scaling factors for doxorubicin from Fernandez-Chaz et al. [7]

1.3 Results

The female model exhibited longer APD90, higher peak calcium concentration, and longer calcium relaxation time compared to the male model (Figure 1.2 and Table 1.3). Doxorubicin increased APD90 and the relaxation time of the calcium transient in all models, while the maximum calcium concentration was only increased for the baseline and the female model (Figures 1.3, 1.4, 1.5). A similar relative increase in APD90 was observed for male and female when comparing doxorubicin and healthy conditions. However, for the calcium transient different concentrations could be observed for both models resulting in different peak concentrations. The relative increase in the maximum concentration was small for the female model when comparing doxorubicin and healthy, while no changes could be observed for the male model. Relative relaxation time for the calcium transient was higher for the female than the male model with 41% vs. 37% (Figure 1.4 and Figure 1.5). Contraction was slower (longer time to maximum displacement) and stronger (larger maximum displacement) for doxorubicin compared to healthy (Figure 1.6 and Table 1.3) in both models. The relative change for the maximum displacement in case of doxorubicin was higher for the female model compared to the male model (99% vs. 57%) whereas the relative change in the time to maximum displacement was higher for the male model than the female model (23% vs. 15%, Figure 1.7).

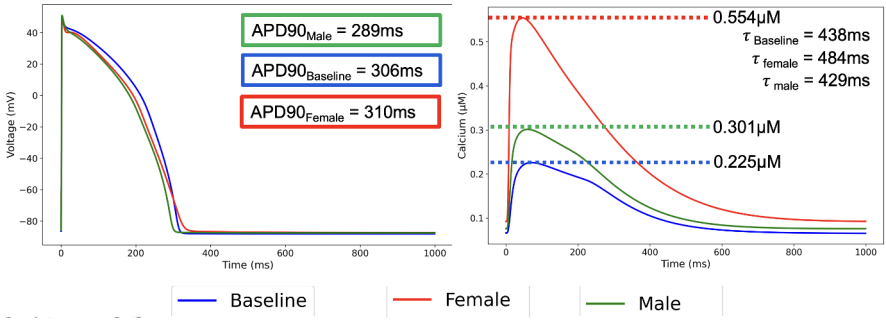

Fig. 1.2: Comparison of action potential (left) and calcium transient (right) across baseline (blue), male (green), and female (red) models, no drug effects included, values are extracted at center of small tissue slab at steady state. APD90 is prolonged for the female model compared to baseline, while it is reduced in the male model relative to baseline. Intracellular calcium concentration is higher for the female model relative to the male model, with both exceeding the baseline level. The relaxation time of the calcium transient τ is longest in the female model and shortest in the male model.

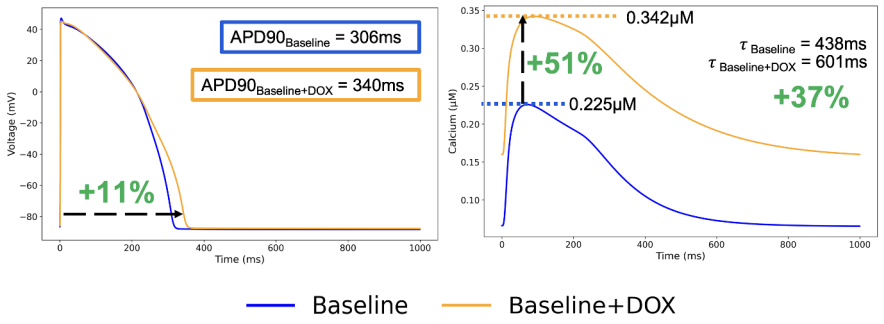

Fig. 1.3: Comparison of action potential (left) and calcium transient (right) for doxorubicin (DOX, yellow) and healthy (blue), no population factors included, values are extracted at the center of small tissue slab at steady state. Action potential duration as well as amplitude and relaxation time of calcium transient are increased for doxorubicin compared to baseline. APD90 is prolonged by 11%, maximum intracellular calcium concentration is increased by 51%, and calcium transient relaxation time τ is increased by 37% relative to the healthy model for doxorubicin.

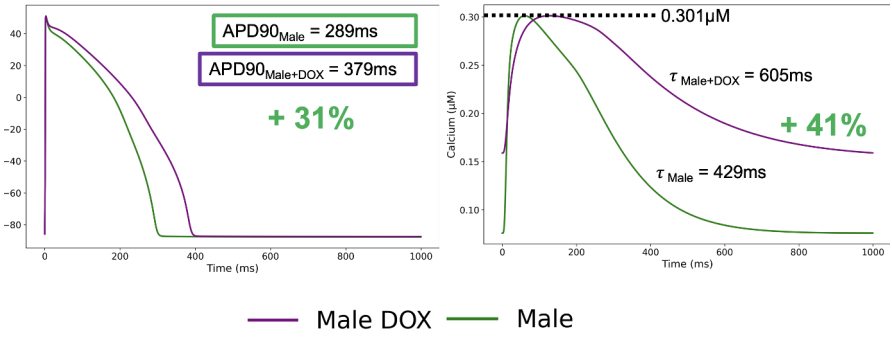

Fig. 1.4: Comparison of action potential (left) and calcium transient (right) for doxorubicin (purple) and healthy (green) for the male model, values are extracted at the center of small tissue slab at steady state. Both, action potential duration as well as the relaxation time of the calcium transient are increased for doxorubicin compared to healthy conditions. Maximum calcium concentration is similar in both models. APD90 is increased by 31% for doxorubicin compared to healthy, while calcium transient relaxation time τ is increased by 41% for doxorubicin relative to the healthy model.

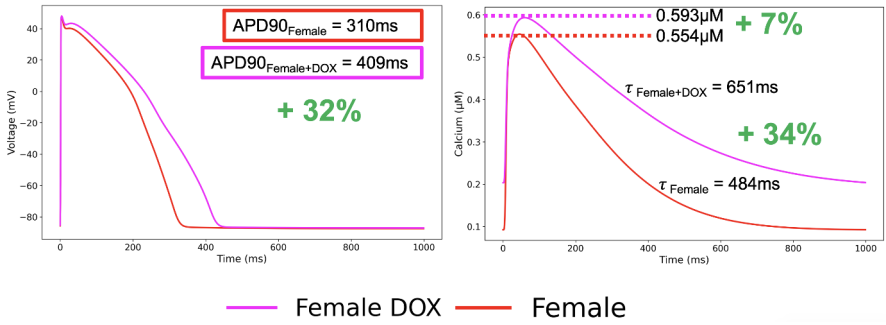

Fig. 1.5: Comparison of action potential (left) and calcium transient (right) for doxorubicin (pink) and healthy (red) for the female model, values are extracted at the center of small tissue slab at steady state. Action potential duration as well as relaxation time and maximum concentration of the calcium transient are increased for doxorubicin compared to healthy conditions. APD90 is prolonged by 32% for doxorubicin compared to healthy. The intracellular calcium concentration is 7% higher for doxorubicin relative to healthy. Relaxation time of the calcium transient τ is prolonged by 34% in case of doxorubicin compared to healthy to the healthy model.

	APD90	$[Ca^{2+}]_i$	$[Ca^{2+}]_i$ relaxation time
Healthy Baseline	306ms	0.225μM	438ms
DOX Baseline	340ms	0.342μM	601ms
% Change Baseline	+11%	+51%	+37%
Female Healthy	310ms	0.554μM	484ms
Female DOX	409ms	0.593μM	651ms
% Change Female	+32%	+7%	+34%
Male Healthy	289ms	0.301μM	429ms
Male DOX	379ms	0.301μM	605ms
% Change Male	+31%	+0%	+41%
% Change Paper Experimental	+31%	+52%	+30%

Table 1.3: Action potential duration (APD90), maximum intracellular calcium concentration ($[Ca^{2+}]_i$) and relaxation time for the calcium transient ($[Ca^{2+}]_i$ relaxation time) for all 6 simulated models (baseline-healthy, baseline-DOX, male-healthy, male-DOX, female-healthy, female-DOX) at the center of the tissue slab at steady state. Percent changes are calculated by comparing the healthy model to the DOX-treated model for baseline, male, and female conditions.

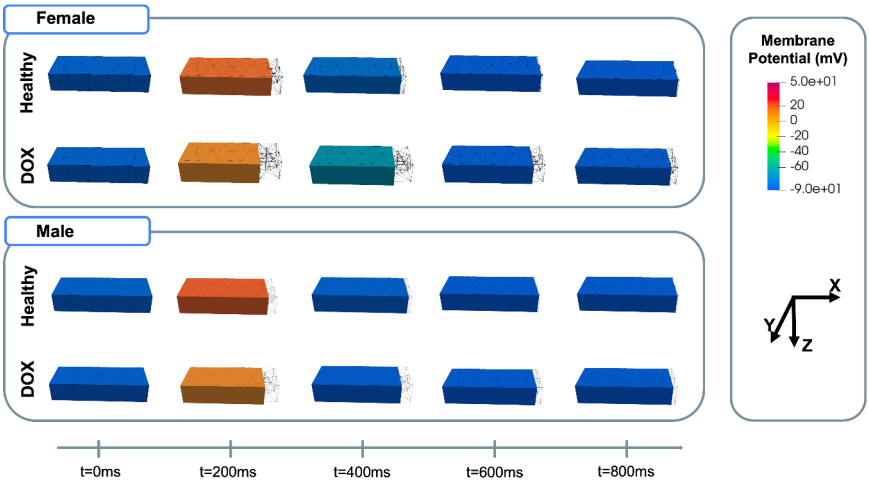

Fig. 1.6: Effects of doxorubicin (DOX) in the female model versus male model at tissue level. Maximum displacement in all three dimensions as well as the time to maximum displacement are increased for doxorubicin compared to healthy. In case of doxorubicin, the tissue is not completely relaxed when the next stimulus is applied. For the female model, maximum displacement was reached after 146ms in healthy conditions and after 168ms for doxorubicin (+15%). For the male model, maximum displacement was reached after 147ms in healthy conditions and after 181ms for doxorubicin (+23%). Maximum displacement in x direction was increased by 99% for the female model and by 57% for the male model in case of doxorubicin compared to healthy conditions.

1.4 Discussion

This study utilized an electro-mechanical solver to investigate the effects of doxorubicin on electro-mechanical coupling in male and female populations. In both male and female populations, doxorubicin treatment led to an increase in action potential duration at 90% repolarization (APD90) and calcium transients. Specifically, in the male simulation, DOX treatment increased APD90 by 31%, calcium transient relaxation time by 41%, and had no effect on peak intracellular calcium concentration (Figure 1.4). In the female model, DOX treatment increased APD90 by 32%, calcium transient relaxation time by 34%, and increased peak intracellular calcium concentration by 7% (Figure 1.5). The effects of doxorubicin were consistent between sexes, however, baseline electrophysiological differences between males and females were observed. Healthy female and male population simulations showed that compared to males, female peak calcium concentration is 84% higher, female relaxation time is 13% higher, and female APD90 is 7% longer (Figure 1.2). The higher baseline calcium levels in females may explain why they are more susceptible to doxorubicin-

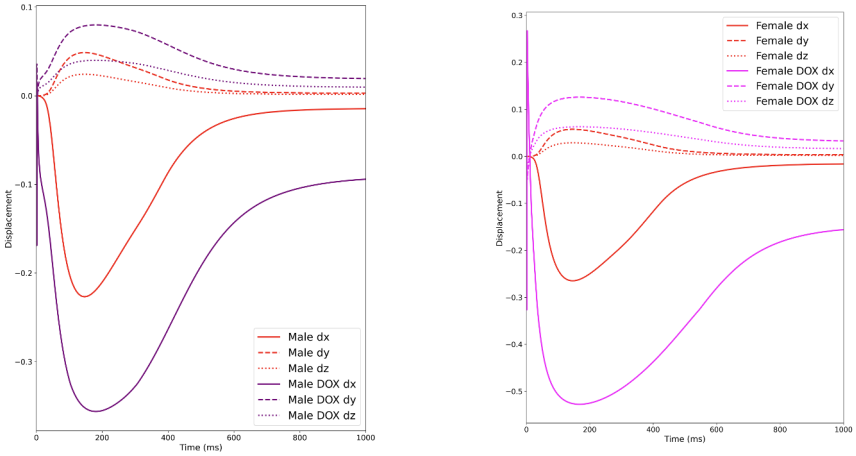

Fig. 1.7: Comparison of displacement in all three dimensions for the male model (left, DOX in purple and healthy in red) and female model (right, healthy in red and DOX in pink), all values are extracted at the center of the big tissue slab.

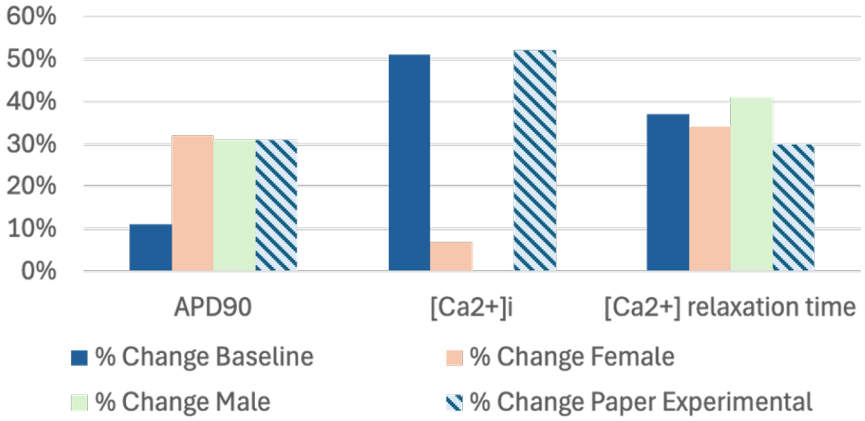

Fig. 1.8: Comparison of the effects of doxorubicin in the baseline (blue), female (orange), male (green), and experimental paper models (blue stripes) [7] at tissue level. The action potential duration at 90% repolarization (APD90), intracellular calcium concentration level ([Ca2+]i), and calcium relaxation time changes when introducing the effects of doxorubicin vs. healthy are compared. Simulation results for APD90 and relaxation time are consistent with experimental data for the male and female model whereas the peak calcium concentration is only consistent for the baseline model.

induced cardiotoxicity, as the increase in calcium transients in females results in an even higher overall calcium load. The inherent electrophysiological difference across populations suggests that women may require different dosing strategies or additional treatments to mitigate the risk of calcium overload and the associated dysfunctions in calcium regulation. Elevated intracellular calcium levels can lead to significant calcium handling dysfunctions, which are linked to further complications such as early afterdepolarizations, delayed afterdepolarizations, and even apoptosis in chronic cases [11].

Figure 1.8 illustrates the results from our study compared to available experimental data [7]. While the female and male simulation results for APD90 and calcium relaxation time are consistent with experimental findings, the peak calcium concentration does not align with the experimental data for the male and female population models (Figure 1.8). The discrepancy in peak intracellular concentration can be attributed to the doxorubicin scaling factors used in our model, which were adjusted to match the baseline case to experimental data, particularly by scaling the leak from the sarcoplasmic reticulum (SR). To improve the accuracy of our simulations with available experimental data, modifications to the SR calcium leak parameters in male and female population models would be necessary.

To the best of our knowledge, this in silico study is the first study analyzing the effects of doxorubicin at tissue level and the first study combining the effects of doxorubicin with sex-specific parameters. The different effects of doxorubicin on the female and male model in electrophysiology and mechanics show the need to consider sex when modeling drug effects. However, the study is limited in the use of only one male and one female randomly selected model. To better capture the biological variability in populations, future work should include additional male and female ionic profiles [8]. In addition, different pacing frequencies should be investigated to assess potential arrhythmogenic risks. Furthermore, simulations on larger tissue models with realistic geometries at whole-heart level are needed to ensure a comprehensive analysis. Overall, this study highlights the need to change the current one treatment fits all approach to more personalized treatments in the future in cancer therapy.

References

1. Jane Robertson, Ronald Barr, Lawrence N Shulman, Gilles B Forte, and Nicola Magrini. Essential medicines for cancer: WHO recommendations and national priorities. Bulletin of the World Health Organization, 94(10):735, 2016.
2. Yonghe Ding, Ke Du, Yu-Juan Niu, Yong Wang, and Xiaolei Xu. Genetic susceptibility and mechanisms underlying the pathogenesis of anthracycline-associated cardiotoxicity. Oxidative medicine and cellular longevity, 2022(1):5818612, 2022.
3. Kanu Chatterjee, Jianqing Zhang, Norman Honbo, and Joel S Karliner. Doxorubicin cardiomyopathy. Cardiology, 115(2):155–162, 2010.
4. Edward A Lefrak, Jan Pit'ha, Sidney Rosenheim, and Jeffrey A Gottlieb. A clinicopathologic analysis of adriamycin cardiotoxicity. Cancer, 32(2):302–314, 1973.
5. JP Krischer, DD Cuthbertson, S Epstein, AM Goorin, ML Epstein, and SE Lipshultz. Risk factors for early anthracycline clinical cardiotoxicity in children: the pediatric oncology group experience. Progress in pediatric cardiology, 8(2):83–90, 1997.
6. Henrik Nicolay Topnes Finsberg, Ilsbeth Gerarda Maria van Herck, Cécile Daversin-Catty, Hermenegild Arevalo, and Samuel Wall. simcardems: A fenics-based cardiac electromechanics solver. Journal of Open Source Software, 8(81):4753, 2023.
7. M Fernandez-Chas, MJ Curtis, and SA Niederer. Mechanism of doxorubicin cardiotoxicity evaluated by integrating multiple molecular effects into a biophysical model. British journal of pharmacology, 175(5):763–781, 2018.
8. Jordi Llopis-Lorente, Samuel Baroudi, Kévin Koloskoff, Maria Teresa Mora, Matthieu Basset, Lucía Romero, Sylvain Benito, Frederic Dayan, Javier Saiz, and Beatriz Trenor. Combining pharmacokinetic and electrophysiological models for early prediction of drug-induced arrhythmogenicity. Computer Methods and Programs in Biomedicine, 242:107860, 2023.
9. Thomas O'Hara, László Virág, András Varró, and Yoram Rudy. Simulation of the undiseased human cardiac ventricular action potential: model formulation and experimental validation. PLoS computational biology, 7(5):e1002061, 2011.
10. Sander Land, So-Jin Park-Holohan, Nicolas P Smith, Cristobal G Dos Remedios, Jonathan C Kentish, and Steven A Niederer. A model of cardiac contraction based on novel measurements of tension development in human cardiomyocytes. Journal of molecular and cellular cardiology, 106:68–83, 2017.
11. Stefan Wagner, Lars S Maier, and Donald M Bers. Role of sodium and calcium dysregulation in tachyarrhythmias in sudden cardiac death. Circulation research, 116(12):1956–1970, 2015.

Chapter 2
Biventricular Simulation Pipeline for Risk Stratification in Repaired Tetralogy of Fallot

Ali-Razak Rashid, Iulia Nazarov, Joachim Kröner, Niklas Tanger, Alessandro Gatti, and Hermenegild Arevalo

2.1 Abstract

Tetralogy of Fallot is the most common cyanotic congenital heart disease. The majority of patients survive into adulthood but most experience adverse cardiac events before the age of fifty. Effective risk stratification to identify the most vulnerable patients before an adverse event occurs remains a clinical challenge. Post-corrective surgery anatomy combined with age-related remodelling may lead to the formation of anatomic isthmuses. Conduction slowing within one or more of these isthmuses has been shown to be a cause of inducible ventricular tachycardia, one of the most predictive risk factors for this cohort of patients. Based on these observations, a meshing and simulation pipeline was developed to non-invasively assess vulnerability to reentry using conduction slowing within an isthmus. Simulation showed that reentry vulnerability increased as conduction velocity within the isthmus decreased. The pipeline was able to assess reentry risk even without induction. This pipeline may be developed and clinically validated to be used as a patient-specific method for assessing post-repair tetralogy of Fallot patients in adulthood.

Ali-Razak Rashid
Department of Biomedical Engineering and Imaging Sciences, King's College London, UK

Iulia Nazarov
Department of Biomedical Engineering and Imaging Sciences, King's College London, UK

Joachim Kröner
Department of Computer Science, University of Milan, Italy

Niklas Tanger
Cardiovascular Imaging and Dynamics, KU Leuven, Belgium

Alessandro Gatti
Department of Informatics, University of Oslo, Norway

Hermenegild Arevalo (corresponding author)
Department of Computational Physiology, Simula Research Laboratory, Norway e-mail: hermenegild@simula.no

All authors contributed equally to this work

K. J. McCabe, *Computational Physiology*, Simula SpringerBriefs on Computing 20, https://doi.org/10.1007/978-3-032-28826-4_2

2.2 Introduction

Tetralogy of Fallot (TOF) is the most common cyanotic congenital heart disease, affecting 0.34 per 1,000 live births [1, 2]. The four fundamental characteristics of TOF are: ventricular septal defect (VSD); right ventricular outflow tract (RVOT) obstruction; overriding of the aorta, where it is positioned directly superior to the VSD rather than the left ventricle (LV); and hypertrophy of the right ventricle (RV) [3, 4, 5]. The most common approach to surgical correction is by transannular patch (TAP) [6], requiring an incision from the main pulmonary artery to the infundibulum. Non-conducting patch material is placed to repair the VSD through right ventriculotomy, RV muscle bundles and pulmonary valve tissue are excised to relieve RVOT obstruction, and a transannular RVOT patch placed to close the ventriculotomy [7]. A preferable [8] yet less common approach is valve saving repair, whereby the VSD is accessed through a transatrial-transpulmonary procedure, sparing the pulmonary valve [7]. Preference for surgical approach is institutional and dependent on RVOT morphology, with cases with subvalvular obstruction requiring an infundibular patch regardless [9, 7]. Therefore, the outcome of the majority of corrective surgeries is a two-patch repair, with a VSD patch and an infundibular patch.

Medium-term outcomes post-surgery are excellent [10, 11, 12, 13, 14, 15], with up to 90% survival observed at 35-year follow-up [16, 17, 18]. Survival into mid-adulthood is positive, however, 44% of repaired TOF patients experience adverse cardiac events, such as ventricular tachycardia (VT) and sudden cardiac death (SCD), by the age of 50 [19]. Sustained VT has a 5-15% cumulative incidence at 35-year follow-up [20, 21], increasing with age, arrhythmic symptoms, and ventricular dysfunction [22], contributing to higher late mortality [23, 24]. The increase in VT risk and mortality is attributed to slow conduction through the characteristic anatomic isthmuses, which may form around the patch material [25, 26]. The most common isthmus, known as isthmus 3, is located between the VSD patch and pulmonary annulus and is almost universally present in TOF patients [27, 26, 5]. Slow conduction ($< 0.5 \text{ms}^{-1}$) through the anatomic isthmus is strongly associated with clinically inducible VT [28]. Inducible sustained VT results in an almost five-fold increased risk of SCD within a 6.5-year follow-up window [29, 30]. Heterogeneity in disease severity, progression, and outcome [31] necessitates effective risk stratification for identifying the patients that would most benefit from intervention.

Current risk stratification strategy utilises a number of non-invasive risk factors such as age, number of previous cardiac surgeries, QRS duration, QRS fragmentation, and biventricular systolic and diastolic dysfunction [32, 23, 20, 21, 24, 33, 22, 34]. Stratification of such a heterogeneous population is difficult and there is no universally accepted algorithm [31]. Many patients, particularly those at intermediate risk, have conflicting risk estimates and are difficult to effectively stratify with a general approach [35]. Personalised risk assessment via invasive electrophysiology (EP) study may be indicated in patients with multiple non-invasive risk factors [36]. Inducible sustained VT may be a useful risk factor [37], however the high prevalence of fast, poorly tolerated VT [38] and the risk of EP study complications [39] may

make this impractical. The current lack of personalised risk stratification contributes to premature death, inappropriate ICD implantation, and higher morbidity [40].

Motivated by the need for non-invasive personalised risk assessment, a biventricular simulation pipeline was developed to simulate invasive EP study for use in risk stratification algorithms. A refined instance of the mean TOF mesh from the Congenital Heart Disease Atlas (CHDA) from the Cardiac Atlas Project [41, 42] was used as a substitute for a patient-specific geometry. Fibre orientation was assigned to align with the fibre directions observed in autopsied TOF specimens [43]. A methodology was then developed to place VSD and infundibular patches onto the mesh, parametrised to allow for patient-specific patch sizes, geometries, and locations. A region to denote isthmus 3 was automatically tagged and assigned varying conduction velocities to emulate the remodelling and CV slowing observed clinically [25, 27, 28, 26]. Reentry risk quantitatively assessed using the reentry vulnerability index (RVI) [44].

2.3 Methods

The CHDA [42] provides meshes of approximately 1mm resolution, which is too coarse for physiological EP simulation [45]. To prepare a mesh for simulation, the mean TOF surface mesh was smoothed, isotropically refined to a finer resolution, and tetrahedralised. Smoothing and remeshing were performed using MeshLab [46]. Tetrahedralisation was performed using TetGen [47] version 0.6.7. Mesh regions were then tagged as healthy myocardium, VSD patch, RVOT patch, or isthmus 3, and assigned ionic and conduction properties for simulation. Six experiments were conducted, each with tuned conductivities assigned within isthmus 3 to target a different conduction velocity (CV). In each experiment, tissue was paced to a steady state, then single extra-stimulus pacing was used to calculate RVI. A visual overview of the meshing-simulation pipeline is shown in Figure 2.1.

2.3.1 Fibre Generation

Fibre orientations were generated on the coarse surface and volume meshes from the CHDA. Laplace-Dirichlet rule-based (LDRB) fibre generation [48] was used to assign fibre directions. These were visually inspected and adjusted to align with clinically observed ventricular myoarchitecture from autopsied TOF patients [43]. LDRB helical angles in the longitudinal direction were set at $\alpha_{endo} = 60°$ and $\alpha_{epi} = -60°$ for both LV and RV, and transverse fibre angles set to $\beta = 0°$ for both LV and RV [49, 50]. Fibre values generated from the coarse resolution mesh were interpolated onto the finer resolution mesh, with nearest-neighbour values used at mesh boundaries.

2.3.2 Mesh Smoothing and Refinement

Taubin smoothing [51] was used for non-shrinking mesh smoothing. Briefly, Gaussian filtering with a positive scale factor λ is applied to the mesh, which smooths and shrinks it. Subsequently, Gaussian filtering with a negative scale factor μ such that $\mu < -\lambda$ is then applied to inflate the mesh. These steps are repeated alternately to produce a smoothed mesh with minimal shrinkage. The smoothing parameter $\lambda = 0.5$ and the inflation parameter $\mu = -0.53$ were selected for all smoothing iterations and applied to all nodes uniformly.

An initial twenty Taubin smoothing steps were performed on the atlas surfaces. Mesh resolution was subsequently increased using ten isotropic explicit remeshing [52] iterations, with the initial five having a target edge length at the midpoint between the initial resolution and the target resolution, and the final five having a target edge length of the target resolution. After each of the five remeshing iterations, twenty additional Taubin smoothing steps were applied, producing the refined surface mesh. This was then tetrahedralised with a minimum radius-edge ratio of 1.5. The maximum tetrahedron volume V_{max} was calculated from the target edge length E_{target} : $V_{max} = (\sqrt{2}/12) \cdot E^3_{target}$. Tetrahedralising the refined surface mesh produced the refined volume mesh, which was tagged and used for simulations.

2.3.3 Mesh Tagging

The CobivecoX coordinate system [41] was used to delineate regions with distinct EP properties within the refined volume mesh. A ball with radius r around the specified coordinate point was used to define a region. RVOT patch was assigned at coordinates (tv, rt, ab, tm) = (1, 0.49, 0.86, 0.5) with r=15mm; VSD patch was assigned at coordinates (tv, rt, ab, tm) = (1, 0.66, 0.75, 0) with r =10mm; RV apex was assigned at coordinates (tv, ab, tm) = (1, 0, 1) with r =1mm for use in stimulation.

The isthmus 3 region was identified using previous literature [25, 26, 5]. It was tagged as the relative complement of the mesh nodes within both patches, with respect to a 9mm radius capsule which connects the point on the RV endocardium and the point on the pulmonary valve that are closest to the centre of the VSD patch. All elements not within the patches or isthmus 3 were tagged as healthy myocardium.

2.3.4 Electrophysiology

All simulations were monodomain [53], performed using openCARP [54] version 16 with 50μs time discretisation. The ten Tusscher-Panfilov [55] ionic model was pre-paced at a cycle length of 1000ms, with 2ms long 60mV transmembrane voltage stimuli, for 100 cycles to achieve limit cycle, verified by visual inspection. The resultant state vector was assigned homogeneously to all myocardial tissue. Conduc-

tivities were assigned by automatic tuning [56] to achieve a prescribed CV using tuneCV, part of the openCARP software package. Conductivities were tuned iteratively until the target CV with absolute error $< 0.001\text{ms}^{-1}$ was achieved. In healthy myocardium, longitudinal conductivity was assigned from tuning to a target CV of 0.6ms^{-1}, with transverse and normal conductivity assigned by tuning CVs to the anisotropy ratio 6:2:1 [57, 58].

Six experimental CVs were tuned for isthmus 3, with a longitudinal CV of 0.6ms^{-1} set as control. Longitudinal CVs were then tuned decreasing in 0.1ms^{-1} increments to a minimum of 0.1ms^{-1}; transverse and normal conductivities were tuned for each experiment to target CVs with anisotropy ratio 6:2:1. Non-conducting patch material was modelled as a hole in the mesh.

2.3.5 Stimulus and Pacing Protocol

Capture threshold and ventricular effective refractory period (VERP) were measured experimentally by brute force using a small cuboid mesh with healthy myocardial properties. Capture threshold was found by increasing stimulus current strength until capture, and VERP was found by increasing the S2 coupling interval until capture. Stimulation of the biventricular mesh was performed at the RV apex with a 2ms transmembrane current density of $51\mu\text{A/cm}^2$ (1.5 times capture threshold) applied from a 1mm diameter virtual electrode within the endocardium. For each experimental setup, seven S1 stimuli were delivered at 600ms cycle length to achieve tissue-level steady state, followed by the experimental S2 beat. S2 was a single extra-stimulus delivered at VERP+20ms [59, 60], measured to be 360ms.

2.3.6 Post-Processing

Simulation CV, the CV observed on the mesh during simulation using the tuned conductivities, was calculated using two methods. Isochronal local activation time (LAT) maps were used to calculate CV across the LAT map (CV_{LAT}) by dividing isochrone width in space with isochrone width in time. Localised CV was calculated over each tetrahedron element by taking the inverse LAT gradient over each finite element [61], giving the local CV as the wave passes over the element (CV_{local}).

To quantitatively assess risk from the simulation, the reentry vulnerability index (RVI) [44] was calculated using the S2 beat. RVI is the minimum difference between the proximal site's repolarisation time and the activation times of all distal sites within an 8mm radius. RVI therefore gives a measure of the excitable gap, with smaller numbers indicating a larger excitable gap, thus higher vulnerability to reentry. Minimum RVI values were compared across experimental setups to assess how reduced CV within isthmus 3 affects VT vulnerability, as defined by RVI.

2.3.7 Statistics

Normally distributed data are presented as mean±standard deviation (SD), with a range where appropriate. Margin of error was calculated using standard error of the mean (SEM) at 95% confidence. Units of the range and SEM are the same as the units given for the mean and SD. All statistics were calculated using the MATLAB (MathWorks) Statistics and Machine Learning Toolbox, version 24.2 (R2024b).

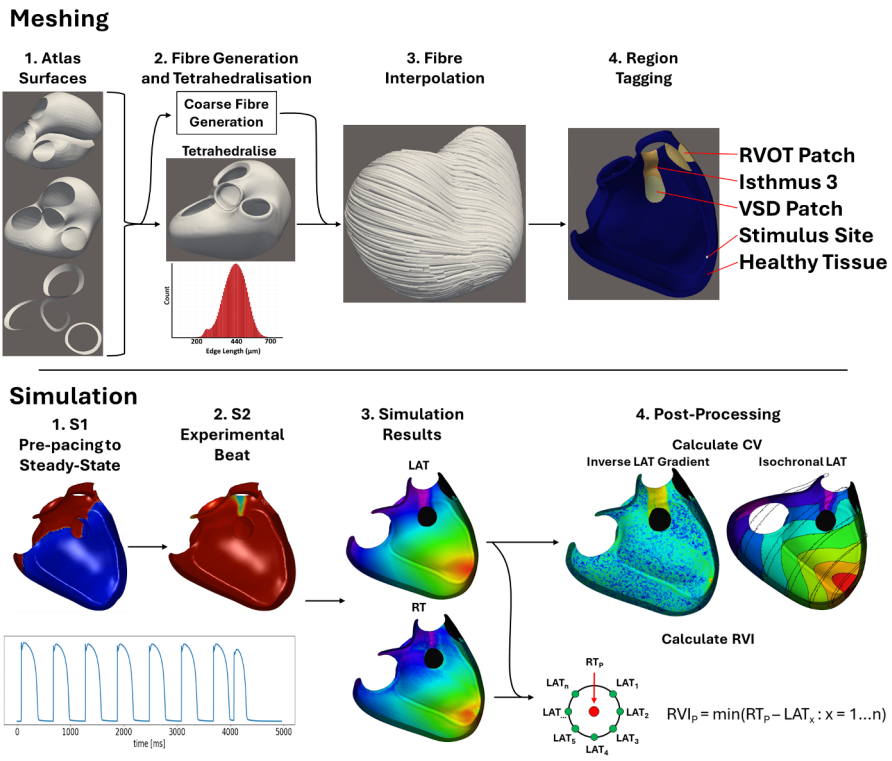

Fig. 2.1: Meshing and simulation pipeline, where the region tagged mesh is the input to the simulation pipeline. RVOT = right ventricular outflow tract; VSD = ventricular septal defect; LAT = local activation time; RT = repolarisation time; RVI = reentry vulnerability index.

2.4 Pipeline Evaluation

The mean TOF mesh was refined to a target resolution of 500μm. Actual mean edge length was 441±70.7μm, range 82.7-734. Tetrahedron target maximum volume $V_{max} = 14,731,391.3\mu m^3$, with actual mean tetrahedron $V = 8,094,750 \pm 2,437,600\mu m^3$, range 96,907-24,040,900.

Tuned conductivities (Table 2.1) gave accurate results within isthmus 3 measured by both CV_{LAT} and CV_{local} for a target CV≤0.4ms^{-1}. The conductivities no longer produced the target CV for target CVs >0.4ms^{-1}. Simulation CV in healthy myocardium (target CV of 0.6ms^{-1}) was similar for both CV measuring methods: average CV_{LAT} = 0.42±0.088ms^{-1} (SEM: ±0.0768 (±18.29%); average CV_{local} = 0.42±0.015ms^{-1} (SEM: ±0.0172 (±4.10%). Average isthmus 3 CV_{LAT} and CV_{local} were concordant with the target CV up to 0.4ms^{-1}. Above this, simulated CV remained at ≈0.42ms^{-1} regardless of conductivity increase. Minimum CV was 0ms^{-1} and maximum CV was 0.6ms^{-1} for each simulation, measured across every element.

Target CV	σ_{intra}, mS/cm	σ_{extra}, mS/cm	Tuned CV
0.01660	0.00910	0.07201	0.01650
0.03330	0.01175	0.09101	0.03320
0.05000	0.01330	0.09678	0.05050
0.06660	0.01883	0.09995	0.06660
0.08330	0.02201	0.13021	0.08330
0.10000	0.02410	0.25360	0.09990
0.13330	0.32600	0.29080	0.13370
0.16660	0.04220	0.32540	0.16590
0.20000	0.05645	0.28224	0.19910
0.30000	0.09501	0.47505	0.30000
0.40000	0.13980	0.69898	0.40010
0.50000	0.19040	0.95202	0.50010
0.60000	0.25764	1.03055	0.60040

Table 2.1: Target CVs and the resultant CV from the tuned intra- and extracellular conductivities. CV = conduction velocity; σ_{intra} = intracellular conductivity; σ_{extra} = extracellular conductivity.

Mean RVI was stable in healthy myocardium across all experiments. Within isthmus 3, mean RVI decreased with decreasing CV, remaining stable above 0.4ms^{-1}; minimum RVI decreased with all decreases in CV (Table 2.2). RVI maps showed decreasing RVI with slower CV within isthmus 3 (Figure 2.2).

Target CV (ms^{-1})	Tuned CV (ms^{-1})	Mean RVI, healthy (ms)	Mean RVI, isthmus 3 (ms)	Minimum RVI, isthmus 3 (ms)
0.1	0.0999	207 ± 11	171 ± 21	127
0.2	0.1991	207 ± 10	199 ± 12	166
0.3	0.3000	207 ± 10	209 ± 9	182
0.4	0.4001	207 ± 10	214 ± 7	192
0.5	0.5001	208 ± 10	216 ± 5	197
0.6	0.6004	208 ± 10	217 ± 4	202

Table 2.2: Mean RVIs for healthy and isthmus 3 tissue for each tuned longitudinal CV value within isthmus 3. Healthy tissue conductivity was uniformly set to target the tuned CV of 0.6004ms^{-1}. CV = conduction velocity; RVI = reentry vulnerability index.

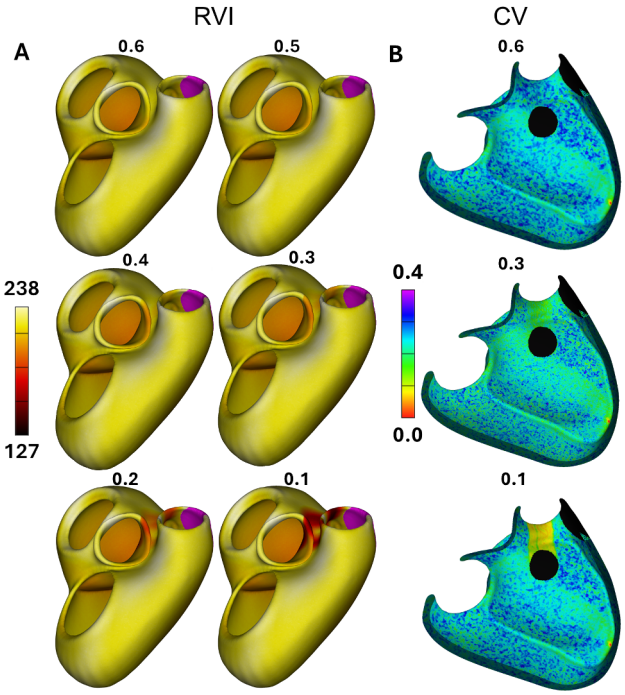

Fig. 2.2: **A)** RVI maps by target CV. Magenta region is the RVOT patch. Lower RVI indicates higher risk of reentry. **B)** Inverse LAT gradient method CV maps for target CVs 0.1ms^{-1}, 0.3ms^{-1}, and 0.6ms^{-1}. The black region is the VSD patch. Small region at the apex with 0 CV is the RV apex stimulus site. RVI = reentry vulnerability index; CV = conduction velocity.

2.5 Discussion

A meshing and simulation pipeline was developed for risk stratification of repaired tetralogy of Fallot patients using biventricular simulations. The mean TOF mesh from the CHDA was used for pipeline validation; however, input parameters to the meshing pipeline allow for a patient-specific mesh with individualised patch and isthmus locations and geometries. The preliminary simulation output shows that, with linear CV reduction within isthmus 3, RVI decreases superlinearly, with CVs closer to 0ms^{-1} (conduction block) producing increasingly lower RVI, indicating higher vulnerability.

RVI demonstrates promising potential for finer risk stratification in TOF patients, even when VT is non-inducible. Non-inducibility represents the majority of patients within this cohort [62], therefore a risk factor that can reflect the extent of vulnerability instead of a binary inducible or non-inducible may allow for finer and more personalised risk stratification scores. The calculation of RVI using simulation may allow for more frequent risk assessment as it is non-invasive thus can be performed without risk to the patient. RVI risk score is dependent on S2 coupling interval [63], however with the emeregence of more standardised programmed stimulation protocols [64] this can be controlled for, allowing for more standardised risk assessment. RVI can also be adequately adjusted using Bazett's correction to account for coupling interval [63].

More revision is necessary to make the simulations more physiological. CV_{LAT} and CV_{local} both indicate that CV within healthy myocardium was slower than the tuned CV, which may greatly impact risk assessment, especially in more heterogeneous circumstances. In addition to conductivities leading to correct CV, future improvements include the addition of a His-Purkinje network and the inclusion of endocardial, transmural, and epicardial heterogeneity. These would allow for validation of patient-specific EP using intra-cardiac mapping data or surface ECG matching. A realistic model that is validated to match a patient's clinical phenotype is essential for use of the model in risk assessment.

2.6 Acknowledgements

This work was partly supported by the Research Council of Norway. Simulations were performed on resources provided by Sigma2 - the National Infrastructure for High Performance Computing and Data Storage in Norway. Ali-Razak Rashid is funded by the EPSRC Research Council, part of the EPSRC DTP, Grant Ref: EP/W524475/1. Iulia Nazarov is supported by the CDT in Digital Twins for Healthcare, and the Wellcome/EPSRC Centre for Medical Engineering (WT203148/Z/16/Z). Joachim Kröner is supported by funding from the European Union's Horizon Europe programme under the Marie Sklodowska-Curie grant agreement No 101119941 (INSIDE-HEART). Niklas Tanger is funded by the KU Leuven internally funded project "Bayesian Inversion of Cardiac Electrograms for Patient Specific analysis (BICEPS)" IDN/22/006.

References

1. Denise van der Linde, Elisabeth E.M. Konings, Maarten A. Slager, Maarten Witsenburg, Willem A. Helbing, Johanna J.M. Takkenberg, and Jolien W. Roos-Hesselink. Birth prevalence of congenital heart disease worldwide. Journal of the American College of Cardiology, 58(21):2241–2247, November 2011.
2. Yingjuan Liu, Sen Chen, Liesl Zühlke, Graeme C Black, Mun-kit Choy, Ningxiu Li, and Bernard D Keavney. Global birth prevalence of congenital heart defects 1970–2017: updated systematic review and meta-analysis of 260 studies. International Journal of Epidemiology, 48(2):455–463, February 2019.
3. Maurice Lev and Friedrich A.O. Eckner. The pathologic anatomy of tetralogy of fallot and its variations. Diseases of the Chest, 45(3):251–261, March 1964.
4. Marie J. Béland, Rodney C. G. Franklin, Jeffrey P. Jacobs, Christo I. Tchervenkov, Vera D. Aiello, Steven D. Colan, J. William Gaynor, Otto N. Krogmann, Hiromi Kurosawa, Bohdan Maruszewski, Giovanni Stellin, and Paul M. Weinberg. Update from the international working group for mapping and coding of nomenclatures for paediatric and congenital heart disease. Cardiology in the Young, 14(2):225–229, April 2004.
5. Francis Bessière, Victor Waldmann, Nicolas Combes, Olivier Metton, Nabil Dib, Blandine Mondésert, Edward O'Leary, Elizabeth De Witt, Chrystalle Katte Carreon, Stephen P. Sanders, Jeremy P. Moore, John Triedman, and Paul Khairy. Ventricular arrhythmias in adults with congenital heart disease, part i. Journal of the American College of Cardiology, 82(11):1108–1120, September 2023.
6. Hamad F. Al Habib, Jeffrey Phillip Jacobs, Constantine Mavroudis, Christo I. Tchervenkov, Sean M. O'Brien, Siamak Mohammadi, and Marshall L. Jacobs. Contemporary patterns of management of tetralogy of fallot: Data from the society of thoracic surgeons database. The Annals of Thoracic Surgery, 90(3):813–820, September 2010.
7. Rachel D. Vanderlaan and David J. Barron. Optimal surgical management of tetralogy of fallot. CJC Pediatric and Congenital Heart Disease, 2(6):352–360, December 2023.
8. Samuel Blais, Ariane Marelli, Alain Vanasse, Nagib Dahdah, Adrian Dancea, Christian Drolet, and Frederic Dallaire. Comparison of long-term outcomes of valve-sparing and transannular patch procedures for correction of tetralogy of fallot. JAMA Network Open, 4(7):e2118141, July 2021.
9. Jacob R. Miller, Elizabeth H. Stephens, Andrew B. Goldstone, Andrew C. Glatz, Lauren Kane, Glen S. Van Arsdell, Giovanni Stellin, David J. Barron, Yves d'Udekem, Lee Benson, James Quintessenza, Richard G. Ohye, Sachin Talwar, Stephen E. Fremes, Sitaram M. Emani, and Pirooz Eghtesady. The american association for thoracic surgery (aats) 2022 expert consensus document: Management of infants and neonates with tetralogy of fallot. The Journal of Thoracic and Cardiovascular Surgery, 165(1):221–250, January 2023.
10. Tom R. Karl, Shunji Sano, Samphant Pornviliwan, and Roger B.B. Mee. Tetralogy of fallot: Favorable outcome of nonneonatal transatrial, transpulmonary repair. The Annals of Thoracic Surgery, 54(5):903–907, November 1992.
11. Andrew J Parry, Doff B McElhinney, Grace C Kung, V.Mohan Reddy, Michael M Brook, and Frank L Hanley. Elective primary repair of acyanotic tetralogy of fallot in early infancy: overall outcome and impact on the pulmonary valve. Journal of the American College of Cardiology, 36(7):2279–2283, December 2000.
12. Charles D Fraser, E.Dean McKenzie, and Denton A Cooley. Tetralogy of fallot: surgical management individualized to the patient. The Annals of Thoracic Surgery, 71(5):1556–1563, May 2001.
13. Robert D. Stewart, Carl L. Backer, Luciana Young, and Constantine Mavroudis. Tetralogy of fallot: Results of a pulmonary valve-sparing strategy. The Annals of Thoracic Surgery, 80(4):1431–1439, October 2005.
14. Linda W.G. Luijten, Eva van den Bosch, Nienke Duppen, Ronald Tanke, J. Roos-Hesselink, Aagje Nijveld, Arie van Dijk, Ad J.J.C. Bogers, Ron van Domburg, and Willem A. Helbing.

Long-term outcomes of transatrial–transpulmonary repair of tetralogy of fallot. European Journal of Cardio-Thoracic Surgery, 47(3):527–534, May 2014.
15. Clayton A. Smith, Courtney McCracken, Amanda S. Thomas, Logan G. Spector, James D. St Louis, Matthew E. Oster, James H. Moller, and Lazaros Kochilas. Long-term outcomes of tetralogy of fallot: A study from the pediatric cardiac care consortium. JAMA Cardiology, 4(1):34, January 2019.
16. Georg Nollert, Teddy Fischlein, Stefan Bouterwek, Christine Böhmer, Werner Klinner, and Bruno Reichart. Long-term survival in patients with repair of tetralogy of fallot: 36-year follow-up of 490 survivors of the first year after surgical repair. Journal of the American College of Cardiology, 30(5):1374–1383, November 1997.
17. Edward J. Hickey, Gruschen Veldtman, Timothy J. Bradley, Aungkana Gengsakul, Cedric Manlhiot, William G. Williams, Gary D. Webb, and Brian W. McCrindle. Late risk of outcomes for adults with repaired tetralogy of fallot from an inception cohort spanning four decades. European Journal of Cardio-Thoracic Surgery, 35(1):156–164, January 2009.
18. Yves d'Udekem, John C. Galati, Glenda J. Rolley, Igor E. Konstantinov, Robert G. Weintraub, Leeanne Grigg, James M. Ramsay, Gavin R. Wheaton, Sarah Hope, Michael H. Cheung, and Christian P. Brizard. Low risk of pulmonary valve implantation after a policy of transatrial repair of tetralogy of fallot delayed beyond the neonatal period. Journal of the American College of Cardiology, 63(6):563–568, February 2014.
19. Mark Dennis, Ben Moore, Irina Kotchetkova, Lynne Pressley, Rachael Cordina, and David S Celermajer. Adults with repaired tetralogy: low mortality but high morbidity up to middle age. Open Heart, 4(1):e000564, March 2017.
20. Paul Khairy, Jamil Aboulhosn, Michelle Z. Gurvitz, Alexander R. Opotowsky, Francois-Pierre Mongeon, Joseph Kay, Anne Marie Valente, Michael G. Earing, George Lui, Deborah R. Gersony, Stephen Cook, Jennifer Grando Ting, Michelle J. Nickolaus, Gary Webb, Michael J. Landzberg, and Craig S. Broberg. Arrhythmia burden in adults with surgically repaired tetralogy of fallot: A multi-institutional study. Circulation, 122(9):868–875, August 2010.
21. Judith A.A.E. Cuypers, Myrthe E. Menting, Elisabeth E.M. Konings, Petra Opić, Elisabeth M.W.J. Utens, Willem A. Helbing, Maarten Witsenburg, Annemien E. van den Bosch, Mohamed Ouhlous, Ron T. van Domburg, Dimitris Rizopoulos, Folkert J. Meijboom, Eric Boersma, Ad J.J.C. Bogers, and Jolien W. Roos-Hesselink. Unnatural history of tetralogy of fallot: Prospective follow-up of 40 years after surgical correction. Circulation, 130(22):1944–1953, November 2014.
22. Joseph Atallah, M. Cecilia Gonzalez Corcia, and Edward P. Walsh. Ventricular arrhythmia and life-threatening events in patients with repaired tetralogy of fallot. The American Journal of Cardiology, 132:126–132, October 2020.
23. Hiromichi Hamada, Masaru Terai, Toshiaki Jibiki, Tsunetaro Nakamura, Michael A. Gatzoulis, and Koichiro Niwa. Influence of early repair of tetralogy of fallot without an outflow patch on late arrhythmias and sudden death: a 27-year follow-up study following a uniform surgical approach. Cardiology in the Young, 12(4):345–351, July 2002.
24. Jouke P Bokma, Michiel M Winter, Jim T Vehmeijer, Hubert W Vliegen, Arie P van Dijk, Joost P van Melle, Folkert J Meijboom, Martijn C Post, Aeilko H Zwinderman, Barbara J M Mulder, and Berto J Bouma. Qrs fragmentation is superior to qrs duration in predicting mortality in adults with tetralogy of fallot. Heart, 103(9):666–671, November 2016.
25. Katja Zeppenfeld, Martin J. Schalij, Margot M. Bartelings, Usha B. Tedrow, Bruce A. Koplan, Kyoko Soejima, and William G. Stevenson. Catheter ablation of ventricular tachycardia after repair of congenital heart disease: Electroanatomic identification of the critical right ventricular isthmus. Circulation, 116(20):2241–2252, November 2007.
26. Gijsbert F L Kapel, Sergio Laranjo, Nico A Blom, Mark G Hazekamp, Martin J Schalij, Margot M Bartelings, Monique R M Jongbloed, and Katja Zeppenfeld. Impact of surgery on presence and dimensions of anatomical isthmuses in tetralogy of fallot. Heart, 104(14):1200–1207, January 2018.
27. Jeremy P. Moore, Atsuko Seki, Kevin M. Shannon, Ravi Mandapati, Roderick Tung, and Michael C. Fishbein. Characterization of anatomic ventricular tachycardia isthmus pathology

after surgical repair of tetralogy of fallot. Circulation: Arrhythmia and Electrophysiology, 6(5):905–911, October 2013.
28. Gijsbert F.L. Kapel, Frédéric Sacher, Olaf M. Dekkers, Masaya Watanabe, Nico A. Blom, Jean-Benoît Thambo, Nicolas Derval, Martin J. Schalij, Zakaria Jalal, Adrianus P. Wijnmaalen, and Katja Zeppenfeld. Arrhythmogenic anatomical isthmuses identified by electroanatomical mapping are the substrate for ventricular tachycardia in repaired tetralogy of fallot. European Heart Journal, page ehw202, May 2016.
29. Paul Khairy, Michael J. Landzberg, Michael A. Gatzoulis, Hugues Lucron, Jean Lambert, Francois Marcon, Mark E. Alexander, and Edward P. Walsh. Value of programmed ventricular stimulation after tetralogy of fallot repair: A multicenter study. Circulation, 109(16):1994–2000, April 2004.
30. Paul Khairy, Louise Harris, Michael J. Landzberg, Sangeetha Viswanathan, Amanda Barlow, Michael A. Gatzoulis, Susan M. Fernandes, Luc Beauchesne, Judith Therrien, Philippe Chetaille, Elaine Gordon, Isabelle Vonder Muhll, and Frank Cecchin. Implantable cardioverter-defibrillators in tetralogy of fallot. Circulation, 117(3):363–370, January 2008.
31. Eiad Habib, Komandoor Srivasthan, and Hicham El Masry. Evaluation and management of sudden death risk in repaired tetralogy of fallot. Journal of Personalized Medicine, 13(12):1715, December 2023.
32. Michael A Gatzoulis, Seshadri Balaji, Steven A Webber, Samuel C Siu, John S Hokanson, Christine Poile, Mark Rosenthal, Makoto Nakazawa, James H Moller, Paul C Gillette, Gary D Webb, and Andrew N Redington. Risk factors for arrhythmia and sudden cardiac death late after repair of tetralogy of fallot: a multicentre study. The Lancet, 356(9234):975–981, September 2000.
33. Mathias Possner, Stephanie Y. Tseng, Fares Alahdab, Jouke P. Bokma, Adam M. Lubert, Paul Khairy, M. Hassan Murad, Walid Ben Ali, Larry J. Prokop, Richard J. Czosek, Gruschen R. Veldtman, and Tarek Alsaied. Risk factors for mortality and ventricular tachycardia in patients with repaired tetralogy of fallot: A systematic review and meta-analysis. Canadian Journal of Cardiology, 36(11):1815–1825, November 2020.
34. H. Baumgartner, P. Bonhoeffer, N. M. S. De Groot, F. de Haan, J. E. Deanfield, N. Galie, M. A. Gatzoulis, C. Gohlke-Baerwolf, H. Kaemmerer, P. Kilner, F. Meijboom, B. J. M. Mulder, E. Oechslin, J. M. Oliver, A. Serraf, A. Szatmari, E. Thaulow, P. R. Vouhe, E. Walma, A. Vahanian, A. Auricchio, J. Bax, C. Ceconi, V. Dean, G. Filippatos, C. Funck-Brentano, R. Hobbs, P. Kearney, T. McDonagh, B. A. Popescu, Z. Reiner, U. Sechtem, P. A. Sirnes, M. Tendera, P. Vardas, P. Widimsky, T. McDonagh, L. Swan, F. Andreotti, M. Beghetti, M. Borggrefe, A. Bozio, S. Brecker, W. Budts, J. Hess, R. Hirsch, G. Jondeau, J. Kokkonen, M. Kozelj, S. Kucukoglu, M. Laan, C. Lionis, I. Metreveli, P. Moons, P. G. Pieper, V. Pilossoff, J. Popelova, S. Price, J. Roos-Hesselink, M. S. Uva, P. Tornos, P. T. Trindade, H. Ukkonen, H. Walker, G. D. Webb, and J. Westby. Esc guidelines for the management of grown-up congenital heart disease (new version 2010): The task force on the management of grown-up congenital heart disease of the european society of cardiology (esc). European Heart Journal, 31(23):2915–2957, August 2010.
35. Jayant Kakarla, Nathan C. Denham, Ayako Ishikita, Erwin Oechslin, Rafael Alonso-Gonzalez, and Krishnakumar Nair. Risk stratification for sudden cardiac death in repaired tetralogy of fallot. CJC Pediatric and Congenital Heart Disease, 2(6):414–425, December 2023.
36. Eric V. Krieger, Katja Zeppenfeld, Elizabeth S. DeWitt, Valeria E. Duarte, Alexander C. Egbe, Christiane Haeffele, Kimberly Y. Lin, Melissa R. Robinson, Christy Sillman, and Shailendra Upadhyay. Arrhythmias in repaired tetralogy of fallot: A scientific statement from the american heart association. Circulation: Arrhythmia and Electrophysiology, 15(11), November 2022.
37. Paul Khairy, Michael J Silka, Jeremy P Moore, James A DiNardo, Jim T Vehmeijer, Mary N Sheppard, Alexander van de Bruaene, Marie-A Chaix, Margarita Brida, Benjamin M Moore, Maully J Shah, Blandine Mondésert, Seshadri Balaji, Michael A Gatzoulis, and Magalie Ladouceur. Sudden cardiac death in congenital heart disease. European Heart Journal, 43(22):2103–2115, March 2022.
38. Mikael Laredo, Guillaume Duthoit, Frédéric Sacher, Frédéric Anselme, Caroline Audinet, Francis Bessière, Pierre Bordachar, Abdeslam Bouzeman, Serge Boveda, Sok Sithikun Bun,

Morgane Chassignolle, Gaël Clerici, Antoine Da Costa, Maxime de Guillebon, Pascal Defaye, Nathalie Elbaz, Romain Eschalier, Fabrice Extramiana, Laurent Fauchier, Alexis Hermida, Estelle Gandjbakhch, Rodrigue Garcia, Jean-Baptiste Gourraud, Charles Guenancia, Benoit Guy-Moyat, Didier Irles, Laurence Iserin, François Jourda, Linda Koutbi, Fabien Labombarda, Magalie Ladouceur, Philippe Lagrange, Nicolas Lellouche, Jacques Mansourati, Christelle Marquié, Raphael Martins, Grégoire Massoulié, Amel Mathiron, Philippe Maury, Anne Messali, Antoine Milhem, Pierre Mondoly, Cédric Nguyen, Sandro Ninni, Jean Luc Pasquié, Bertrand Pierre, Penelope Pujadas, Jean-Marc Sellal, Jean-Benoit Thambo, Camille Walton, Pierre Winum, Cyril Zakine, Alexandre Zhao, Xavier Jouven, Nicolas Combes, Eloi Marijon, and Victor Waldmann. Rapid ventricular tachycardia in patients with tetralogy of fallot and implantable cardioverter-defibrillator: Insights from the dai-t4f nationwide registry. Heart Rhythm, 20(2):252–260, February 2023.

39. Connor P. Oates, Binaya Basyal, William Whang, Vivek Y. Reddy, and Jacob S. Koruth. Trends in safety of catheter-based electrophysiology procedures in the last 2 decades: A meta-analysis. Heart Rhythm, 21(9):1718–1726, September 2024.
40. Lisa Albertini, Satoshi Kawada, Krishnakumar Nair, and Louise Harris. Incidence and clinical predictors of early and late complications of implantable cardioverter-defibrillators in adults with congenital heart disease. Canadian Journal of Cardiology, 39(3):236–245, March 2023.
41. Lisa R Pankewitz, Kristian G Hustad, Sachin Govil, James C Perry, Sanjeet Hegde, Renxiang Tang, Jeffrey H Omens, Alistair A Young, Andrew D McCulloch, and Hermenegild J Arevalo. A universal biventricular coordinate system incorporating valve annuli: Validation in congenital heart disease. Medical Image Analysis, 93:103091, April 2024.
42. Lisa R Pankewitz, Kristian G Hustad, Sachin Govil, James C Perry, Sanjeet Hegde, Renxiang Tang, Jeffrey H Omens, Alistair A Young, Andrew D McCulloch, and Hermenegild J Arevalo. A universal biventricular coordinate system incorporating valve annuli: Validation in congenital heart, 2023.
43. D. Sanchez-Quintana, R. H. Anderson, and S. Y. Ho. Ventricular myoarchitecture in tetralogy of fallot. Heart, 76(3):280–286, September 1996.
44. Michele Orini, Adam J. Graham, Neil T. Srinivasan, Fernando O. Campos, Ben M. Hanson, Anthony Chow, Ross J. Hunter, Richard J. Schilling, Malcolm Finlay, Mark J. Earley, Simon Sporton, Mehul Dhinoja, Martin Lowe, Bradley Porter, Nicholas Child, Christopher A. Rinaldi, Jaswinder Gill, Martin Bishop, Peter Taggart, and Pier D. Lambiase. Evaluation of the reentry vulnerability index to predict ventricular tachycardia circuits using high-density contact mapping. Heart Rhythm, 17(4):576–583, April 2020.
45. Boyang Cao, Nan Zhang, Zhenyin Fu, Ruiqing Dong, Tan Chen, Weiguo Zhang, Lv Tong, Zefeng Wang, Mingxia Ma, Zhanchun Song, Fuzhi Pan, Jinghui Bai, Yongquan Wu, Dongdong Deng, and Ling Xia. Studying the influence of finite element mesh size on the accuracy of ventricular tachycardia simulation. Reviews in Cardiovascular Medicine, 24(12):351, December 2023.
46. Paolo Cignoni, Marco Callieri, Massimiliano Corsini, Matteo Dellepiane, Fabio Ganovelli, and Guido Ranzuglia. Meshlab: an open-source mesh processing tool, 2008.
47. Hang Si. Tetgen, a delaunay-based quality tetrahedral mesh generator. ACM Transactions on Mathematical Software, 41(2):1–36, February 2015.
48. J. D. Bayer, R. C. Blake, G. Plank, and N. A. Trayanova. A novel rule-based algorithm for assigning myocardial fiber orientation to computational heart models. Annals of Biomedical Engineering, 40(10):2243–2254, May 2012.
49. P. M. Nielsen, I. J. Le Grice, B. H. Smaill, and P. J. Hunter. Mathematical model of geometry and fibrous structure of the heart. American Journal of Physiology-Heart and Circulatory Physiology, 260(4):H1365–H1378, April 1991.
50. Flavio Fenton and Alain Karma. Vortex dynamics in three-dimensional continuous myocardium with fiber rotation: Filament instability and fibrillation. Chaos: An Interdisciplinary Journal of Nonlinear Science, 8(1):20–47, March 1998.
51. Gabriel Taubin. A signal processing approach to fair surface design. In Proceedings of the 22nd annual conference on Computer graphics and interactive techniques - SIGGRAPH '95, SIGGRAPH '95, page 351–358. ACM Press, 1995.

52. Mario Botsch and Leif Kobbelt. A remeshing approach to multiresolution modeling. In Proceedings of the 2004 Eurographics/ACM SIGGRAPH symposium on Geometry processing, SGP04, page 185–192. ACM, July 2004.
53. James P Keener and James Sneyd. Mathematical Physiology. Interdisciplinary applied mathematics. Springer, New York, NY, 2 edition, June 1998.
54. Gernot Plank, Axel Loewe, Aurel Neic, Christoph Augustin, Yung-Lin Huang, Matthias A.F. Gsell, Elias Karabelas, Mark Nothstein, Anton J. Prassl, Jorge Sánchez, Gunnar Seemann, and Edward J. Vigmond. The opencarp simulation environment for cardiac electrophysiology. Computer Methods and Programs in Biomedicine, 208:106223, September 2021.
55. K. H. W. J. ten Tusscher and A. V. Panfilov. Alternans and spiral breakup in a human ventricular tissue model. American Journal of Physiology-Heart and Circulatory Physiology, 291(3):H1088–H1100, September 2006.
56. Caroline Mendonca Costa, Elena Hoetzl, Bernardo Martins Rocha, Anton J Prassl, and Gernot Plank. Automatic parameterization strategy for cardiac electrophysiology simulations. Comput. Cardiol. (2010), 40:373–376, October 2013.
57. L Clerc. Directional differences of impulse spread in trabecular muscle from mammalian heart. The Journal of Physiology, 255(2):335–346, February 1976.
58. M. J. Schalij, W. J. Lammers, P. L. Rensma, and M. A. Allessie. Anisotropic conduction and reentry in perfused epicardium of rabbit left ventricle. American Journal of Physiology-Heart and Circulatory Physiology, 263(5):H1466–H1478, November 1992.
59. Nicholas Jackson, Sigfus Gizurarson, Karthik Viswanathan, Benjamin King, Stephane Massé, Marjan Kusha, Andreu Porta-Sanchez, John Roshan Jacob, Fakhar Khan, Moloy Das, Andrew C.T. Ha, Ali Pashaei, Edward Vigmond, Eugene Downar, and Kumaraswamy Nanthakumar. Decrement evoked potential mapping: Basis of a mechanistic strategy for ventricular tachycardia ablation. Circulation: Arrhythmia and Electrophysiology, 8(6):1433–1442, December 2015.
60. Andreu Porta-Sánchez, Nicholas Jackson, Peter Lukac, Steen Buus Kristiansen, Jan Moller Nielsen, Sigfus Gizurarson, Stéphane Massé, Christopher Labos, Karthik Viswanathan, Benjamin King, Andrew C.T. Ha, Eugene Downar, and Kumaraswamy Nanthakumar. Multicenter study of ischemic ventricular tachycardia ablation with decrement-evoked potential (deep) mapping with extra stimulus. JACC: Clinical Electrophysiology, 4(3):307–315, March 2018.
61. P.V. Bayly, B.H. KenKnight, J.M. Rogers, R.E. Hillsley, R.E. Ideker, and W.M. Smith. Estimation of conduction velocity vector fields from epicardial mapping data. IEEE Transactions on Biomedical Engineering, 45(5):563–571, May 1998.
62. Victor Waldmann, Francis Bessière, Kevin Gardey, Mohamed Bakloul, Emre Belli, Damien Bonnet, Anne-Solène Chaussade, Sarah Cohen, Hubert Delasnerie, Nabil Dib, Sylvie Di Filippo, Arnaud Dulac, Sébastien Hascoët, Roland Henaine, Laurence Iserin, Clément Karsenty, Magalie Ladouceur, Antoine Legendre, Sophie Malekzadeh-Milani, Mansour Mostefa Kara, Jelena Radojevic, Miarisoa Ratsimandresy, Eloi Marijon, Alice Maltret, Paul Khairy, and Nicolas Combes. Systematic electrophysiological study prior to pulmonary valve replacement in tetralogy of fallot: A prospective multicenter study. Circulation: Arrhythmia and Electrophysiology, 16(6), June 2023.
63. Michele Orini, Peter Taggart, Martin Hayward, and Pier Lambiase. Optimisation of the global re-entry vulnerability index to minimise cycle length dependency and prediction of ventricular arrhythmias during human epicardial sock mapping. In 2017 Computing in Cardiology Conference (CinC), CinC2017. Computing in Cardiology, September 2017.
64. L Herrador Galindo, J Francisco Pascual, A Santos Ortega, J Perez Rodon, B Benito, J Cantalapiedra Romero, M Bach Oller, J Maldonado, L Dos Subira, A Pijuan Domenech, B Miranda Barrio, V Gonzalez Fernandez, B Gordon Ramirez, I Ferreira Gonzalez, and N Rivas Ganadara. Evaluation of ventricular tachycardia inducibility after implementation of a standardized programmed ventricular stimulation protocol in patients with repaired tetralogy of fallot. European Heart Journal, 42, October 2021.

Chapter 3
A Statistical Shape Modeling Pipeline for Assessing Arrhythmic Risk in Mitral Valve Disease Patients

Ingvild Askim Adde, Eva Schuijt, Diana Vucevic, Nina Ziegenbein, Giulia Monopoli, Nickolas Forsch, and Molly Maleckar

Abstract Mitral valve prolapse (MVP) and mitral annular disjunction (MAD) are associated with ventricular arrhythmias and sudden cardiac death, but risk stratification remains challenging. We extended a statistical shape modeling pipeline to analyze left ventricle end-diastole (ED) geometry and systolic motion defined as the displacement between end-systole and end-diastole (ES-ED), in 91 patients with MVP/MAD. The first five ED modes explain around 90% of shape variability, while the first six motion modes explained around 80% of systolic motion variability. Significant associations with arrhythmia were identified for ED modes M1 (global size) and M2 (sphericity), and for motion modes M3 (circumferential contraction) and M6 (regional wall displacement). Importantly, sex-stratified analyses revealed additional significant associations. This pipeline demonstrates that shape and motion modes derived from principal component analysis can capture clinically relevant

Ingvild Askim Adde
School of Economics, Innovation and Technology, Kristiania University of Applied Sciences, Norway

Eva Schuijt
Department of Physiology, Maastricht University, The Netherlands

Diana Vucevic
Department of Bioengineering, University of California San Diego, USA

Nina Ziegenbein
Steno Diabetes Center Aarhus, Aarhus University Hospital, Denmark and Department of Public Health, Aarhus University, Denmark

Giulia Monopoli
Simula Research Laboratory, Oslo, Norway

Nickolas Forsch
Simula Research Laboratory, Oslo, Norway

Molly Maleckar (corresponding author)
Simula Research Laboratory, Oslo, Norway e-mail: mmaleck@simula.no

All authors contributed equally to this work

K. J. McCabe, *Computational Physiology*, Simula SpringerBriefs on Computing 20, https://doi.org/10.1007/978-3-032-28826-4_3

remodeling in MVP/MAD, offering a complementary approach for arrhythmic risk assessment.

3.1 Introduction

Cardiovascular disease remains the leading cause of death worldwide, with arrhythmic events contributing substantially to this burden [1]. Yet, predicting which individuals are at risk of arrhythmias continues to pose a major clinical challenge.

Mitral valve prolapse (MVP) is the most common valvular heart disease, affecting an estimated 2–3% of the general population [2]. Mitral annular disjunction (MAD) frequently coexists with MVP. Although many patients remain asymptomatic, a clinically important subset of individuals with MVP and/or MAD have increased arrhythmic risk, commonly referred to as arrhythmic mitral valve syndrome (AMVS). This includes ventricular arrhythmia and sudden cardiac death. However, the underlying mechanisms of AMVS are not yet fully understood, making it difficult to accurately assess the risk of these life-threatening events in affected patients.

MVP is characterized by abnormal leaflet motion, in which the mitral valve leaflets are excessively compliant and bow back into the left atrium during systole, giving the appearance of a "floppy" or arched shape. A displacement over 2 millimeters of the mitral leaflets beyond the mitral annulus is considered the official definition of MVP [2]. Diagnosis is primarily made using transthoracic echocardiogram, however, cardiac magnetic resonance (CMR) imaging has now emerged as an important noninvasive modality to characterize MVP [3]. While the etiology is often unknown, MVP can be inherited or associated to connective tissue disorders such as Marfan syndrome, Ehler-Danlos syndrome and Loeys-Dietz syndrome [2]. MAD, defined as systolic separation between the mitral annulus and the ventricular myocardium [4], frequently coexists with MVP, occurring in 20–58% of cases [2].

Several studies have demonstrated left ventricular remodeling in patients with MAD/MVP, revealing a spectrum of remodeling patterns [4, 5]. Histological analysis of sudden cardiac death victims with MVP, as well as late gadolinium enhancement on contrast-enhanced CMR images in MVP patients who have arrhythmia, have shown left ventricular fibrosis of the inferobasal wall and papillary muscles [6, 7, 8]. One of the hallmark features seen clinically in patients with MAD is a pattern known as 'curling', where the posterior mitral annulus shows an unusually pronounced downward shift during systole, giving the nearby myocardium a distinctive curved appearance on imaging [3, 2, 6].

There is a clinical hypothesis that this left ventricle (LV) structural remodeling may be associated with arrhythmic events by providing a substrate for electrical instability [8]. However, to capture these complex structural alterations associated with LV remodeling, traditional clinical metrics often do not suffice.

In previous work, statistical shape modeling was applied to three-dimensional (3D) CMR end-systole (ES) short-axis (SAX) frames from a cohort of MVP/MAD patients. After segmenting the images, this methodology generated 3D point clouds,

which were then used to perform statistical shape analysis. For this ES analysis, one mode was significantly different in patients who experienced any type of ventricular arrhythmia, aborted cardiac arrest (ACA), ventricular tachycardia (VT), or non-sustained ventricular tachycardia (nsVT) compared to those who did not. This mode represented a pattern of skewing and tilting of the left ventricle and explained 16% of the total variance among the cohort [9].

In our study, we further extend this approach by including end-diastole (ED) frames and analyzing systolic motion between ES and ED, with the aim to extract additional structural and mechanical information not captured from ES shape alone.

In the following sections, we present our clinical cohort data and describe the statistical shape modeling framework, including automatic segmentation of SAX CMR images, point cloud generation, and statistical shape analysis (SSA). We subsequently present the SSA-derived modes for ED and motion (ES-ED) and examine their correlation with clinical measurements.

3.2 Methods

In this project, we extend the work of Monopoli et al. [9] from the ES scenario to include ED frames and the motion analysis (ES-ED), following the approach of Farrar et al. [10]. Figure 3.1 provides an overview of the original framework. The method uses segmented LV myocardium, LV blood pool, and RV blood pool from CMR images as input (Figure 3.1A). The segmented data are then converted to 3D point clouds (Figure 3.1B), which are subsequently analyzed using SSA with principal component analysis (PCA) (Figure 3.1C). Below, we describe our dataset and provide a more detailed description of each step in the present framework. The code and workflow for this project is publicly available[1].

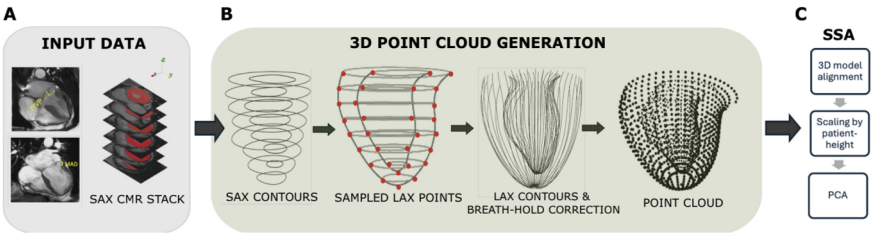

Fig. 3.1: Overview of the SSA pipeline. Segmented CMR images (A) are used as input to generate 3D point clouds (B), which are then subjected to PCA (C). Reprinted from Monopoli et. al [9].

[1] https://github.com/NinaZiegenbein/sscp25

3.2.1 Dataset

The dataset consists of CMR images from 91 patients with clinically confirmed MAD, of whom 75% had possible concomitant MVP [9]. The data was obtained from Oslo University Hospital in collaboration with the ProCardio Centre for Research-Based Innovation. The cohort includes 59 females and 32 males, aged 18 to 78 years. Each CMR dataset contained cine sequences in the SAX view, capturing a full cardiac cycle of approximately 30 frames per patient. In addition to imaging data, standard clinical measurements and disease status were available for each patient, providing complementary information. Additional details on the dataset are available in [11].

For each patient, we identified the frame showing maximal myocardial dilation as the ED frame through visual inspection of the SAX cine sequences. We excluded slices above the mitral valve plane and slices where the apex was not visible. Patients were classified as arrhythmic if they had experienced any of the following: ACA, VT, or nsVT. Out of the 91 patients, 14 patients were defined as arrhythmic (8 females and 6 males).

3.2.2 Segmentation of CMR images

We used the `ventricular_short_axis_3label` model created by MONAI [12] to automatically segment the LV myocardium, as well as the LV and right ventricle (RV) blood pools, in our CMR SAX images. The model is based on a U-Net architecture and has been trained on a private dataset from King's College London, mainly using ED frames [13]. The model requires images of size (256, 256) as input. Hence, we applied cropping and zero-padding when relevant to resize our images to the proper size. After running the model on our dataset, we verified the segmentations visually using *3D Slicer* [14]. Figure 3.2 shows an example of a successful segmentation using the MONAI model. In some rare cases, the segmentations were not satisfactory, particularly for the RV blood pool. These segmentations were corrected manually in *3D Slicer*.

3.2.3 3D point cloud generation

We employed the `saxomode` package [9] to generate 3D point clouds from the segmented data from section 3.2.2. The `saxomode` package automatically identifies the LV epicardial and endocardial boundaries based on the segmentation masks, and converts them to real-world coordinates using voxel dimensions [9]. Third-order B-splines were then applied to fit the coordinates, resulting in smooth endocardial and epicardial SAX contours. During B-spline fitting, a smoothing factor of

$$\frac{1}{N}\sum (y-g)^2 \leq s \tag{3.1}$$

was used to correct for SAX breath-hold misalignment. Here, $g(x)$ represents the smoothed interpolation, y represents the interpolated data, N is the total number of points, and s is the smoothing factor. All contours were visually inspected, and a higher smoothing factor was applied in scenarios wherein breath-hold misalignment from acquisition was pronounced. Each of the 20 resulting SAX planes was then sampled at 40 evenly distributed points, plus an additional apical point, resulting in a total of 1,602 data points per patient. Additional details regarding the point cloud generation can be found in [9].

To enable meaningful shape comparisons, the derived LV point clouds were aligned to a common anatomical coordinate system [9]. Specifically, each point cloud was translated so that the origin coincided with the geometric center of the LV epicardium (center-of-mass of the epicardial mask). The z-axis was defined along the imaging short-axis stack's longitudinal direction (approximating the LV base–apex axis). An orthogonal y-axis was then established pointing toward the RV, determined by projecting the RV's center-of-mass onto the base plane and resolving the vector from the LV origin to that point. Together with the implicitly defined, orthogonal x-axis, this yielded a standardized orientation for all hearts. Crucially, this alignment ensures that each sampled point has one-to-one anatomical correspondence across subjects. In other words, points indexed the same (e.g., the 5th point on the 10th plane) lie in equivalent anatomical regions in every heart. This standardized coordinate framework eliminates differences due to arbitrary pose or position, allowing direct comparison of shape features across the cohort. Furthermore, each patient's point cloud was height-normalized, which reduced shape size differences attributable to patient height [9].

3.2.3.1 Motion analysis

To complement the static ED shape analysis, we evaluated LV systolic motion by quantifying the displacement of the endocardial and epicardial surfaces between ES and ED. The sets of motion vectors were characterized by subtracting the ED point cloud coordinates from the corresponding ES point cloud coordinates. Three patients were missing ES point clouds, resulting in a total of 88 patients. Of these, 13 patients were arrhythmic (8 females and 5 males).

3.2.4 Statistical shape analysis and association with arrhythmia

PCA was used to identify the dominant modes of variation in LV geometry at ED as well as in systolic wall motion derived from ES–ED displacement fields. These modes provide an interpretable decomposition of global shape and motion patterns

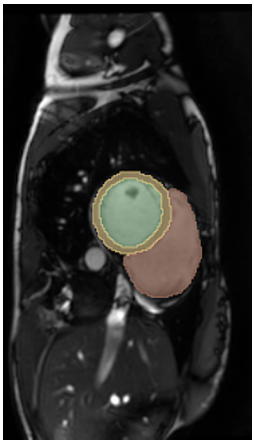

Fig. 3.2: A successful segmentation using the MONAI model [12]. The LV myocardium is segmented in yellow, while the LV and RV blood pools are segmented in green and red, respectively.

into orthogonal components, each capturing a distinct axis of variability within the cohort.

To assess the relationship between these modes and clinical outcomes, we applied nonparametric Mann–Whitney U-tests for binary variables, comparing patients with and without a history of arrhythmia. For chosen continuous clinical variables available, linear regression was used to evaluate correlations with individual PCA modes. All analyses were also stratified by sex to explore potential sex-specific associations. A two-sided significance threshold of $p < 0.05$ was applied throughout.

3.3 Results

3.3.1 Modes of variation

Five and six principal modes described the majority of shape variation for ED (Figure 3.3a) and motion data (Figure 3.3b), respectively. For simplicity, we will refer to the modes as M1, M2, ... , MN, where N represents the mode number. We focus here on the modes that showed significant associations with clinical measurements or arrhythmic events, rather than describing all modes, to highlight the patterns most relevant to arrhythmic risk and LV remodeling. For visualization, we depict the effect of each mode at ±2 standard deviations (SD) from the mean.

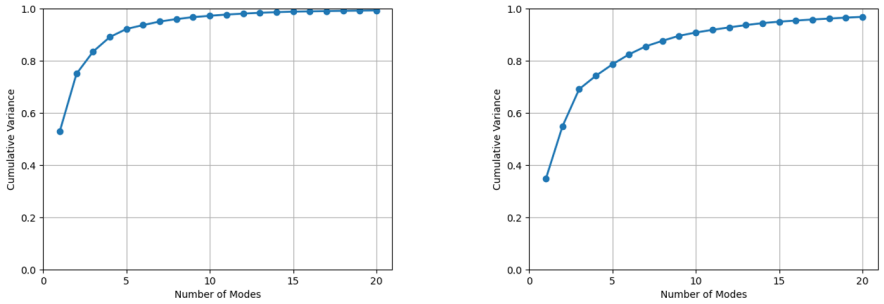

(a) ED data.

(b) Motion data.

Fig. 3.3: Cumulative variance explained by PCA modes for ED (a) and motion (b) data. Five principal modes explain over 90% of the data for ED and six principal modes explain just over 80% for the motion analysis data, ES-ED.

ED Shape Modes

Figure 3.4 provides visual examples of different modes present in the ED data. Here, M1 (top row) primarily reflects global size variation. At -2SD (left), the LV appears smaller, while +2SD (right) represents a globally dilated chamber with outward bowing of the walls and a blunter apex. M2 (middle row) describes differences in sphericity with a slimmer LV at -2SD and a fuller and rounder LV at +2SD.

M5 (bottom row) reflects mid-wall asymmetry between the lateral wall and septum. In the –2SD configuration, there is septal bulging with a blunter apex compared to the mean geometry, while the +2SD configuration shows that the lateral wall bulges outward closer to the base and the septum flattens.

Wall Motion Modes

Figure 3.5 illustrates examples of modes present in the motion data. M1 (top row) predominantly captures base-apex (longitudinal) displacement. At +2 SD, the LV exhibits pronounced inward displacement throughout the chamber, whereas at –2 SD this inward motion is attenuated and, in some regions, nearly absent or outward, consistent with substantially reduced global contraction relative to the mean. M3 (second row) represents radial wall motion in the short-axis plane. At -2SD, the systolic inward displacement of the walls is mild (weaker radial contraction), while at +2SD the walls move markedly inward (stronger radial contraction). M4 (third row) highlights a differential base-to-apex pattern: at +2SD, the basal and apical regions exhibit displacement in opposite directions around the ventricular circumference, whereas at -2SD displacement occurs in the opposite circumferential direction. This opposite-motion pattern should not be interpreted as true myocardial torsion, as the motion field is derived from independent ES and ED shapes rather than

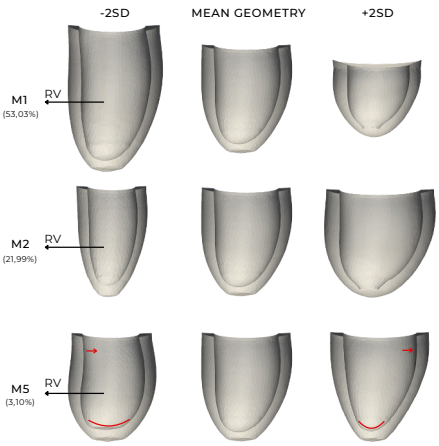

Fig. 3.4: Examples of modes (M1, M2, M6) captured by the PCA at ED, with the percentage of variance explained indicated for each mode. The central column shows the mean LV geometry, while columns to the left and right illustrate ±2 standard deviations (SD). The left column also illustrates the orientation of all LV in the same row.

tracked rotation. Finally, M6 (bottom row) captures localized regional displacement differences. At +2SD, a focal outward bulge appears in the anterior wall region, whereas at -2SD the bulging is instead observed in the opposite (inferior) wall region.

3.3.2 Correlation with clinical variables

Figure 3.6 shows the correlation of the modes with any type of arrhythmia for the ED analysis. M1 and M2 significantly correlate with any type of arrhythmia ($p = 0.02$ and $p = 0.01$, respectively).

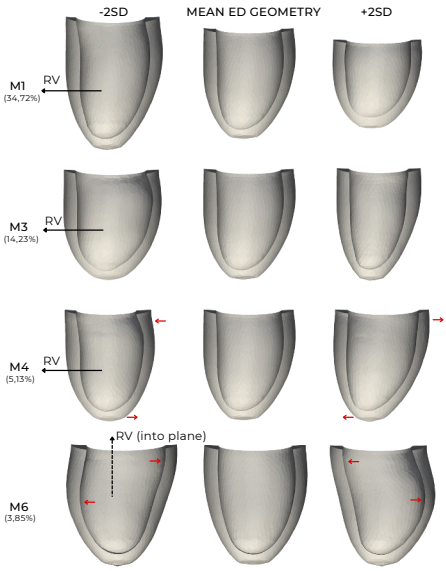

Fig. 3.5: Examples of modes (M1, M3, M4, M6) captured by the PCA for motion data (ES-ED), with the percentage of variance explained indicated for each mode. The central column shows the mean LV geometry at ED, while columns to the left and right illustrate ±2 standard deviations (SD) of the motion (ES-ED) visualized on the mean ED geometry. The left column also illustrates the orientation of all LV in the same row.

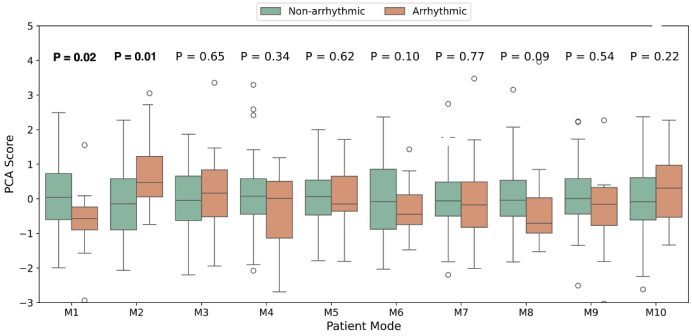

Fig. 3.6: Correlation of the different modes with any type of arrhythmia for ED analysis. Results are presented as median values with interquartile ranges, significant ($p < 0.05$) modes in bold.

When considering sex differences, we see that for females M1 and M5 significantly correlate with any type of arrhythmia ($p = 0.02$ and $p = 0.02$, respectively) in Figure 3.7a, while for males the significant modes are M2 and M5 ($p = 0.02$ and $p = 0.04$, respectively) in Figure 3.7b. Interestingly, M5 exhibited opposite patterns between sexes: in females, higher M5 values were observed in arrhythmic patients compared to non-arrhythmic patients, while in males, arrhythmic patients had lower M5 values than non-arrhythmic patients. This explains why a pooled analysis does not show M5 as significant.

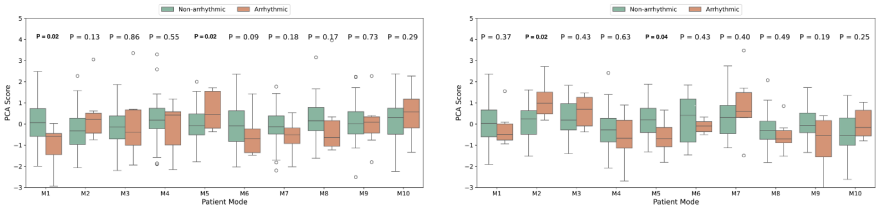

(a) Female (b) Male

Fig. 3.7: Correlation of the different modes with any type of arrhythmia for ED analysis, stratified by sex.

Figure 3.8 shows the correlation of the modes with any type of arrhythmia for the motion analysis. M3 and M6 significantly correlate with any type of arrhythmia ($p = 0.01$ and $p = 0.04$, respectively).

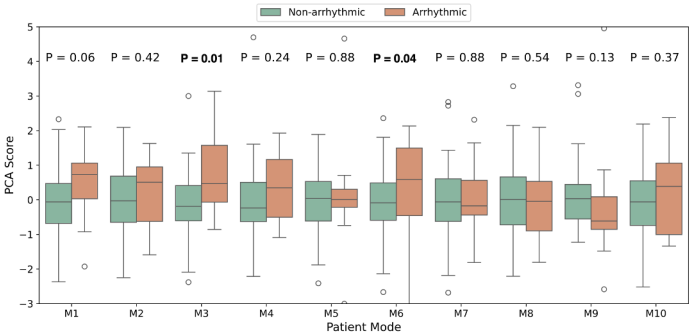

Fig. 3.8: Correlation of the different modes with any type of arrhythmia for motion analysis.

When considering sex differences in the motion analysis, we see that for females M1 and M3 significantly correlate with any type of arrhythmia ($p = 0.01$ and

$p = 0.05$, respectively) in Figure 3.9a, while for males the significant modes are M4 and M6 ($p = 0.04$ and $p = 0.02$, respectively) in Figure 3.9b.

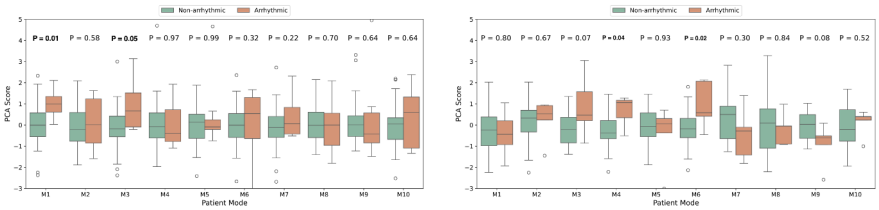

(a) Female

(b) Male

Fig. 3.9: Correlation of the different modes with any type of arrhythmia for motion analysis, stratified by sex.

In addition, we examined correlations between PCA modes and the presence of overall fibrosis, fibrosis localized to the papillary muscles, and MAD presence, as well as associations with continuous clinical measurements, including volumes and percentage of fibrosis, ejection fraction, MAD length, and wall thickness. None of these analyses yielded statistically significant results.

3.4 Discussion

We identified PCA-derived modes of ED geometry and systolic wall motion (ES - ED) that captured the main axes of left ventricular shape variation in patients with MAD. Five modes described the majority (ca. 90%) of ED shape variation, while six modes described the majority (ca. 80%) of motion variation. In the ED analysis, M1 and M2 were significantly associated with arrhythmic status overall. When stratified by sex, M1 and M5 were significant in females, and M2 and M5 were significant in males, with M5 showing opposite trends between sexes. For motion data, M3 and M6 were associated with arrhythmia overall, while sex-specific analyses revealed significant associations of M1 and M3 in females, and M4 and M6 in males. No significant correlations were observed in this study between any PCA mode and fibrosis, MAD presence, or continuous clinical measures including LV volumes, percentage of fibrosis, ejection fraction, MAD length, or wall thickness.

In the ED analysis, M1 and M2 were significantly associated with a history of arrhythmia. M1 (Figure 3.4) reflects elongation or dilation of the basal region, which may correspond to the annular disjunction gap. This aligns with prior observations that MVP patients at risk often exhibit structural abnormalities at the base of the heart, such as MAD or a “hooded” LV base geometry [15]. MAD has been linked to ventricular ectopy and fibrosis independent of leaflet prolapse [15], making it notable that our shape analysis captured variance in the basal annular region associated with

arrhythmic status. The second ED shape mode, M2 (Figure 3.4), represents increased LV spherical remodeling. A more spherical (globular) LV shape has been associated with adverse remodeling and dysfunction in other cardiac diseases [10]. Although MVP classically involves a normal or hyperdynamic ejection fraction, this subtle spherical remodeling in arrhythmic patients may indicate early myocardial changes that predispose to electrical instability.

The LV motion analysis provided additional insights into how altered mechanics might contribute to arrhythmogenesis in MVP/MAD. M3 (Figure 3.5) described reduced longitudinal shortening, essentially, a blunted base-to-apex contraction. In normal hearts, longitudinal (basal-apical) contraction is a major contributor to efficient systolic function, and its reduction can signify subtle dysfunction [10]. In MVP, diminished longitudinal shortening or delayed contraction in certain regions could create heterogeneity in timing (mechanical dispersion) and areas of stretch that facilitate arrhythmia. Indeed, prior work using speckle-tracking echocardiography has shown that increased LV mechanical dispersion is a predictor of ventricular arrhythmias in MVP [16]. M3 may be capturing a similar phenomenon of dyssynchronous or impaired regional contraction that predisposes to ectopy. M6 (Figure 3.5) corresponded to abnormal deformation at the posterior–basal LV (near the mitral annulus). Specifically, arrhythmic MVP hearts demonstrated an exaggerated systolic displacement of the posterior annular region relative to the LV apex. This finding is consistent with the clinical observation of "systolic curling," an abnormal systolic hinging motion of the mitral annulus that has been associated with myocardial fibrosis in MVP [15]. Basso et al. have hypothesized that in MVP with MAD, excessive leaflet motion and annular curling lead to a paradoxical increase in annular diameter during systole, stretching the basal inferolateral myocardium and papillary muscles and ultimately causing regional hypertrophy, fibrosis, and ventricular ectopy [8].

The sex-specific patterns we observed (e.g. a particular shape mode correlating with arrhythmia only in females or males) indicate possible differences in LV remodeling associated with AMVS between sexes. Malignant MVP has historically been reported more frequently in middle-aged women [15], though this is not a consistent finding across all studies. Our data hint that the LV remodeling associated with arrhythmia might manifest differently between sexes, possibly due to hormonal, genetic, or anatomical factors, but further investigation with larger cohorts is needed to confirm and explain these differences.

Despite these promising findings, several limitations of our approach must be acknowledged. First, while our segmentation and alignment methods were generally reliable, any segmentation errors or misalignment could introduce noise into the shape modes. We mitigated this through careful quality control, but the method's accuracy still depends on the initial image processing. Secondly, the motion was based on subtraction of ED coordinates from the ES coordinates. This subtraction-based method inherently does not capture rotational or torsional deformations of the LV. Ventricular twist (the opposite rotation of the apex and base during systole) is a key component of normal LV mechanics, contributing to efficient ejection and subsequent diastolic recoil. Future studies should address this by incorporating rotation-aware motion descriptors. This could be achieved by augmenting the point-cloud analysis

with angular measurements or by employing 3D strain tensor analysis to directly quantify torsion and other complex deformations. A related technical limitation is that PCA, being a linear dimensionality reduction, may not fully capture nonlinear shape changes. We used a limited number of modes (focused on the most variance), which additionally might miss subtler patterns. Our statistical analysis was restricted to linear correlations, which may have overlooked potential non-linear relationships between modes and clinical data. Another limitation is the cross-sectional design and sample size of our study. The associations we identified between shape/motion modes and arrhythmias are correlational. We cannot ascertain causality, whether the geometric and functional abnormalities contribute to arrhythmia or are simply consequences of a primary arrhythmogenic process. Longitudinal studies will be needed to determine if certain shape or motion profiles can predict future arrhythmic events in MVP. Furthermore, our cohort was relatively moderate in size and drawn from a single tertiary center specializing in MVP; this may limit generalizability. The significant mode differences we observed should be validated in larger, independent populations.

To summarize, we applied statistical shape modeling to both ED geometry and systolic motion, identifying principal modes of LV shape and motion in MAD patients and examining their associations with arrhythmic status, including sex-specific patterns. Traditional markers such as severe mitral regurgitation, bileaflet prolapse, or fibrosis on cardiac MRI have been used to identify high-risk MVP, but many patients with malignant ventricular arrhythmias have only mild regurgitation or minimal overt abnormalities [15, 10] The ability to detect subtle shape and motion deviations in the LV using SSM could augment current imaging assessment for MVP/MAD patients and potentially improve risk stratification. For example, a high score in a “basal annular motion” mode or “longitudinal function” mode might flag a patient who, despite preserved ejection fraction, has underlying mechanical dysfunction predisposing to ventricular ectopy. Identifying such high-risk mechanical phenotypes could prompt closer monitoring (e.g. intensive Holter surveillance) or consideration of prophylactic interventions.

3.5 Conclusion

We extended a previously developed statistical shape modeling pipeline for ES to include ED and systolic motion (ES - ED). For ED, two modes M1 and M2 show a significant association with arrhythmia, while for systolic motion this holds for M3 and M6. Furthermore, we showed that, in both ED and motion, considering sex difference reveals additional modes that are significantly associated with arrhythmia. This demonstrates that incorporating motion analysis as well as sex differences adds valuable information. In future work, statistical shape analysis results could be used to evaluate associations with other clinical variables such as myocardial and papillary muscle fibrosis. Moreover, combining ED and motion PCA scores might prove to be even be more predictive. Overall, this study shows that LV shape modes (ED and

motion) hold promise as potential biomarkers for arrhythmic risk in AMVS, offering a complementary approach to current clinical methods.

References

1. Gregory A Roth, George A Mensah, Catherine O Johnson, Giovanni Addolorato, Enrico Ammirati, Larry M Baddour, Noël C Barengo, Andrea Z Beaton, Emelia J Benjamin, Catherine P Benziger, et al. Global burden of cardiovascular diseases and risk factors, 1990–2019: update from the gbd 2019 study. Journal of the American college of cardiology, 76(25):2982–3021, 2020.
2. Avi Sabbag, Benjamin Essayagh, Juan David Ramirez Barrera, Cristina Basso, Ana Berni, Bernard Cosyns, Jean-Claude Deharo, Thomas Deneke, Luigi Di Biase, Maurice Enriquez-Sarano, et al. Ehra expert consensus statement on arrhythmic mitral valve prolapse and mitral annular disjunction complex in collaboration with the esc council on valvular heart disease and the european association of cardiovascular imaging endorsed cby the heart rhythm society, by the asia pacific heart rhythm society, and by the latin american heart rhythm society. Europace, 24(12):1981–2003, 2022.
3. Fatemeh Adabifirouzjaei, Albert Hsiao, and Anthony N DeMaria. Mitral valve prolapse—the role of cardiac imaging modalities. Structural Heart, 6(2):100024, 2022.
4. Lars A Dejgaard, Eystein T Skjølsvik, Øyvind H Lie, Margareth Ribe, Mathis K Stokke, Finn Hegbom, Esther S Scheirlynck, Erik Gjertsen, Kristoffer Andresen, Thomas M Helle-Valle, et al. The mitral annulus disjunction arrhythmic syndrome. Journal of the American College of Cardiology, 72(14):1600–1609, 2018.
5. Caitlin S Drescher, Michelle D Kelsey, George S Yankey, Albert Y Sun, Andrew Wang, Anita Sadeghpour, Donald D Glower Jr, Sreekanth Vemulapalli, and Anita M Kelsey. Imaging considerations and clinical implications of mitral annular disjunction. Circulation: Cardiovascular Imaging, 15(9):e014243, 2022.
6. Benjamin Essayagh, Avi Sabbag, Clémence Antoine, Giovanni Benfari, Li-Tan Yang, Joseph Maalouf, Samuel Asirvatham, Hector Michelena, and Maurice Enriquez-Sarano. Presentation and outcome of arrhythmic mitral valve prolapse. Journal of the American college of cardiology, 76(6):637–649, 2020.
7. Cristina Basso, Martina Perazzolo Marra, Stefania Rizzo, Manuel De Lazzari, Benedetta Giorgi, Alberto Cipriani, Anna Chiara Frigo, Ilaria Rigato, Federico Migliore, Kalliopi Pilichou, et al. Arrhythmic mitral valve prolapse and sudden cardiac death. Circulation, 132(7):556–566, 2015.
8. Martina Perazzolo Marra, Cristina Basso, Manuel De Lazzari, Stefania Rizzo, Alberto Cipriani, Benedetta Giorgi, Carmelo Lacognata, Ilaria Rigato, Federico Migliore, Kalliopi Pilichou, et al. Morphofunctional abnormalities of mitral annulus and arrhythmic mitral valve prolapse. Circulation: Cardiovascular Imaging, 9(8):e005030, 2016.
9. Giulia Monopoli, Mohammad Javad Sadeghinia, Eivind Westrum Aabel, Margareth Ribe, Anna Isotta Castrini, Nina Hasselberg, Cecilie Bugge, Christian Five, Kristina Haugaa, Gabriel Balaban, et al. Arrhythmic mitral valve syndrome: Insights from left ventricular end-systolic shape analysis. In International Conference on Functional Imaging and Modeling of the Heart, pages 26–36. Springer, 2025.
10. Genevieve Farrar, Avan Suinesiaputra, Kathleen Gilbert, James C Perry, Sanjeet Hegde, Alison Marsden, Alistair A Young, Jeffrey H Omens, and Andrew D McCulloch. Atlas-based ventricular shape analysis for understanding congenital heart disease. Progress in pediatric cardiology, 43:61–69, 2016.
11. Eivind W Aabel, Monica Chivulescu, Lars A Dejgaard, Margareth Ribe, Erik Gjertsen, Einar Hopp, Tove E Hunt, Øyvind H Lie, and Kristina H Haugaa. Tricuspid annulus disjunction: novel findings by cardiac magnetic resonance in patients with mitral annulus disjunction. Cardiovascular Imaging, 14(8):1535–1543, 2021.

12. Eric Kerfoot, James Clough, Ilkay Oksuz, Jack Lee, Andrew P King, and Julia A Schnabel. Left-ventricle quantification using residual u-net. In International workshop on statistical atlases and computational models of the heart, pages 371–380. Springer, 2018.
13. Olaf Ronneberger, Philipp Fischer, and Thomas Brox. U-net: Convolutional networks for biomedical image segmentation. In International Conference on Medical image computing and computer-assisted intervention, pages 234–241. Springer, 2015.
14. Andriy Fedorov, Reinhard Beichel, Jayashree Kalpathy-Cramer, Julien Finet, Jean-Christophe Fillion-Robin, Sonia Pujol, Christian Bauer, Dominique Jennings, Fiona Fennessy, Milan Sonka, et al. 3d slicer as an image computing platform for the quantitative imaging network. Magnetic resonance imaging, 30(9):1323–1341, 2012.
15. Theofanis George Korovesis, Paraskevi Koutrolou-Sotiropoulou, and Demosthenes George Katritsis. Arrhythmogenic mitral valve prolapse. Arrhythmia & Electrophysiology Review, 11:e16, 2022.
16. James N Cameron, Kadhim I Kadhim, Suraya HB Kamsani, Hui-Chen Han, Omar Farouque, Prashanthan Sanders, and Han S Lim. Arrhythmogenic mitral valve prolapse: can we risk stratify and prevent sudden cardiac death? Arrhythmia & Electrophysiology Review, 13:e11, 2024.

Chapter 4
Differentiating the Roles of Metabolic Similarity and Ionic Coupling in Determining the Beta Hub Cell Phenotype

Ingvild S. Devold, Hanne Rokstad, Jazmin Velazquez, Shane Browne, Andrew G. Edwards, and Vira Kravets

Abstract Pancreatic beta cells regulate circulating glucose levels by releasing insulin. Beta cells transduce elevated blood glucose into electrical activity through an intrinsic cascade of metabolic and electrophysiologic responses. These responses are synchronized across the electrically connected network of beta cells, such that insulin release is also relatively synchronous. Despite their coordinated behavior, individual beta cells exhibit significant functional heterogeneity. This heterogeneity is thought to provide cells with specific functional phenotypes the ability to control the activity of the broader network. Hub cells, identified by their synchronized [Ca^{2+}] activity, are one such functional subpopulation, and are believed to orchestrate the second, oscillatory phase of insulin release. However, it remains unclear whether the cell-autonomous characteristics of hub cells, such as their metabolic activity and electrophysiologic properties, are more important than their network characteristics (i.e. gap junctional coupling) for their ability to influence broader network activity. In this study, we investigate the roles of intrinsic metabolic and electrophysiologic properties and ionic coupling in determining the beta hub cell phenotype. Using a computational islet model of 1,000 beta cells, our analysis revealed that the most

Ingvild S. Devold
Department of Numerical Analysis and Scientific Computing, Simula Research Laboratory, Norway

Hanne Rokstad
Department of Physics, Norwegian University of Science and Technology, Norway

Jazmin Velazquez
Department of Bioengineering, University of California Berkeley, USA

Shane Browne
Department of Mechanical and Aerospace Engineering, University of California San Diego, USA

Andrew G. Edwards
Department of Computational Physiology, Simula Research Laboratory, Norway

Vira Kravets (corresponding author)
Department of Bioengineering & Department of Pediatrics, University of California San Diego, USA e-mail: vkravets@ucsd.edu

K. J. McCabe, *Computational Physiology*, Simula SpringerBriefs on Computing 20, https://doi.org/10.1007/978-3-032-28826-4_4

significant parameters differentiating hub cells from followers were their largely increased glycolysis rate, slightly lower kATP conductance, and much higher gap-junctional coupling currents. After investigating the intrinsic coupling conductance of neighboring cells and the number of structural (direct electrical) links as independent contributors to the hub cell's local electrical coupling, we find that the number of cells to which a beta cell is directly coupled may be a key determinant of its propensity to serve as a hub cell in the model. As predicted for this subpopulation, we also demonstrate that decoupling hub cells impairs the functional connectivity of the entire network. Our findings indicate the importance of both autonomous cellular dynamics and non-autonomous structural coupling for the hub cell phenotype. These insights help build a fundamental understanding of hub cells, which in turn may contribute to identifying potential approaches to preserve or improve beta cell function and thereby manage the progression of diabetes.

4.1 Introduction

Beta cells in the pancreatic islets regulate blood glucose levels through insulin secretion. These cells respond to changes in glucose concentrations by generating electrical signals that trigger insulin release, and their dysfunction is linked to diabetes. Although the responses of beta cells often appear highly synchronized, these cells are functionally heterogeneous. Different subpopulations have been proposed to play distinct roles in modulating islet function. "First responder" beta cells have been hypothesized to drive the first phase of insulin release by reacting most quickly to glucose elevation and thereby initiating the electrical activity that in turn drives increased $[Ca^{2+}]$ and insulin secretion[1, 2]. Experimental and computational studies have also identified "hub" cells, which are distinguished by their highly synchronized $[Ca^{2+}]$ activity during the second oscillatory phase of insulin release and thought to be largely responsible for coordinating second phase activity of the islet[3, 4, 5].

In response to glucose, increased glycolytic flux and ATP production cause ATP-sensitive potassium channels (K_{ATP}) to close, leading to membrane depolarization. This triggers the opening of voltage-gated calcium channels, resulting in elevated intracellular $[Ca^{2+}]$, which in turn stimulates insulin release. Importantly, each beta cell is not an isolated functional entity, but one functional component of a large network of beta cells that is electrically coupled through connexin 36 (Cx36) gap junctions [6]. This gap junctional coupling allows the cells to synchronize their electrical activity and generate a pulsatile insulin release, coordinated across the islet. In combination, this signaling cascade and structural connectivity causes beta cell and islet function to be influenced by both the intrinsic, autonomous properties of each cell and non-autonomous properties arising from the cell's role in a network connected by gap junctions.

These complex interactions are challenging to study experimentally, but they lend themselves to computational modeling. To better understand the relative importance of autonomous and non-autonomous factors, we apply a computational model of

a mouse pancreatic beta cell network [7, 8, 2, 5]. This model, an extension of the single beta cell Cha-Noma model [9], simulates a network of 1000 beta cells, electrically coupled through gap junctions [7]. The model allows us to simulate calcium dynamics, and thereby identify hub cells via correlation analysis, analogously to experimental approaches [10, 3]. A key advantage of this computational approach is the opportunity to systematically investigate the role of intrinsic properties of beta cells, such as metabolic parameters, or their network properties, such as gap junction coupling, for determining overall islet function.

In this study, we aim to understand how both intrinsic cell dynamics and communication through gap junctions determine hub cell properties within a beta cell network. By simulating islets with variable parameters and decoupling different subpopulations on the basis of those parameters or of their function within the network, we can explore how intrinsic cell dynamics and gap junctional coupling influence the overall function of pancreatic islets. Proper understanding of these interactions is essential in preserving and improving beta cell function to potentially develop targeted therapies preventing the progression of diabetes.

4.2 Methods

4.2.1 Coupled Cha-Noma beta cell model

We used a previously introduced computational model of a heterogeneous network of beta cells [7], implemented in C++. The model builds upon the Cha-Noma model [9, 11], which describes the electrophysiological properties of a single mouse beta cell, including ion channels, transporters, and $[Ca^{2+}]$ dynamics (see Figure 4.1). This is extended to a network of $N = 1000$ cells, with between 1 and 12 gap junction connections per cell [5]. The system is described by a set of ordinary differential equations (ODEs), where the membrane potential V_i of each cell i is governed by

$$\begin{aligned} C_m \frac{dV_i}{dt} = {} & I_{\mathrm{CaV}} + I_{\mathrm{TRPM}} + I_{\mathrm{SOC}} + I_{\mathrm{bNSC}} + I_{\mathrm{KDr}} + I_{\mathrm{KCa(SK)}} \\ & + I_{\mathrm{KATP}} + I_{\mathrm{NaCa}} + I_{\mathrm{PMCA}} + I_{\mathrm{NaCa}} + I_{\mathrm{NaK}} + I_{\mathrm{coup}} \end{aligned} \tag{4.1}$$

and solved for in each time step. Here, the coupling current,

$$I_{\mathrm{coup}} = \sum_j \frac{1}{2} \left(g^i_{\mathrm{coup}} + g^j_{\mathrm{coup}} \right) \left(V_i - V_j \right), \tag{4.2}$$

models the current through the cell's Cx36 gap junctions and depends on the voltage difference between the connected cell pairs (i, j) and both their intrinsic coupling conductances, g_{coup}.

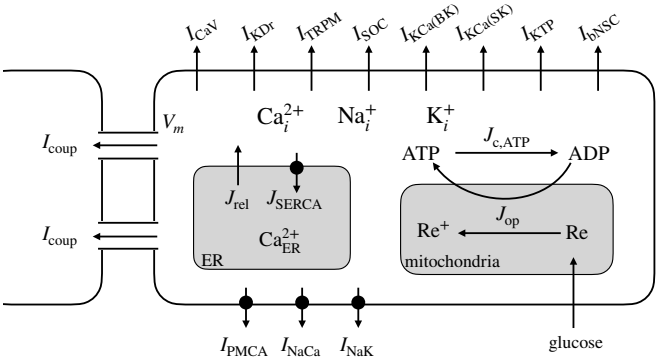

Fig. 4.1: Schematic diagram of the coupled Cha-Noma model. Figure recreated with modification from [9].

4.2.2 Cellular heterogeneity from randomized parameter values

Heterogeneity was introduced to the model by assigning randomized parameter values to cells based on previously established distributions from experiments [7]. Table 4.1 shows the distributions used for three of the parameters. The parameter assignments were seeded, and for our experiments, we ran repeated simulations for different seeds, in an attempt to mimic the variability found in experimental islets and to enhance the statistical robustness of the analysis.

Parameter	Symbol	Distribution	Mean	SD	Unit
Glycolysis rate	k_{glyc}	Normal	0.126	0.0315	ms^{-1}
Coupling conductance	g_{coup}	Gamma(4,4)	0.12	0.06	nS
K_{ATP} channel conductance	g_{KATP}	Normal	2.31	0.57	pA/mV

Table 4.1: A selection of probability distributions used when assigning randomized parameter values to cells in the computational beta cell network model [5].

4.2.3 Driving glucose curve

The primary driver of the simulation was a prescribed glucose curve $[G](t)$. We used a simple step function for this purpose, starting with an initial glucose concentration of $[G] = 2.0$ mM for the first 20 seconds. After this period, the glucose concentration was increased to a chosen maximum level (e.g. $[G]_{max} = 12.0$ mM), which was maintained for the remainder of the simulation. We tested $[G]_{max} \in \{2, 4, 6, 8, 10, 12\}$

mM, and ran analysis on the $[G]_{max} = 12$ mM case since this consistently produced $[Ca^{2+}]$ oscillations across seeds.

4.2.4 Defining the functional network from Ca2+ activity

Among the simulation outputs were the $[Ca^{2+}]$ time series data for each of the $N = 1000$ beta cells. These time series were used to construct the islet functional network by identifying highly synchronized cells, as described in [5]. First, we extracted a time window containing the second, oscillatory phase. For simulations with duration 900 s, we used the period from 100 s to the end of the simulation. With the $[Ca^{2+}]$ data from this time window, we computed the correlation matrix using MATLAB's `corr()` function, which provides the Pearson correlation coefficients,

$$R \in \mathbb{R}^{N\times N}, \quad R_{ij} = \frac{\sum[x_i(t) - \bar{x}_i][x_j(t) - \bar{x}_j]}{\sqrt{\sum[x_i(t) - \bar{x}_i]^2 \sum[x_j(t) - \bar{x}_j]^2}}.$$

Next, we applied a threshold R_{th} to identify synchronized cell pairs. Cell pairs with correlation coefficients above this threshold were considered functionally linked. The resulting adjacency matrix A, with entries

$$A_{ij} = \begin{cases} 1 & \text{if } R_{ij} \geq R_{th}, \\ 0 & \text{otherwise,} \end{cases} \tag{4.3}$$

defined the beta cell functional network. We chose the threshold $R_{th} = 0.99975$ to yield a power law distribution of network degree, as suggested by experimental studies [12, 3].

4.2.5 Analysis

4.2.5.1 Identifying hub cells from network degree

The degree of a node in a network refers to its number of edges. In the context of the beta cell functional network, this corresponds to the number of cells a given cell is highly synchronized with, and therefore likely to be functionally coupled with. In this simulation framework, the only direct means of coupling is gap junctional. We identified hub cells as those whose degree exceeded 65% of the maximal degree observed for any cell in the network ($deg_{th} = 0.65$). This criterion resulted in a proportion of hub cells consistent with the previously suggested range of 1-10% [3].

4.2.5.2 Comparative analysis of hubs and followers

Statistical inference was performed via two-sample t-test, using MATLAB's ttest2() function for comparison of hubs vs. followers. All t-tests were performed at the seed level, such that the mean parameter values for hubs and followers from each seed constituted the independent observations subjected to t-tests. In addition to comparing the assigned randomized parameters, we calculated the *total* gap junction coupling conductance as suggested in [5],

$$g_{\text{coup}}^{i,\text{tot}} = \sum_{j=1}^{m} \frac{1}{2}(g_{\text{coup}}^{i} + g_{\text{coup}}^{j}), \tag{4.4}$$

summing the average coupling conductances of the cell and its physically linked neighbors ($j = 1, \ldots, m$). This parameter incorporates both the number of gap junctions of a given cell, its intrinsic coupling conductance, and the intrinsic coupling conductances of its connected cells.

4.2.6 Decoupling beta cell subpopulations

Following the original islet simulations and subsequent analysis, we re-ran the simulations after decoupling specific subsets of beta cells. For example, all cells in the top 10% of the coupling distribution. In this process we simulated removal of those cells' gap junctions by excluding their coupling current contributions (Equation 4.2) from the ODE system. In these decoupled simulations, the decoupled subpopulation was also excluded from the subsequent analysis. To ensure a fair comparison between simulated decoupling experiments, we consistently decoupled a fixed number of cells. This approach prevented variations in the size of the decoupled subgroups. Finally, the decoupling of a random group of cells served as a control, allowing us to isolate the effects of decoupling specific subpopulations from the more general effect of the decoupling itself.

4.3 Results

To analyze the relative importance of functional similarity and structural network connectivity to the beta hub cell phenotype, we analyzed a simulated beta cell network using an extension of the Cha-Noma model [9]. The model incorporates both the main ion channels affecting the beta cell membrane potential and the electrical coupling between cells through Cx36 gap junction channels. Cellular heterogeneity was implemented through randomized parameters (Figure 4.2A), assigned according to probability distributions based on experimental data [7]. The islet was stimulated by a $[\text{G}]_{\text{max}} = 12.0\,\text{mM}$ maximum glucose concentration from 20 s to 900 s. We

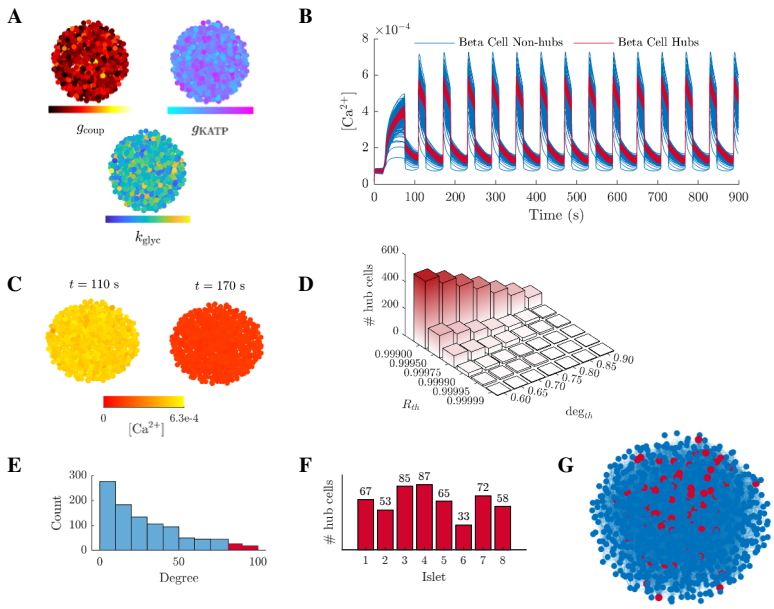

Fig. 4.2: **From structural to functional beta cell network.** (**A**) The 1000-cell beta cell network false-colored by parameter values (gap junction coupling conductance g_{coup}, K_{ATP} channel conductance g_{KATP}, and glycolysis rate k_{glyc}). (**B**) Calcium response from the islet shown in (A), simulated at $[G]_{\text{max}} = 12$ mM for 900 s, with hub cells highlighted in red. (**C**) False-color map displaying the beta cell network calcium concentration at two time points, near a peak ($t = 110$ s) and a nadir ($t = 170$ s). (**D**) Number of identified hub cells for different correlation (R_{th}) and network degree (deg_{th}) thresholds. (**E**) Degree distribution of the functional network. Hub cells with normalized degree exceeding 0.65 highlighted in red. (**F**) Number of identified hubs for eight different simulated islets, using the $R_{th} = 0.99975$ and $\text{deg}_{th} = 0.65$ criteria. (**G**) Beta cell functional network with identified hubs highlighted in red.

repeated the simulation for 8 different islets, each with different randomized parameter values. This produced fast (< 2 min) and highly synchronized Ca^{2+} oscillations for all simulated islets. Figure 4.2B shows a representative calcium response of one simulated islet, and Figure 4.2C highlights the tight coupling of the network at two time points – at a peak and a nadir of the calcium response.

4.3.1 Two thresholds determine the number of identified hub cells

We examined the effect of two thresholds on the number of identified hub cells (Figure 4.2D). Our analysis confirmed that both the correlation threshold R_{th} and the degree threshold $\deg_{th}$ impact the number of hub cells identified, with larger thresholds resulting in fewer hubs. Moreover, the correlation threshold R_{th} directly affects the degree distribution of the functional network. Figure 4.2E displays the power-law-like distribution obtained using a value $R_{th} = 0.99975$. Using the $R_{th} = 0.99975$ and $\deg_{th} = 0.65$ criteria, we obtained hub cell proportions between 3% and 9% for the different simulated islets (Figure 4.2F). This is in agreement with the 1%-10% interval previously advocated for based on experiments [3]. Finally, Figure 4.2G shows the spatial distribution of the identified hub cells in the functional network for one simulated islet. We found no discernible pattern in the spatial organization of the hub cells. Instead, they appeared to be randomly scattered across the network.

4.3.2 Simulations of Ca2+ oscillations reveal that both metabolic activity and structural coupling are key in differentiating beta cell hubs

Next, we analyzed 8 simulated islets with different randomized parameter sets to investigate systematic differences between hub and follower beta cell subpopulations. The glucokinase activity, quantified by the glycolysis rate k_{glyc}, serves as an indicator of the cell's metabolic activity. We found that k_{glyc} was significantly higher in hub cells than follower cells (mean ± SD $0.14 \pm 0.0022\,\text{ms}^{-1}$ vs. $0.12 \pm 0.0009\,\text{ms}^{-1}$, $p < 0.001$) (Figure 4.3A). The primary point of coupling between metabolic and electrical activity in beta cells is the ATP-sensitive potassium channel. The conductance of these channels (g_{KATP}), which corresponds to the number of K_{ATP} channels, is expected to impact cell dynamics. We observed that g_{KATP} was slightly lower in hub cells compared to follower cells (mean ± SD $2.27 \pm 0.05\,\text{pA/mV}$ vs. $2.31 \pm 0.02\,\text{pA/mV}$, $p = 0.03$) (Figure 4.3B). These results suggest that, within this model, metabolic activity plays a more important role than the number of K_{ATP} channels in determining the hub cell phenotype. This finding aligns with previous research [5].

Intuitively, it is reasonable to expect that structural coupling affects network synchrony and therefore high structural coupling may be a characteristic feature of beta hub cells. Still, we observed that intrinsic coupling conductance (the g_{coup} attributable only to each cell, rather than the cell and its direct connections) did not differ significantly between hub and follower cells (mean ± SD 0.121 ± 0.006 nS vs. 0.118 ± 0.002 nS, $p = 0.33$) (Figure 4.3C). However, comparing the total gap junction coupling conductance (Equation 4.4), we observed that this was significantly higher for hub cells than followers (mean ± SD 0.73 ± 0.03 nS vs. 0.64 ± 0.01 nS, $p < 0.001$) (Figure 4.3D). This suggests that both the intrinsic coupling conductance of the cell, and the coupling conductances of cells in its direct network (those coupled to it)

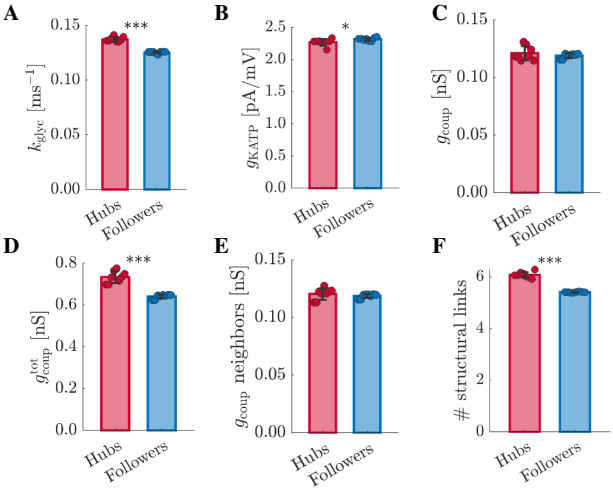

Fig. 4.3: **Analysis of parameter differences between the hub and follower beta cell subpopulations.** Significance was determined by paired t-tests. $*p < 0.05$, $**p < 0.01$, $***p < 0.001$. Data points represent average values of each simulated islet, and error bars represent SD. (**A**) Mean parameter value of glycolysis rate (k_{glyc}) averaged over the hub and follower (non-hub) cell subpopulations ($n = 8$ seeds). (**B**) As in (A) for K_{ATP} conductance (g_{KATP}). (**C**) As in (A) for coupling conductance (g_{coup}). (**D**) As in (A) for total coupling conductance ($g^{\mathrm{tot}}_{\mathrm{coup}}$). (**E**) As in (A) for mean coupling conductance of structurally linked cells. (**F**) As in (A) for number of structural links.

may act in concert to make the cell highly synchronized. We next decomposed how those coupled neighbors influence the hub cell phenotype. We found that the mean intrinsic coupling conductance of a hub cell's structurally linked neighbors was not different (mean ± SD 0.120 ± 0.005 nS vs. 0.119 ± 0.002 nS, $p = 0.36$) (Figure 4.3E) from that of the follower cell's. Instead, the number of structural links was higher for hub cells than for followers (mean ± SD 6.1 ± 0.11 vs. 5.4 ± 0.02, $p < 0.001$) (Figure 4.3F). Together, these observations indicate that the number of cells to which a beta cell is directly coupled may be a key determinant of its propensity to serve as a hub cell in the model.

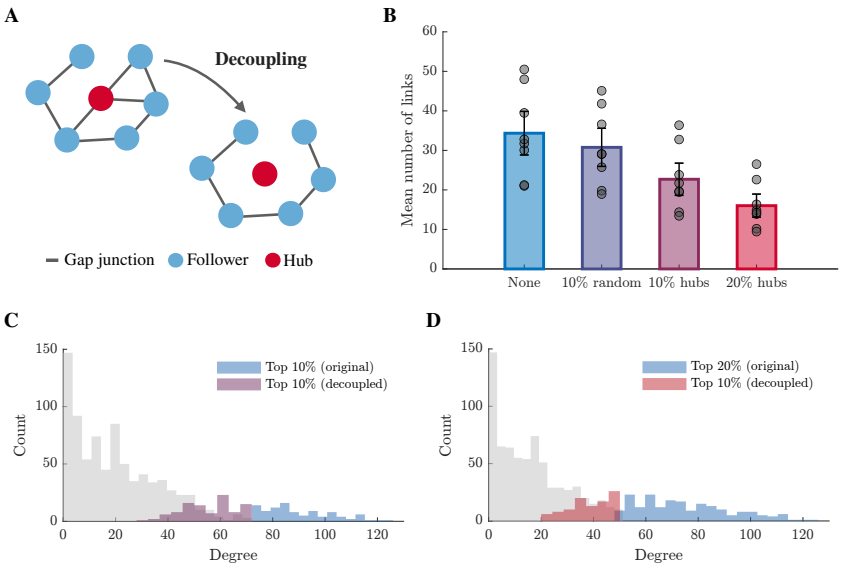

Fig. 4.4: **Analysis of decoupled islet simulations.** (**A**) Schematic of the decoupling process, where the gap junctions of hub cells are removed. (**B**) Mean number of functional links for different decoupled subpopulations. From left to right, the following groups were decoupled: None; 100 random cells; the 100 most functionally linked cells; the 200 most functionally linked cells. The bars indicate the mean degree across all simulated islets ($n = 8$ seeds), whereas the data points represent individual islets. Error bars indicate SEM. (**C**) Degree distribution of the original simulated islet, with cells selected for decoupling ("Top 10% (original)") and the new 100 most functionally linked in the decoupled islet ("Top 10% (decoupled)") indicated. (**D**) As in (C), but decoupling the 200 most functionally linked cells.

4.3.3 Decoupling beta cell subpopulations reveals impaired islet connectivity and potential compensatory mechanisms

To investigate the importance of selected beta cell subpopulations to the total islet synchronization, we ran decoupled simulations on eight different simulated islets. This entailed removing the gap junctions of selected subsets of cells from the simulation and excluding those cells from the subsequent analysis (Figure 4.4A). We compared the effect of decoupling three different groups of cells on the network connectivity, measured by the mean number of functional links (Figure 4.4B). First, we decoupled 100 random cells, in an attempt to study the isolated effect of the decoupling itself. This slightly reduced the mean number of functional links, from 34.3 ± 5.5 to 30.8 ± 4.8 (mean ± SEM) (Figure 4.4B). Decoupling the 10% most functionally linked cells substantially reduced the average connectivity to 22.7 ± 4.1. Finally, decoupling the 20% most functionally linked had the strongest effect, result-

ing in an average number of functional links of 16.0 ± 2.9 in the remaining coupled islet.

With decoupling, we aimed to simulate the effect of cell ablation. Although the total islet synchronization was impaired after decoupling, the islet remained tightly coupled, raising the question of whether other cells can take on the roles of the hubs. To answer this, we identified the 100 most functionally linked cells in the decoupled simulations and examined where those cells belonged in the degree distribution of the original islet. After decoupling the 10% most linked cells, the new 10% most linked group of cells appeared to be on the upper end of the degree spectrum of the remaining cells (Figure 4.4C). Similarly, after decoupling the top 20%, the replacement hubs appeared to be in the next degree percentiles of the original islet (Figure 4.4D). Thus, it is likely that the hierarchy of functional coupling is well described by the degree distribution, and that any cell's position within that distribution (hierarchy) is not markedly altered by removing a reasonably small fraction of highly coupled cells.

4.4 Discussion

In this study, we integrated computational modeling with principles of biological heterogeneity to investigate the defining characteristics of hub cells in pancreatic beta cell networks. Our findings indicate that the hub cell phenotype arises from a combination of metabolic properties and structural connectivity. This dual dependency emphasizes the importance of both autonomous cellular functions and direct cell-cell electrical coupling in regulating insulin secretion and maintaining glucose homeostasis, contributing to novel insights into islet physiology.

We demonstrate that hub cells exhibit significantly higher glycolytic rates (k_{glyc}) compared to follower cells, suggesting that intrinsic metabolic activity is a critical determinant of hub cell functionality. This aligns with previous studies that identified metabolic heterogeneity as a driver of functional differences within beta cell populations [4]. The higher glycolytic activity in hub cells likely facilitates their ability to coordinate the second phase of insulin release, a process essential for maintaining normoglycemia. This suggests that targeting metabolic pathways specific to hub cells could offer a novel approach to enhancing islet function in diabetic conditions.

The role of structural connectivity, via gap junctions, is also essential for defining the hub cell phenotype. Our simulations indicate that hub cells have significantly higher total coupling conductance ($g_{\mathrm{coup}}^{\mathrm{tot}}$), enhancing synchronized activity across the islet. We also decompose this effect by investigating the intrinsic coupling conductance of neighboring cells and the number of structural (direct electrical) links as independent contributors to the hub cell's local electrical coupling. These analyses demonstrate that the difference in $g_{\mathrm{coup}}^{\mathrm{tot}}$ likely stems from the number of cells to which they are directly coupled rather than the degree or coupling conductance of those connected cells. The decoupling experiments emphasize that disrupting gap junctions, specifically in the highly connected hub cells, leads to a decline in co-

ordination across the islet. This highlights the importance of hub cells in ensuring effective propagation of electrical signals and thereby coordination of insulin release.

While the computational model offers valuable insights, it also has limitations. A challenge with the current model is its extremely tight coupling. The $[Ca^{2+}]$ time series are all highly correlated, illustrated by the large threshold ($R_{th} = 0.99975$) required to achieve a power-law degree distribution. This tight coupling makes it difficult to discern clear effects of any manipulation on synchronization or functional organization of the islet. When all cells are that highly correlated, the intricate dynamics and potential heterogeneity within the islet may be obscured. This underscores the importance of exploring various decoupling strategies to reveal underlying patterns and to better understand the functional connectivity within the islet. By selectively decoupling specific groups of cells, we aim to expose the subtle nuances of cellular interactions that are otherwise concealed in a highly coupled system. This also highlights the sensitivity of the islet analysis to the manually chosen threshold. It is essential to solidify the choice of this threshold, and additional experiments should be considered for validation.

Another challenge arises from the significant variability between simulated islets. When different seeds are used to assign randomized parameters to cells, this variability leads to substantial differences in islet behavior and organization, making it difficult to draw consistent conclusions. This issue was especially apparent in the decoupled simulations, where the mean number of functional links varied considerably between seeds. Each set of random parameters can create unique patterns of synchronization and connectivity, complicating generalization. To address this, robust statistical methods and multiple simulations are necessary to capture the range of possible outcomes and to reflect the variability found in real-world islets. Analyzing a wide array of simulations helps us understand the variability and identify consistent patterns.

In the future, extending the model to include pathological conditions, such as diabetes, could provide valuable insights into how hub cell functionality changes with disease states. Furthermore, our results suggest that hub cells could serve as biomarkers for islet health, with potential applications in the early detection of beta cell failure. The integration of computational and experimental approaches will be essential in further explaining the role of hub cells and their potential as targets for preserving islet function.

4.5 Conclusion

Our study highlights the critical role of both autonomous and non-autonomous parameters in defining the beta hub cell phenotype. Employing the extended ChaNoma model, we established that autonomous metabolic factors, such as glycolysis rate, are essential in phenotype differentiation. Non-autonomous factors, including total gap junction coupling conductance and the number of structural links, also play a significant role in hub cell identification. Hub cells act as critical coordinators

within the beta cell network, with their functionality emerging from a delicate balance between metabolic activity and structural connectivity. The seemingly random spatial distribution of hub cells suggests that location is not a significant factor, at least in our model of a beta cell islet. Lastly, our decoupling experiments emphasize the importance of hub cells in maintaining network synchronization. Decoupling these highly coupled cells leads to significant disruptions. Still, the islet remains highly synchronized, suggesting that other cells may partially compensate for the missing hub cells, thereby ensuring continued functionality despite disruptions. These findings contribute to the understanding of islet physiology and suggest new avenues for diagnostics and potential therapeutic interventions in diabetes.

References

1. Victoria Salem, Luis Delgadillo Silva, Kinga Suba, Eleni Georgiadou, S. Neda Mousavy Gharavy, Nadeem Akhtar, Aldara Martin-Alonso, David C. A. Gaboriau, Stephen M. Rothery, Theodoros Stylianides, Gaelle Carrat, Timothy J. Pullen, Sumeet Pal Singh, David J. Hodson, Isabelle Leclerc, A. M. James Shapiro, Piero Marchetti, Linford J. B. Briant, Walter Distaso, Nikolay Ninov, and Guy A. Rutter. Leader β-cells coordinate Ca2+ dynamics across pancreatic islets in vivo. Nature Metabolism, 1(6):615–629, June 2019.
2. Vira Kravets, JaeAnn M. Dwulet, Wolfgang E. Schleicher, David J. Hodson, Anna M. Davis, Laura Pyle, Robert A. Piscopio, Maura Sticco-Ivins, and Richard K. P. Benninger. Functional architecture of pancreatic islets identifies a population of first responder cells that drive the first-phase calcium response. PLOS Biology, 20(9):e3001761, September 2022.
3. Natalie R. Johnston, Ryan K. Mitchell, Elizabeth Haythorne, Maria Paiva Pessoa, Francesca Semplici, Jorge Ferrer, Lorenzo Piemonti, Piero Marchetti, Marco Bugliani, Domenico Bosco, Ekaterine Berishvili, Philip Duncanson, Michael Watkinson, Johannes Broichhagen, Dirk Trauner, Guy A. Rutter, and David J. Hodson. Beta cell hubs dictate pancreatic islet responses to glucose. Cell Metabolism, 24(3):389–401, September 2016.
4. Richard K. P. Benninger and Vira Kravets. The physiological role of β-cell heterogeneity in pancreatic islet function. Nature Reviews Endocrinology, 18(1):9–22, January 2022.
5. Jennifer K Briggs, Anne Gresch, Isabella Marinelli, JaeAnn M Dwulet, David J Albers, Vira Kravets, and Richard K. P. Benninger. β-cell intrinsic dynamics rather than gap junction structure dictates subpopulations in the islet functional network. eLife, 12:e83147, November 2023.
6. Richard K. P. Benninger, Min Zhang, W. Steven Head, Leslie S. Satin, and David W. Piston. Gap Junction Coupling and Calcium Waves in the Pancreatic Islet. Biophysical Journal, 95(11):5048–5061, December 2008.
7. Thomas H Hraha, Matthew J Westacott, Marina Pozzoli, Aleena M Notary, P Mason McClatchey, and Richard K. P. Benninger. Phase transitions in the multi-cellular regulatory behavior of pancreatic islet excitability. PLOS Computational Biology, 10(9):e1003819, 2014.
8. JaeAnn M. Dwulet, Nurin W.F. Ludin, Robert A. Piscopio, Wolfgang E. Schleicher, Ong Moua, Matthew J. Westacott, and Richard K.P. Benninger. How Heterogeneity in Glucokinase and Gap-Junction Coupling Determines the Islet [Ca2+] Response. Biophysical Journal, 117(11):2188–2203, December 2019.
9. Chae Young Cha, Yasuhiko Nakamura, Yukiko Himeno, JianWu Wang, Shinpei Fujimoto, Nobuya Inagaki, Yung E Earm, and Akinori Noma. Ionic mechanisms and Ca2+ dynamics underlying the glucose response of pancreatic β cells: A simulation study. Journal of General Physiology, 138(1):21–37, July 2011.
10. Marko Šterk, Yaowen Zhang, Viljem Pohorec, Eva Paradiž Leitgeb, Jurij Dolenšek, Richard K. P. Benninger, Andraž Stožer, Vira Kravets, and Marko Gosak. Network representation of

multicellular activity in pancreatic islets: Technical considerations for functional connectivity analysis. PLOS Computational Biology, 20(5):e1012130, May 2024.
11. Chae Young Cha, Enrique Santos, Akira Amano, Takao Shimayoshi, and Akinori Noma. Time-dependent changes in membrane excitability during glucose-induced bursting activity in pancreatic β cells. Journal of General Physiology, 138(1):39–47, 2011.
12. Andraž Stožer, Marko Gosak, Jurij Dolenšek, Matjaž Perc, Marko Marhl, Marjan Slak Rupnik, and Dean Korošak. Functional connectivity in islets of Langerhans from mouse pancreas tissue slices. PLOS Computational Biology, 9(2):e1002923, 2013.

Chapter 5
Exploring the intrinsic and extrinsic determinants of heterogeneity in a β-cell network

Anwar Khaddaj, Shane Browne, Woori Choi, Vira Kravets, and Andrew G. Edwards

Abstract Pancreatic islets are micro-organs composed of multiple endocrine cell types. β-cells are the most common of these and are highly heterogeneous in both their intrinsic properties, such as ion channel conductances and metabolic activity, and extrinsic properties, including gap junction coupling and paracrine signaling. Capturing these diverse sources of heterogeneity is essential for computational models that aim to reproduce islet function. We evaluate two established multicellular models, the coupled Cha-Noma model of the mouse β-cell network, and the Riz human model. Prior work with these two models suggest that the Cha-Noma model involves minimal intrinsic heterogeneity and therefore bursts with highly synchronized activity, whereas heterogeneity in the Riz model prescribed from *in vitro* patch-clamp results in highly unsynchronized behavior of the coupled network. We hypothesize that adjusting the number of bursting cells in both model formulations may invoke more physiologically realistic network coordination. We applied a categorical sensitivity analysis to establish which parameters are most important for determining bursting in single cells of the Riz model. We also introduced new heterogeneity (based on single-cell gene expression) in parameters that had previously been treated as invariant among β-cells. We hypothesized that introducing heterogeneity in the small conductance Ca^{2+} K^+ channel in particular could promote a

Anwar Khaddaj
School of Mathematical and Statistical Sciences, Arizona State University, USA

Shane Browne
Department of Bioengineering, University of California San Diego, USA

Woori Choi
Department of Internal Medicine, University of California Davis, USA

Vira Kravets
Department of Bioengineering and Department of Pediatrics, University of California San Diego, USA

Andrew G. Edwards (corresponding author)
Department of Computational Physiology, Simula Research Laboratory, Norway e-mail: andy@simula.no

K. J. McCabe, *Computational Physiology*, Simula SpringerBriefs on Computing 20, https://doi.org/10.1007/978-3-032-28826-4_5

higher proportion of bursting cells. Lastly, both models fail to incorporate the influences of non-β-cells. We introduced paracrine signaling between α and β-cells into the coupled Cha-Noma model and showed it plays a role in accelerating the response time of β-cells to acute glucose stimulation (i.e. promotes a 1st responder phenotype).

5.1 Introduction

The Islet of Langerhans is a 'micro-organ' consisting of several hormone-secreting cells. These endocrine cells include insulin-secreting β-cells, glucagon-secreting α-cells, and somatostatin-secreting δ-cells. The predominant cell type in both human and mouse islets are β-cells [1, 2, 3, 4, 5]. β-cells have been shown to have significant heterogeneity in both intrinsic and extrinsic parameters. This intrinsic heterogeneity includes variation in ion channel conductances [6] and in metabolic activity [7, 8, 9, 10]. Furthermore, heterogeneity in extrinsic characteristics has been broadly observed and is altered in disease, particularly type 2 diabetes. *In situ* patch-clamp of peripheral islet cells [11] *In vitro* patch-clamp of dissociated β-cell pairs [12], as well as non-invasive fluorescence recovery after photobleaching experiments [13], have shown significant heterogeneity in gap junction coupling between β-cells. Additionally, extrinsic heterogeneity in paracrine signaling is likely to exist within the islet due to non-uniformity in heterotypic contacts between cells that are able to engage in paracrine signaling over short distances [14, 15, 1].

For computational models of islets to be informative, there must be a proper reconstruction of both these intrinsic and extrinsic forms of heterogeneity. Published computational β-cell models have attempted to reconstruct this heterogeneity, and here we interrogate two of them: (1) the coupled Cha-Noma mouse model [16]; and, (2) a multicellular version of the Riz human model [17, 18]. Importantly, cursory inspection of glucose-dependent activity in both of these models indicates that neither captures function that is truly representative of intact β-cell networks (Figure 5.2). The coupled Cha-Noma model exhibits activity (indicated by intracellular Ca^{2+}) that is much more coordinated and synchronous than is observed in experiments, while the multicellular Riz model is excessively dyssynchronous and uncoordinated. By quantifying the glucose-induced excitability of the β-cell populations used (i.e. the effects of intrinsic heterogeneity) in both models (Figure 5.1), we observed that the coupled Cha-Noma model had a much higher proportion of bursting cells compared to the multicellular Riz model. Thus, we first hypothesized that redressing this difference by modifying bursting-specific intrinsic heterogeneity of the cell population in the multicellular Riz model might rectify this coordination issue.

Moreover, though both computational models introduce heterogeneous parameters, not all intrinsic parameters are heterogeneous in the population due to limited availability of human-specific patch-clamp data. In the multicellular Riz model, one such parameter is the maximum conductance of the small-conductance calcium-activated potassium (SK) channel. Small-conductance calcium-activated potassium

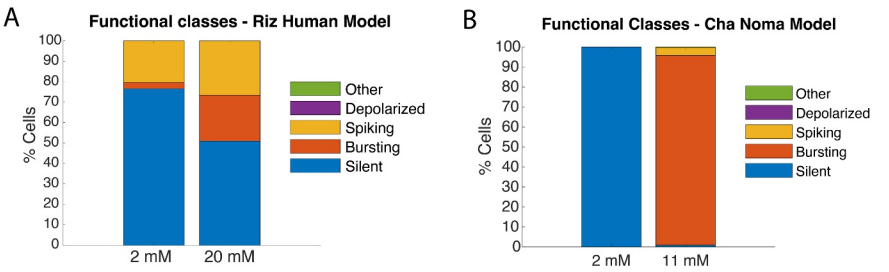

Fig. 5.1: Classification of computation models into different excitability phenotypes. (A) Human Riz model with heterogeneous parameters. (B) Mouse Cha-Noma model with heterogeneous parameters.

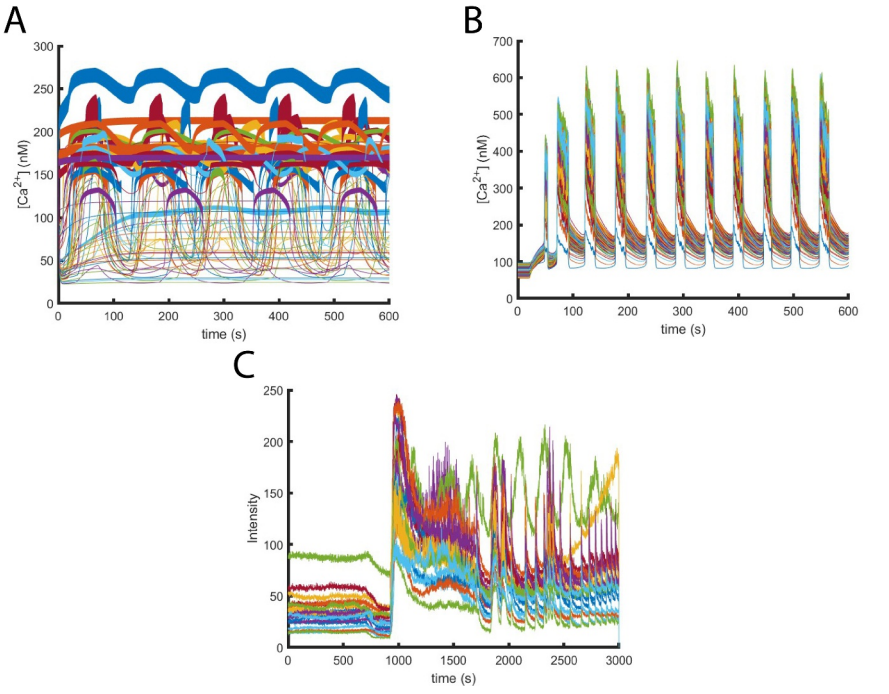

Fig. 5.2: Computational and experimental calcium traces. (A) Calcium traces for 60 cells in the coupled Riz model at 20 mM glucose. (B) Calcium traces for 1000 cells in the coupled Cha-Noma model when excited from 2 mM to 11 mM glucose at t = 20 s. (C) Experimental calcium traces from an isolated mouse islet when excited from 2 mM to 11 mM glucose.

(SK) channels are key regulators of pancreatic β-cell excitability. Activated by elevations in intracellular calcium, SK channels generate after-hyperpolarizing currents that contribute to membrane repolarization and burst termination. By shaping oscillatory activity, SK channels influence the frequency and duty cycle of β-cell bursts, thereby indirectly modulating insulin secretion through their impact on calcium oscillations and granule exocytosis [19]. The assumption of uniform conductance across the population oversimplifies β-cell electrophysiology and fails to account for molecular variability that may be physiologically important for network function. Single-cell transcriptomic profiling of human pancreatic islets in [20] can provide an approximation of ion channel expression at the resolution of individual cells. Our reanalysis of the dataset presented by Segerstolp et al.[20], indicates that KCNN3 transcripts, encoding SK subtype 3, are consistently expressed at quantifiable levels in β-cells, whereas other SK isoforms (KCNN1, KCNN2, KCNN4) are barely detectable. These results suggest that KCNN3 transcript expression constitutes the main detectable SK channel transcript in human β-cells, and we hypothesized that introducing variability defined by cell-to-cell KNN3 transcript level may provide a new basis for modulating bursting across the modeled Riz β-cell population.

Lastly, it is notable that both the coupled Cha-Noma model and the coupled Riz model only include β-cells. Consequently, only intrinsic heterogeneity and extrinsic heterogeneity in the form of gap junction coupling are accounted for. However, paracrine signaling is another important determinant of islet function, and particularly regulation of the β-cell network. Application of exogenous glucagon and glucagon-like-peptide-1 (GLP-1) has been shown to potentiate glucose-stimulated insulin secretion (GSIS), and there is evidence to suggest that endogenous production of glucagon and GLP-1 from α-cells acts on β-cells via paracrine signaling through the glucagon-like-peptide-1 receptor (GLP-1R) [21, 22, 23]. Thus, α-β-cell communication is an important determinant of islet function. This paracrine signaling might have further implications for β-cell subpopulation development, as it has been hypothesized that the β-cell subpopulation termed 1$^{\text{st}}$ responders is preferentially located near α-cells. [24, 25].

In this work, we use sensitivity analysis to help reconstruct realistic network coordination by varying the most heterogeneous parameters in the multicellular Riz model that are the most sensitively associated with the bursting phenotype. We also incorporate SK conductance heterogeneity into simulations in order to better reflect physiological diversity of SK expression in β-cell populations. Finally, we set out to introduce a model for α-β-cell communication into the coupled Cha-Noma model, and quantify the influence of this signaling on indicators of 1^{st} responder behavior near α-cells.

5.2 Methods

5.2.1 Sensitivity analysis

To study the intrinsic heterogeneity of β-cells within an islet, we examine how variations in model parameters influence the responses of β-cells to elevated glucose. To achieve this, we employ a sensitivity analysis technique to quantify the impact of heterogeneous parameters on model outputs. Our study focuses on a human islet population of 3000 cells from which a subset of $n_b = 774$ β-cells is randomly sampled. We utilize the β-cell Riz model described in [26], which has $n_x = 15$ state variables and $n_p = 86$ parameters and can be formulated abstractly as an ordinary differential equation (ODE):

$$x'(t) = f(t, x(t), p), \qquad t \in (t_0, t_f), \tag{5.1a}$$

$$x(t_0) = x_0, \tag{5.1b}$$

where $x : \mathbb{R} \to \mathbb{R}^{n_x}$ represents the state variables, $x_0 \in \mathbb{R}^{n_x}$ represents the initial conditions, $f : \mathbb{R}^{1+n_x+n_p} \to \mathbb{R}^{n_x}$, and $p \in \mathbb{R}^{n_p}$ represents the parameters. Out of the 86 parameters, only 16 parameters are varied during the simulations, and these are grouped into a parameter vector $p^S \in \mathbb{R}^{n_{p^S}=16}$:

$$p^S = [V_{GK,max}, K_{GK}, g_{Kv}, g_{BK}, g_{KATP}, g_{CaL}, g_{CaPQ}, g_{CaT}, V_{hNa,high}, n_{hNa,high}, V_{mNa,high}, g_{Na,high}, V_{hNa,low}, n_{hNa,low}, V_{mNa,low}, g_{Na,low}],$$

The descriptions of these heterogeneous parameters are provided in Table 5.1 below.

Parameter	Description
$V_{GK,max}$	Maximum flux of GK
K_{GK}	Glucose concentration at half-maximal activation of GK
g_{Kv}	I_{Kv} maximal conductance
g_{BK}	I_{BK} maximal conductance
g_{KATP}	I_{KATP} maximal conductance
g_{CaL}	I_{CaL} maximal conductance
g_{CaPQ}	I_{CaPQ} maximal conductance
g_{CaT}	I_{CaT} maximal conductance
$V_{hNa,high}$	$I_{Na,high}$ half inactivation potential
$n_{hNa,high}$	$I_{Na,high}$ inactivation slope factor
$V_{mNa,high}$	$I_{Na,high}$ half activation potential
$g_{Na,high}$	$I_{Na,high}$ maximal conductance
$V_{hNa,low}$	$I_{Na,low}$ half inactivation potential
$n_{hNa,low}$	$I_{Na,low}$ inactivation slope factor
$V_{mNa,low}$	$I_{Na,low}$ half activation potential
$g_{Na,low}$	$I_{Na,low}$ maximal conductance

Table 5.1: Heterogeneous parameters in the β-cells ODE model.

Using this framework, we implement a categorical feature-based sensitivity analysis to quantify how the heterogeneous parameters influence different β-cell phenotypes (or features). The dynamic behaviors of the β-cells are classified into $n_c = 5$ phenotypes: silent, depolarized, spiking, bursting, and other. These phenotypes are determined from the raw membrane potential time-series by the algorithm in Figure 5.3. We applied logistic regression to binarized classification of each phenotype and standardized parameter deviations. The associated input matrix $X \in \mathbb{R}^{n_b \times n_p s}$ contains the standardized parameter values for each of the n_b cells to account for differences in scale before fitting the logistic regression model.

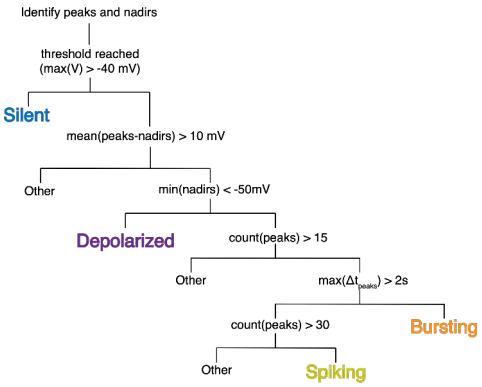

Fig. 5.3: A phenotype classification algorithm used to determine the dynamic behavior of β-cells in response to glucose. The algorithm depends on the simulated voltage behavior in terms of its highest points (peaks), lowest points (nadirs), and peak-to-peak interval (Δt_{peaks}). More than 1000 automatic classifications were randomly selected and verified for correctness by the same analyst. This algorithm is very similar to the one developed in [27] on a heterogeneous population built from the same dataset.

5.2.2 Transcriptomic analysis and modeling approach

We reanalyzed the single-cell RNA sequencing dataset in [20], which profiled over 2,000 pancreatic islet cells from healthy donors and patients with type 2 diabetes. After filtering for β-cells, we performed separate analyses for healthy and diabetic groups, quantifying KCNN3 transcript expression as a proxy for SK channel abundance. Normal, log-normal, and gamma distributions were fitted to transcript-per-million (TPM) values of KCNN3. In β-cells from healthy donors, expression followed a skewed distribution that was best captured by a log-normal model ($r^2 \approx 0.52$). In contrast, β-cells from patients with type 2 diabetes showed lower expression and greater variability, and none of the tested models provided a satisfactory fit. For

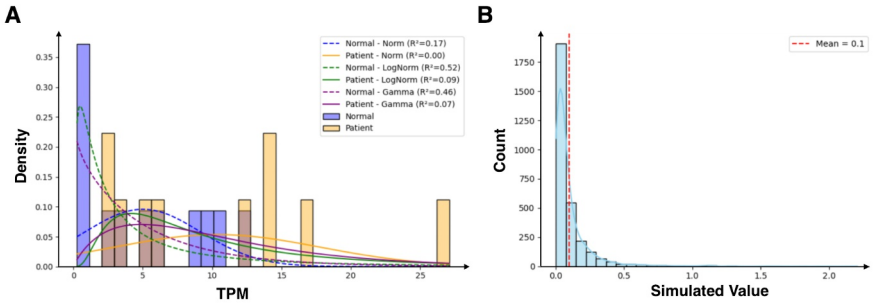

Fig. 5.4: Distribution of KCNN3 expression from RNA-seq and parameterization of g_{SK}. (A) Distribution fitting of *KCNN3* transcript expression. Normal, log-normal, and gamma distributions were fitted to TPM values of *KCNN3* in β-cells. In healthy donors, expression was best captured by a log-normal distribution ($R^2 \approx 0.52$) (B) Parameterization of g_{SK} from the fitted distribution. g_{SK} was parameterized using values sampled from the log-normal distribution of *KCNN3* transcript expression in healthy β-cells, with the mean aligned to 0.1 nS/pF. All simulations were run for 90 s.

simulations, SK conductance (g_{SK}) was parameterized using values sampled from the log-normal distribution of KCNN3 transcript expression observed in healthy β-cells, with the mean set to 0.1 nS/pF. The SK channel current was modeled using a standard Hill-type formulation:

$$I_{SK} = g_{SK} \cdot \frac{[Ca^{2+}]^n}{K_{SK}^n + [Ca^{2+}]^n} \cdot (V - V_K)$$

In this equation, g_{SK} denotes the maximal SK conductance, $[Ca^{2+}]$ represents the intracellular calcium concentration, K_{SK} is the half-activation constant, and n is the Hill coefficient describing the cooperativity of calcium binding. The term $(V - V_K)$ corresponds to the driving force for potassium ions, with V_K being the potassium reversal potential. This formulation captures the calcium-dependent activation of SK channels and their hyperpolarizing influence on the membrane potential. Additional simulations were conducted with fixed g_{SK} values of 0.001, 0.01, 0.1, and 1 nS/pF for comparison. The value of 0.1 nS/pF served as the reference, corresponding to the conductance used in prior modeling studies [26] based on experimental data. All simulations, both fixed and heterogeneous, were run for 90 s. Cell phenotypes were classified according to the same criteria described in the previous section.

5.2.3 α-β-Cell communication

5.2.3.1 Updated Cha-Noma and Coupled Cha-Noma Model

A previously published mathematical model describing a single mouse β-cell [28], termed the Cha-Noma model, as well as an extension of that model to an islet [16], termed the coupled Cha-Noma model, was used as a starting point. Both describe the dynamic activity of β-cell membrane potential, V_m, as a function of 8 plasma membrane currents and 3 ion transporters. The time-dependent change in voltage for the Cha-Noma model is written as follows:

$$C_m \frac{dV_m}{dt} = I_{CaV} + I_{TRPM} + I_{SOC} + I_{bNSC} + I_{KDr} + I_{KCa(BK)} + I_{KCa(SK)} + I_{K_{ATP}} + I_{NaCa} + I_{PMCA} + I_{NaK}.$$

The coupled Cha-Noma model extends this model with the introduction of a coupling current to the right-hand side of the above equation,

$$I^i_{coup} = \sum_{j=1}^{n} \frac{(g^i_{coup} + g^j_{coup})}{2} [V^i_m - V^j_m]$$

as well as the introduction of heterogeneity in several cellular parameters. This heterogeneity is the same as described in [29]. Both the single cell and couple Cha-Noma models were updated to include the effect of α-β-cell communication on ATP-sensitive K^+channels, by introducing a GLP-1R signaling model described in [30]. This allowed GLP-1 concentration to stimulate production of intracellular cyclic-AMP and, further, Protein Kinase A activity. The effects of activated PKA (PKA_a) on K_{ATP} channels were modeled using a formulation from [31] in which the available MgADP to alter the K_{ATP} channel open probability decreases as PKA_a increases, shown as follows:

$$MgADP_f = 0.055 * f_{KPK_a} * ADP_f$$

$$f_{KPK_a} = \frac{1}{1 + k_{KPK_a} * PKA_a}$$

$$O_{KATP} = \frac{0.08(1 + 2\frac{MgADP_f}{k_{dd}}) + 0.89(\frac{MgADP_f}{k_{dd}})^2}{(1 + \frac{MgADP_f}{k_{dd}})^2(1 + 0.45\frac{MgADP_f}{k_{td}} + \frac{ATP_f}{k_{tt}})}$$

The open probability then affects the K_{ATP} channel current as follows:

$$I_{KATP} = g_{KATP} * O_{KATP} * (V_m - E_K)$$

This resulted in an updated model, shown schematically in Figure 5.5.

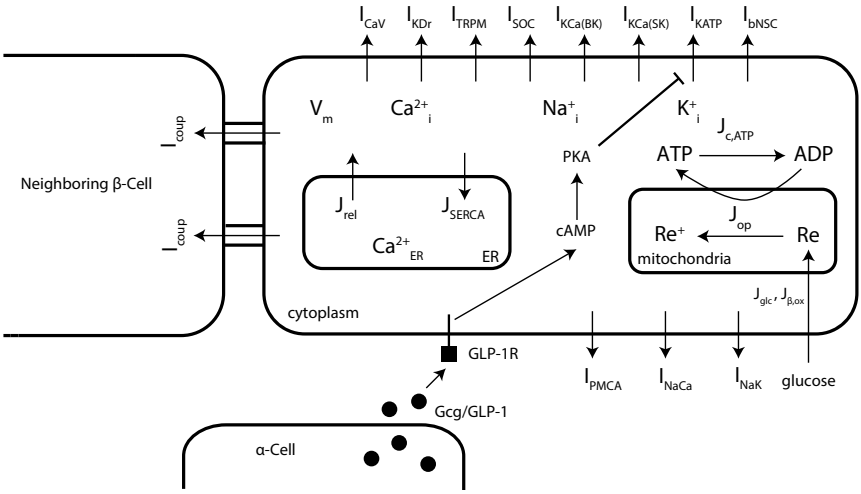

Fig. 5.5: Updated coupled Cha-Noma model, modified from [28]. This updated model incorporates α-β-cell communication via GLP-1 acting on the GLP-1R, resulting in an inhibitory effect on K_{ATP} channels. The updated single-cell Cha Noma model is similar, without the inclusion of β-β-cell coupling.

To introduce α-β-cell communication into the coupled Cha-Noma model, it was also necessary to alter the islet structure. This was necessary as the previous iteration of the coupled Cha-Noma model only included β-cells, but the introduction of α-β-cell communication requires two things: 1) the locations of α-cells, and 2) which β-cells are located close enough to an α-cell to be affected by paracrine signaling. Both of these requirements were met by applying a modified version of the simulated annealing algorithm developed previously by Felíx-Martinez et al. [14, 15]. This allowed the reconstruction of a mouse islet from published immunofluorescence data that included the cell locations for both α-cells and β-cells [32]. To determine cell contacts, a threshold between two cell surfaces of 6 μm was used. This threshold was chosen for the fact that it gave a similar β-β link distribution to that in the coupled Cha-Noma model, allowing for comparisons between the two versions of the models if so desired. The updated islet structure and β-β structural degree distributions can be seen in Figure 5.6.

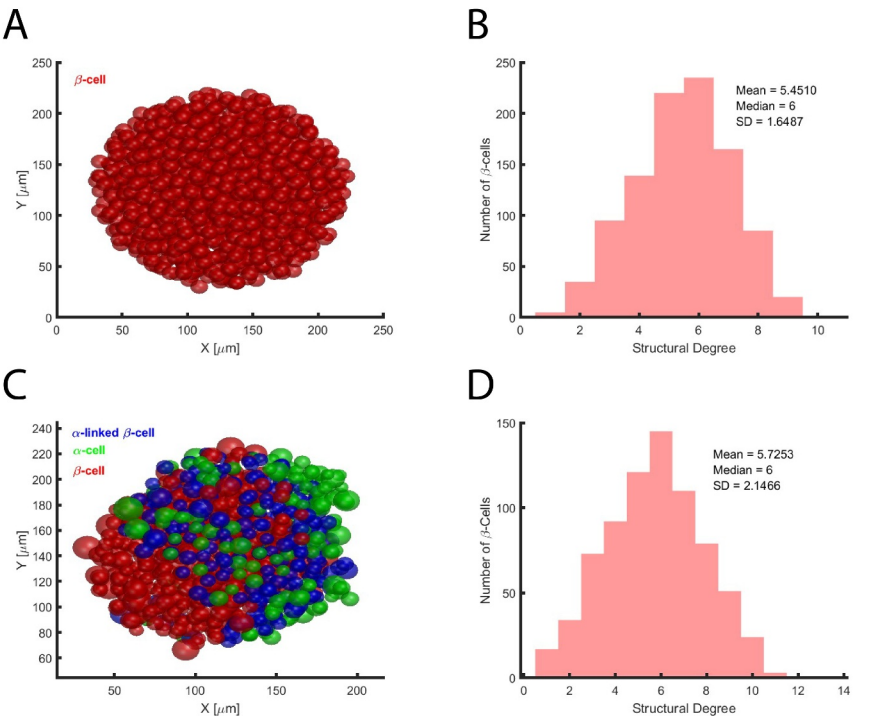

Fig. 5.6: Updated islet structure. (A) Islet structure in the coupled Cha-Noma model. (B) β-β structural distribution for the coupled Cha-Noma model. (C) Updated islet structure that includes α-cells. (D) β-β structural distribution for the updated version of the coupled Cha-Noma model

5.2.3.2 Cha-Noma Model Simulations

Simulations were run using both the updated single-cell Cha-Noma model and the updated coupled Cha-Noma model. The parameters in the single-cell model were set to the mean of those in the coupled Cha-Noma model. For both models, the applied glucose followed a step function, in which glucose was raised from 2 mM to 11 mM at 20 s. For simulations with the coupled model, two sets were run. In the first, [GLP-1] was set to 0 nM across all β-cells. This was done to represent no α-β-cell communication. In the second, [GLP-1] was set to 20 nM only for α-linked β-cells. This was done to represent an islet with α-β-cell communication. A concentration of 20 nM was chosen as it produces maximal stimulation of the GLP-1R. A total of 6 seeds with randomized cellular heterogeneity were used while maintaining the same islet structure.

5.2.3.3 First Responder and Time of Response Analysis

For the multicellular model, the time of response for individual β-cells was calculated using individual calcium traces and a custom MATLAB script. Time of response was calculated as the point at which $[Ca^{2+}]$ reached 25% of its maximum value relative to the steady state $[Ca^{2+}]$ during 2 mM. This time of response was then made relative to the time at which glucose was elevated by subtracting 20 s. A threshold of 25 % was chosen as it gave reasonable results upon visual inspection. First responders were set as the 75 fastest responding cells (out of 750 total). Some examples of the points chosen using this method can be seen in Figure 5.7. For the single-cell model, time of response could be determined by hand.

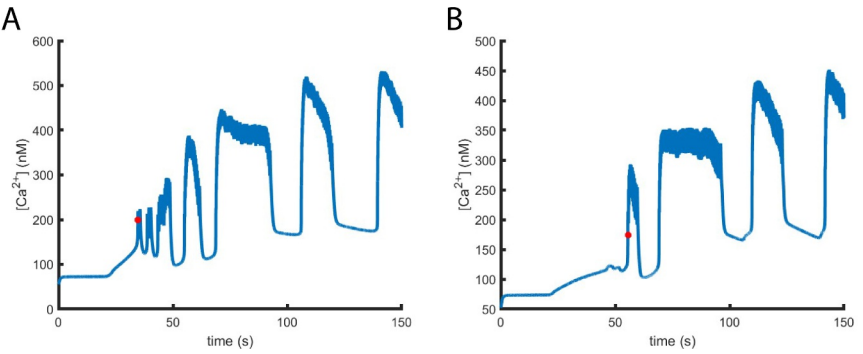

Fig. 5.7: Example time of response points. (A) Example in which the point the cell is presumed to be responding is indicated in red. (B) Example in which the point the cell is presumed to be responding is indicated in red.

5.3 Results

5.3.1 Sensitivity Analysis of Riz Model

As mentioned in the methods, we simulated the Riz (human) β-cell population model at a glucose concentration of 20 mM for 600 s. We the phenotype classification algorithm in Figure 5.3 and determine the frequency of the resulting phenotypes as shown in Figure 5.8 below.

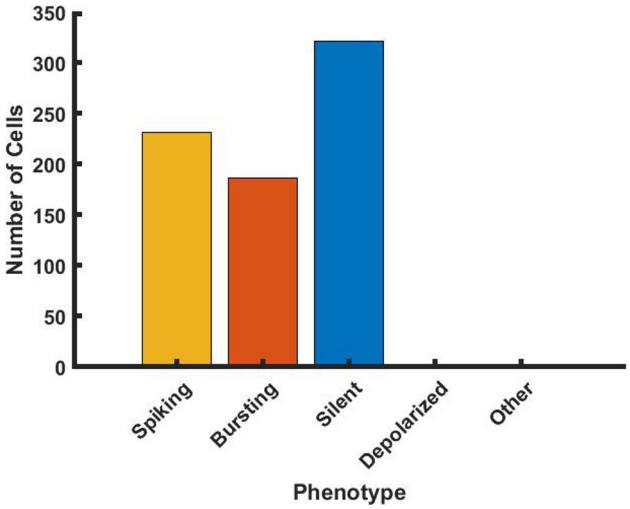

Fig. 5.8: Occurrence of phenotypes of β-cells in Riz model in the case of 20 mM glucose.

The predominant phenotypes are spiking, bursting, and silent, with the remaining phenotypes (depolarized and other) accounting for $< 1\%$ of cells. Thus, we disregard the other two phenotypes for our logistic regression sensitivity analysis because those lesser phenotypes would be dramatically underpowered and determinant parameters would not be reliably identifiable. Recall from the methods that the logistic regression approach used has an input matrix $X \in \mathbb{R}^{744\times16}$ with 744 β-cells and 16 parameters. This matrix includes two groups of parameters that determine whether the Na^+ current exhibits high or low steady-state voltage dependence. As a result, each cell contains 4 columns in which 1 group of Na^+ current parameters that are zero (because that form of the current is not expressed). This results in a rank-deficient structure, which leads to an ill-conditioned logistic regression problem. To address this, we reduce the dimension of the input matrix X by consolidating the nonzero entries of Na^+ current parameters, resulting in a simplified matrix $X^S \in \mathbb{R}^{744\times12}$. Now, we apply the logistic regression approach with the updated input matrix X^S to retrieve a regression coefficient matrix containing the sensitivities of the different parameters for each phenotype. These are plotted in 5.9 below.

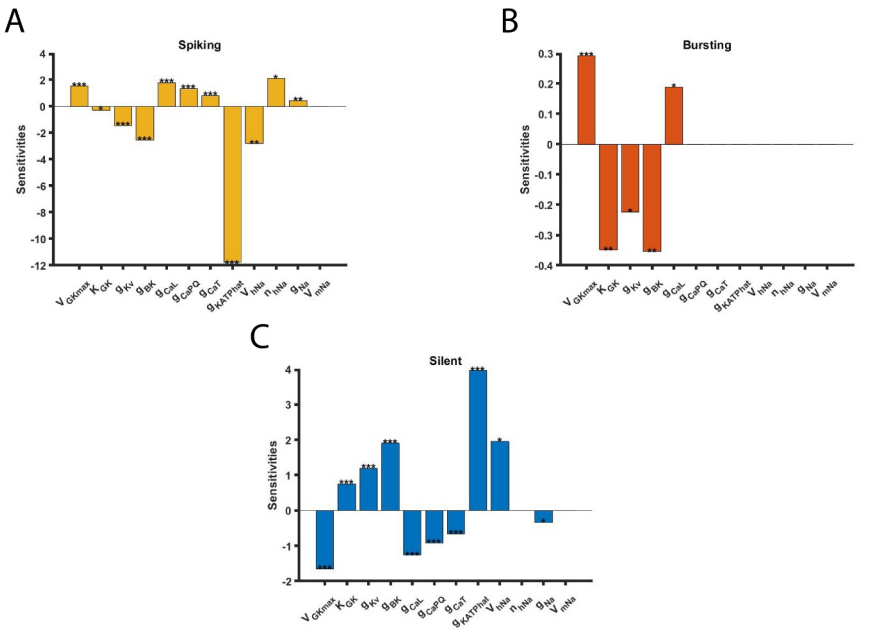

Fig. 5.9: Sensitivity analysis. (A) Parameter sensitivities for spiking phenotype (B) Parameter sensitivities for bursting phenotype (C) Parameter sensitivities for silent phenotype. (*p-value<0.05, **p-value<0.01, and ***p-value<0.001).

Figure 5.9 reveals that g_{KATP}, g_{BK}, and V_{hNa} are the most sensitive parameters in the case of both spiking and silent phenotypes and K_{GK}, g_{BK}, and $V_{GK,\max}$ are the most sensitive parameters for the bursting phenotype. Since we are interested in exaggerating the bursting phenotype, we modulated the variability of the most sensitive parameters for the bursting phenotype by multiplying the mean of the distribution that generates these parameter values by half for parameters K_{GK} and g_{BK} and the mean of the distribution governing $V_{GK,\max}$ by 2. We run the simulation of the human population again, generating the new phenotypes and then assess the change in occurrence of each phenotype at the same high glucose concentration (20 mM). This change is reflected in Figure 5.10 below.

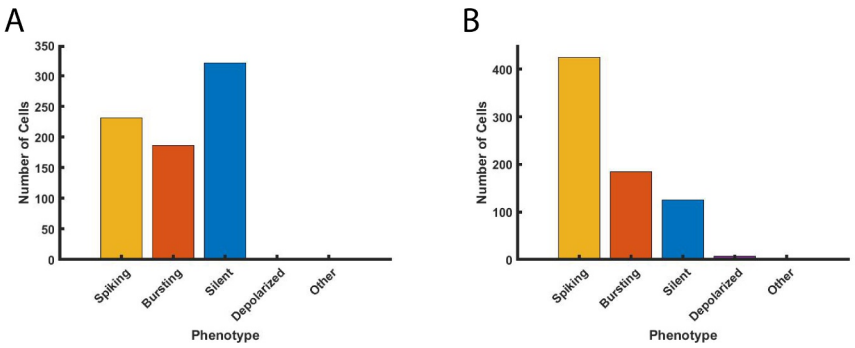

Fig. 5.10: Occurrence of phenotypes of β-cells in Riz model in the case of 20 mM glucose. (A) before changing the variability of the most sensitive parameters for the bursting phenotype (B) after changing the variability of the most sensitive parameters (K_{GK}, g_{BK}, and $V_{GK,\max}$) for the bursting phenotype.

Counter to our expectations, this approach exaggerated the prevalence of the spiking phenotype in the modified population, rather than enhancing the prevalence of bursting. This is because, even though K_{GK}, g_{BK}, and $V_{GK,\max}$ are the most sensitive determinants of bursting, they are also sensitive modulators of spiking, and reciprocally so 5.9. As a result, they are not independently able to exaggerate the bursting phenotype within the population. Thus, we next investigated the effect of targeting the variability of the SK current in the Riz model, which, as mentioned above, was previously implemented as invariant within the β-cell population.

5.3.2 Comparison of β-cells phenotypes under fixed and heterogeneous SK conductance

To investigate how variability in SK channel conductance influences β-cells electrical behavior, we compared cell phenotypes generated under fixed SK conductance values (0.001, 0.01, 0.1, and 1 nS/pF) with those observed in heterogeneous populations sampled from the log-normal distribution of KCNN3 transcript expression. While distribution fitting confirmed that KCNN3 expression in β-cells follows a log-normal pattern in healthy donors, the central question was whether such heterogeneity in SK conductance would affect the diversity of electrophysiological outcomes in our model. Simulations with fixed SK conductance values revealed distinct trends across groups. Both lower-conductance groups (0.001 and 0.01 nS/pF) exhibited more bursting and spiking than the reference value of 0.1 nS/pF. Within these, the 0.01 nS/pF group showed the highest proportion of bursting activity but reduced spiking compared with the 0.001 nS/pF group. In contrast, the 0.1 nS/pF group displayed fewer active cells overall, with reduced spiking and bursting but a higher proportion of silent states than either of the lower-conductance groups. At

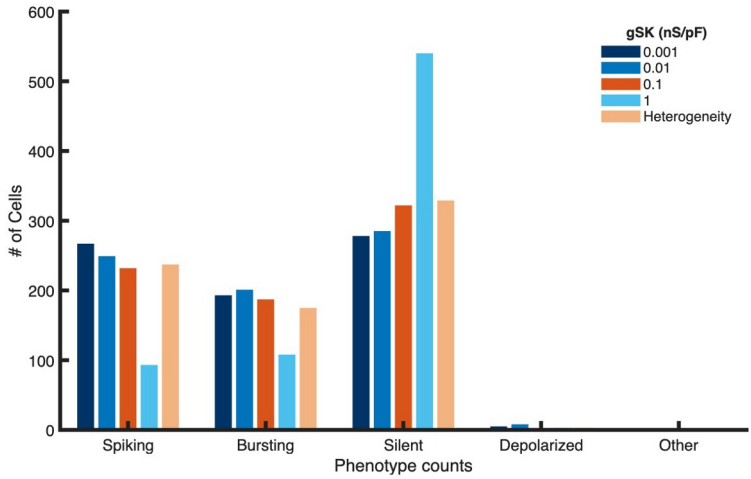

Fig. 5.11: Comparison of β-cell phenotype analysis under fixed and heterogeneous SK conductance. Phenotypes were classified as spiking, bursting, silent, depolarized, or other. Fixed-conductance groups were simulated at 0.001, 0.01, 0.1 (reference), and 1 nS/pF. In addition, a heterogeneous group was generated by sampling g_{SK} values from the log-normal distribution of *KCNN3* transcript expression obtained from RNA-seq data, with the mean aligned to 0.1 nS/pF. All simulations were run for 90 s.

the highest conductance of 1 nS/pF, most cells became silent, reflecting excessive repolarizing drive that strongly suppressed excitability. When SK conductance values were sampled from the log-normal distribution of KCNN3 transcript expression, the simulated population exhibited a mixture of spiking, bursting, and silent cells. The overall distribution of phenotypes was similar to that observed at the reference value of 0.1 nS/pF, which has been used in previous models based on experimental data. This similarity indicates that incorporating heterogeneity does not disrupt the established parameterization of the model or require compensatory adjustments of other parameters. Instead, the introduction of a heterogeneous population reflects the physiological reality that SK channel expression varies across β-cells, while maintaining compatibility with the existing model framework. Thus, the key contribution of this approach is that it updates the model toward a more faithful representation of biological diversity without sacrificing internal consistency.

5.3.3 GLP-1 mediated inhibition of β-cell I_{KATP} plays a subtle but measurable role in promoting 1st responder behavior

As mentioned in the methods, α-β-cell communication was introduced into both the Cha-Noma model and the coupled Cha-Noma model. The effect was modeled as an inhibition of the K_{ATP} channel. To first get an idea of how the average cell would be affected by α-β-cell communication, the single-cell model was run with various applied concentrations of GLP-1 (0, 0.1, 1, 10, 20) nM. At maximal stimulation (20 nM GLP-1), the calcium curve was leftward shifted by 2 s. This is not a large effect, and likely to be at the border of detectability in analogous experiments, but given that it only involves one of many known influences of GLP-1 signaling on β-cell excitability, it suggests that this mode of α-β-cell communication may be quantitatively important in the first phase glucose response.

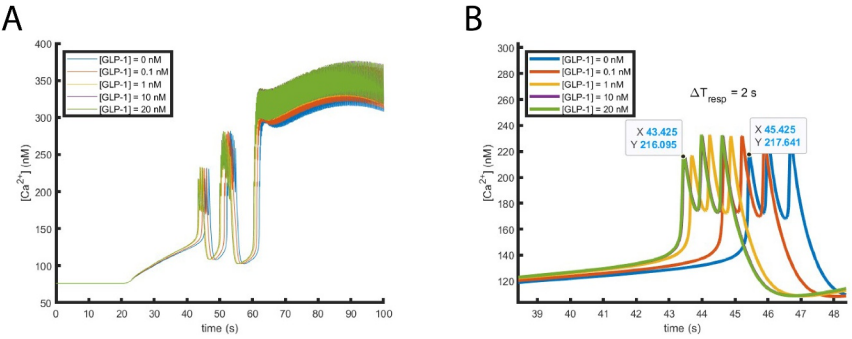

Fig. 5.12: Effects of GLP-1 stimulation on single-cell model. (A) Effects of 0, 0.1, 1, 10, and 20 nM GLP-1 stimulation on the 1st phase response. (B) Zoomed in version of A, showing a maximal leftward shift in time of response of 2 s.

Next, the effect of α-β-cell communication on the 1st responders subpopulation was quantified by running 6 seeds of the multicellular model for two separate conditions as described in the methods. Time of response and 1st responders were determined for both control (0 nM GLP-1) and stimulatory (20 nM GLP-1) experiments. Then, the number of 1st responders that were α-linked in both control and stimulatory conditions were calculated and compared using a Wilcoxon signed rank test. The results are shown in Figure 5.13.

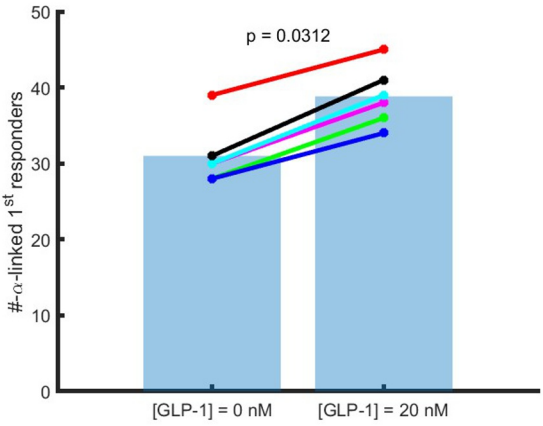

Fig. 5.13: Effect of α-β-cell communication on 1st responder subpopulation. Statistical signficance testing done using a Wilcoxon signed rank test.

From Figure 5.13, it can be seen that introducing α-β-cell communication increased the number of α-linked β-cells that were 1st responders. This trend was observed across all six seeds.

5.4 Discussion

In this manuscript, we aim to reconstruct realistic islets by studying the effect of heterogeneous parameters and some constant parameters of β-cells as well as paracrine signaling for α-β-cell communication on intrinsic and extrinsic heterogeneity. One of the ways to reach a successful reconstruction was to change the number of bursting cells to help coordinate glucose-dependent activity.

While the sensitivity analysis approach used above guided our search for the most sensitive parameters for the bursting β-cell phenotype, the parameter sensitivities for spiking cells are dominant, making it difficult to selectively modulate the bursting phenotype without concurrently influencing the spiking and silent populations. These findings highlight the complexity of phenotype regulation within the β-cell population and point to the need for more targeted multi-parameter adjustments or nonlinear sensitivity analyses to independently modulate the bursting phenotype. It also supports the contention that the crucial bursting dynamics may in fact not be a common property of single β-cells but rather, as has been argued previously [33], an emergent dynamic resulting from coupling cells with silent and spiking phenotypes.

Our comparison of β-cell phenotypes under fixed versus heterogeneous SK conductance demonstrates that variability in SK channel expression can be incorporated into computational models without disrupting established behavior. At lower con-

ductance levels (0.001 and 0.01 nS/pF), spiking and bursting were more prevalent than at the reference value of 0.1 nS/pF. In contrast, at the highest conductance (1 nS/pF), nearly all cells became silent due to excessive repolarizing drive. Under the heterogeneous condition, the resulting phenotype distribution closely resembled that of the reference group (0.1 nS/pF). This similarity indicates that the introduction of heterogeneity does not compromise the internal consistency of the model or necessitate compensatory adjustments of other parameters. Instead, it allows the model to retain its established dynamics while explicitly reflecting the biological fact that SK channel expression is heterogeneous among β-cells. In this sense, the major contribution of our approach lies not in altering the predicted outcomes relative to the reference conductance, but in updating the framework to incorporate physiologically grounded variability.

From a biological perspective, embedding heterogeneity at the channel level provides a more faithful representation of β-cell networks, where functional diversity among cells is an experimentally observed hallmark. From a modeling perspective, this approach increases the fidelity of simulations by aligning them more closely with the molecular data, thereby providing a stronger foundation for studying both normal physiology and disease-related dysfunction. In particular, because β-cell heterogeneity is disrupted in type 2 diabetes, models that integrate transcriptomic variability may offer valuable tools for probing how such changes contribute to impaired islet function.

Introduction of α-β-cell communication via GLP-1 acting on the GLP-1R to decrease the K_{ATP} channel conductance resulted in a statistically significant increase in α-linked β-cells being defined as 1st responders. However, this role seems to be minor as indicated by the number of α-linked β-cells that were already 1st responders prior to GLP-1 stimulation. This indicates that intrinsic parameters and gap-junction coupling are likely to also play substantial roles in defining the 1st subpopulation, as shown in previous work [29].

It is also important to address some limitations of this implementation of α-β-cell communication. The first being that only one effect of GLP-1R signaling was modeled. As detailed in this review [34], the effects of increased cyclic-AMP production on β-cells function are various. Thus, future models must work to incorporate these effects to get a true understanding of how paracrine signaling between α and β-cells impacts β-cells function. Second, PKA_a was modeled as being an instantaneous function of cyclic-AMP. However, previous studies have indicated that PKA_a shows a distinct relationship to cyclic-AMP oscillations [35]. Third, the strength and distance of paracrine signaling within the islet is not known. In this model, only β-cells that were in contact with α-cells were considered to be close enough for paracrine interactions. However, in real islets this may not be the case. Furthermore, the actual extracellular concentration of GLP-1 or glucagon that an α-linked β-cell might be exposed to is unknown, but, for simplicity, was set to a concentration that produces maximal stimulation. Fourth, calculating the time of response with the given population of β-cells proved to be difficult owing to the spiking nature of their first phase. A simple method of the time point at which the $[Ca^{2+}]$ reached 25 % of its maximum value relative to the steady state $[Ca^{2+}]$ at 2 mM glucose was used. A separate

method that utilized MATLABs findpeaks() function was also employed, and gave a similar, statistically significant result. Manual inspection of the time points chosen for both methods indicated them to be reasonable, but not perfect. Thus, a more rigorous method should be employed in future work to confirm the results.

References

1. Over Cabrera, Dora M. Berman, Norma S. Kenyon, Camillo Ricordi, Per-Olof Berggren, and Alejandro Caicedo. The unique cytoarchitecture of human pancreatic islets has implications for islet cell function. Proceedings of the National Academy of Sciences, 103(7):2334–2339, 2006.
2. Danh-Tai Hoang, Hitomi Matsunari, Masaki Nagaya, Hiroshi Nagashima, J. Michael Millis, Piotr Witkowski, Vipul Periwal, Manami Hara, and Junghyo Jo. A conserved rule for pancreatic islet organization. PLOS ONE, 9(10):1–9, 10 2014.
3. German Kilimnik, Junghyo Jo, Vipul Periwal, Mark C. Zielinski, and Manami Hara. Quantification of islet size and architecture. Islets, 4(2):167–172, 2012. PMID: 22653677.
4. Abraham Kim, Kevin Miller, Junghyo Jo, German Kilimnik, Pawel Wojcik, and Manami Hara. Islet architecture: A comparative study. Islets, 1(2):129–136, 2009. PMID: 20606719.
5. Marcela Brissova, Michael J. Fowler, Wendell E. Nicholson, Anita Chu, Boaz Hirshberg, David M. Harlan, and Alvin C. Powers. Assessment of human pancreatic islet architecture and composition by laser scanning confocal microscopy. Journal of Histochemistry & Cytochemistry, 53(9):1087–1097, 2005. PMID: 15923354.
6. Joan Camunas-Soler, Xiao-Qing Dai, Yan Hang, Austin Bautista, James Lyon, Kunimasa Suzuki, Seung K. Kim, Stephen R. Quake, and Patrick E. MacDonald. Patch-Seq Links Single-Cell Transcriptomes to Human Islet Dysfunction in Diabetes. Cell Metabolism, 31(5):1017–1031.e4, May 2020. Publisher: Elsevier.
7. T L Jetton and M A Magnuson. Heterogeneous expression of glucokinase among pancreatic beta cells. Proceedings of the National Academy of Sciences, 89(7):2619–2623, April 1992. Publisher: Proceedings of the National Academy of Sciences.
8. R. Kiekens, P. In 't Veld, T. Mahler, F. Schuit, M. Van De Winkel, and D. Pipeleers. Differences in glucose recognition by individual rat pancreatic B cells are associated with intercellular differences in glucose-induced biosynthetic activity. The Journal of Clinical Investigation, 89(1):117–125, January 1992. Publisher: The American Society for Clinical Investigation.
9. David W. Piston, Susan M. Knobel, Catherine Postic, Kathy D. Shelton, and Mark A. Magnuson. Adenovirus-mediated Knockout of a Conditional Glucokinase Gene in Isolated Pancreatic Islets Reveals an Essential Role for Proximal Metabolic Coupling Events in Glucose-stimulated Insulin Secretion *. Journal of Biological Chemistry, 274(2):1000–1004, January 1999. Publisher: Elsevier.
10. M. Van De Winkel and D. Pipeleers. Autofluorescence-activated cell sorting of pancreatic islet cells: Purification of insulin-containing B-cells according to glucose-induced changes in cellular redox state. Biochemical and Biophysical Research Communications, 114(2):835–842, July 1983.
11. D. Mears, N. F. Sheppard, I. Atwater, and E. Rojas. Magnitude and modulation of pancreatic β-cell gap junction electrical conductance in situ. J. Membarin Biol., 146(2):163–176, July 1995.
12. M. Pérez-Armendariz, C. Roy, D. C. Spray, and M. V. Bennett. Biophysical properties of gap junctions between freshly dispersed pairs of mouse pancreatic beta cells. Biophysical Journal, 59(1):76–92, January 1991.
13. Nikki L. Farnsworth, Alireza Hemmati, Marina Pozzoli, and Richard K. P. Benninger. Fluorescence recovery after photobleaching reveals regulation and distribution of connexin36 gap junction coupling within mouse islets of Langerhans. The Journal of Physiology, 592(20):4431–4446, 2014. _eprint: https://physoc.onlinelibrary.wiley.com/doi/pdf/10.1113/jphysiol.2014.276733.

14. Gerardo J. Félix-Martínez, Aurelio N. Mata, and J. Rafael Godínez-Fernández. Reconstructing human pancreatic islet architectures using computational optimization. Islets, 12(6):121–133, November 2020. Publisher: Taylor & Francis _eprint: https://doi.org/10.1080/19382014.2020.1823178.
15. Gerardo J. Félix-Martínez and J. R. Godínez-Fernández. Comparative analysis of reconstructed architectures from mice and human islets. Islets, 14(1):23–35, December 2022. Publisher: Taylor & Francis _eprint: https://doi.org/10.1080/19382014.2021.1987827.
16. JaeAnn M. Dwulet, Nurin W. F. Ludin, Robert A. Piscopio, Wolfgang E. Schleicher, Ong Moua, Matthew J. Westacott, and Richard K. P. Benninger. How Heterogeneity in Glucokinase and Gap-Junction Coupling Determines the Islet [Ca2+] Response. Biophysical Journal, 117(11):2188–2203, December 2019. Publisher: Elsevier.
17. Roshni Shetty, Radhika Singh-Agarwal, Stefan Meier, Christian Goetz, and Andrew G. Edwards. Reconstruction of a pancreatic beta cell network from heterogeneous functional measurements. In Computational Physiology: Simula Summer School 2023 - Student Reports, pages 71–86. Springer Nature Switzerland, Cham, 2024.
18. Karoline Horgmo Jæger and Aslak Tveito. Sometimes extracellular recordings fail for good reasons. bioRxiv, July 2025. ISSN: 2692-8205 Pages: 2025.07.01.662690 Section: New Results.
19. Reshma Ramracheya, Caroline Chapman, Margarita Chibalina, Haiqiang Dou, Caroline Miranda, Alejandro González, Yusuke Moritoh, Makoto Shigeto, Quan Zhang, Matthias Braun, et al. Glp-1 suppresses glucagon secretion in human pancreatic alpha-cells by inhibition of p/q-type ca2+ channels. Physiological reports, 6(17):e13852, 2018.
20. Åsa Segerstolpe, Athanasia Palasantza, Pernilla Eliasson, Eva-Marie Andersson, Anne-Christine Andréasson, Xiaoyan Sun, Simone Picelli, Alan Sabirsh, Maryam Clausen, Magnus K Bjursell, et al. Single-cell transcriptome profiling of human pancreatic islets in health and type 2 diabetes. Cell metabolism, 24(4):593–607, 2016.
21. Adam P. Chambers, Joyce E. Sorrell, April Haller, Karen Roelofs, Chelsea R. Hutch, Ki-Suk Kim, Ruth Gutierrez-Aguilar, Bailing Li, Daniel J. Drucker, David A. D'Alessio, Randy J. Seeley, and Darleen A. Sandoval. The Role of Pancreatic Preproglucagon in Glucose Homeostasis in Mice. Cell Metab, 25(4):927–934.e3, April 2017.
22. Over Cabrera, James Ficorilli, Janice Shaw, Felipe Echeverri, Frank Schwede, Oleg G. Chepurny, Colin A. Leech, and George G. Holz. Intra-islet glucagon confers β-cell glucose competence for first-phase insulin secretion and favors GLP-1R stimulation by exogenous glucagon. Journal of Biological Chemistry, 298(2):101484, February 2022.
23. Megan E. Capozzi, Berit Svendsen, Sara E. Encisco, Sophie L. Lewandowski, Mackenzie D. Martin, Haopeng Lin, Justin L. Jaffe, Reilly W. Coch, Jonathan M. Haldeman, Patrick E. MacDonald, Matthew J. Merrins, David A. D'Alessio, and Jonathan E. Campbell. β Cell tone is defined by proglucagon peptides through cAMP signaling. JCI Insight, 4(5), March 2019. Publisher: American Society for Clinical Investigation.
24. Nirmala V. Balasenthilkumaran, Lidija Križančić Bombek, David Ramirez, Maša Skelin Klemen, Eva Paradiž Leitgeb, Jasmina Kerčmar, Jan Kopecky, Yaowen Zhang, Annanya Sethiya, Adam Takaoglu, Divya Prabhu, Aining Fan, Shravani Vitalapuram, Jurij Dolenšek, Marko Gosak, Richard KP Benninger, Andraž Stožer, and Vira Kravets. Role of GLP1-receptor-mediated α-β-cell communication in functional β-cell heterogeneity. bioRxiv, 2025.
25. VIRA KRAVETS, CLAIRE H. LEVITT, and RICHARD K. BENNINGER. 195-OR: To Which Degree Do Alpha Cells Shape the Role of the Beta Cells First Responders? Diabetes, 72(Supplement_1):195–OR, June 2023.
26. Michela Riz, Matthias Braun, and Morten Gram Pedersen. Mathematical modeling of heterogeneous electrophysiological responses in human β-cells. PLOS Computational Biology, 10(1):1–14, 01 2014.
27. Daniele Andrean and Morten Gram Pedersen. Machine learning provides insight into models of heterogeneous electrical activity in human beta-cells. Mathematical Biosciences, 354:108927, 2022.

28. Chae Young Cha, Yasuhiko Nakamura, Yukiko Himeno, Jianwu Wang, Shinpei Fujimoto, Nobuya Inagaki, Yung E. Earm, and Akinori Noma. Ionic mechanisms and Ca2+ dynamics underlying the glucose response of pancreatic β cells: a simulation study. J Gen Physiol, 138(1):21–37, July 2011.
29. Vira Kravets, JaeAnn M. Dwulet, Wolfgang E. Schleicher, David J. Hodson, Anna M. Davis, Laura Pyle, Robert A. Piscopio, Maura Sticco-Ivins, and Richard K. P. Benninger. Functional architecture of pancreatic islets identifies a population of first responder cells that drive the first-phase calcium response. PLOS Biology, 20(9):e3001761, September 2022. Publisher: Public Library of Science.
30. Yukari Takeda, Akira Amano, Akinori Noma, Yasuhiko Nakamura, Shimpei Fujimoto, and Nobuya Inagaki. Systems analysis of GLP-1 receptor signaling in pancreatic β-cells. American Journal of Physiology-Cell Physiology, 301(4):C792–C803, October 2011. Publisher: American Physiological Society.
31. Leonid E. Fridlyand and Louis H. Philipson. Pancreatic Beta Cell G-Protein Coupled Receptors and Second Messenger Interactions: A Systems Biology Computational Analysis. PLOS ONE, 11(5):e0152869, May 2016. Publisher: Public Library of Science.
32. Danh-Tai Hoang, Manami Hara, and Junghyo Jo. Design Principles of Pancreatic Islets: Glucose-Dependent Coordination of Hormone Pulses. PLOS ONE, 11(4):e0152446, April 2016. Publisher: Public Library of Science.
33. P. Smolen, J. Rinzel, and A. Sherman. Why pancreatic islets burst but single beta cells do not. the heterogeneity hypothesis. Biophysical Journal, 64(6):1668–1680, 1993.
34. Andraž Stožer, Eva Paradiž Leitgeb, Viljem Pohorec, Jurij Dolenšek, Lidija Križančić Bombek, Marko Gosak, and Maša Skelin Klemen. The Role of cAMP in Beta Cell Stimulus–Secretion and Intercellular Coupling. Cells, 10(7):1658, July 2021. Publisher: Multidisciplinary Digital Publishing Institute.
35. Qiang Ni, Ambhighainath Ganesan, Nwe-Nwe Aye-Han, Xinxin Gao, Michael D. Allen, Andre Levchenko, and Jin Zhang. Signaling diversity of PKA achieved via a Ca2+-cAMP-PKA oscillatory circuit. Nat Chem Biol, 7(1):34–40, January 2011. Publisher: Nature Publishing Group.

Chapter 6
Effects of cellular and subcellular geometry on store-operated calcium entry in dendritic spines

Daniel Mansour, Marina Vannucci, Lucie Wintrová, and Emmet Francis

Abstract Store-operated calcium entry (SOCE) has been recently identified as a mechanism that triggers additional calcium entry into the cell, across the plasma membrane (PM), in response to depletion from the endoplasmic reticulum (ER). In neurons, SOCE is a crucial process for refilling calcium stores. However, the role of ER geometry in facilitating SOCE within dendritic spines has not been fully elucidated. In this paper, we build upon previous work on calcium dynamics to evaluate the effect of ER geometry on SOCE. Here, we develop a basic model of SOCE and construct idealized ER geometries which include simple representations of ER-PM junctions. We first describe the time evolution dynamics of membrane-bound calcium channel activation to show that an increased density of ER-PM junctions leads to greater IP_3R and Orai1 channel activation. Next, we investigate how Ca^{2+} concentration varied over time in various idealized geometries and find that smaller ER-PM gaps and increased ER-PM junction density result in less ER Ca^{2+} efflux and more cytosolic Ca^{2+} influx. Finally, we investigate how Ca^{2+} concentration varied over time in a realistic dendrite geometry and find that supressing SOCE leads to reduced ER Ca^{2+} reuptake. Thus, ER geometry plays a crucial role in facilitating SOCE in dendritic spines.

Daniel Mansour
Department of Mechanical and Aerospace Engineering, University of California San Diego, USA

Marina Vannucci
Department of Physiology, University of Bern, Switzerland

Lucie Wintrová
Mathematical Institute of Charles University, Czech Republic

Emmet Francis (corresponding author)
Department of Pharmacology, University of California San Diego, USA e-mail: eafrancis@ucsd.edu

K. J. McCabe, *Computational Physiology*, Simula SpringerBriefs on Computing 20, https://doi.org/10.1007/978-3-032-28826-4_6

6.1 Introduction

Calcium is a second messenger that plays an important role in eliciting cell responses to stimuli throughout the body [1]. Intracellular calcium regulation is fundamental in physiological processes such as skeletal muscle contraction [2], platelet activation and mobilization [3], T-cell activation, [4] and synaptic transmission in neurons [5] [6] [7]. In the cytoplasm, calcium concentration is typically maintained at very low levels, ~100 nM, while the extracellular levels are on average 4 orders of magnitude higher, ~1 mM [1]. This significant concentration gradient across the plasma membrane (PM) makes passive transport of calcium from the extracellular space to the cytosol a rapid process. Calcium concentration in the cytosol can increase drastically by two different mechanisms: calcium entry through the PM through gated transport or facilitated diffusion and calcium release from the endoplasmic reticulum (ER). A combination of ATP-dependent pumps exist both on the PM and ER-membrane that can transport calcium either to the extracellular space or to the ER lumen. The main ones are the plasma membrane calcium ATPase (PMCA) and the sarco/endoplasmic reticulum ATPase (SERCA) [8]. Due to this constant calcium efflux through PMCA, without an additional influx of calcium from the extracellular space the ER calcium concentration would deplete over extended periods of activation. Store-operated calcium entry (SOCE) has been recently identified as a mechanism that triggers additional calcium entry to avoid ER depletion. This phenomenon has been recently shown experimentally in excitable [9] [10] [11] and non-excitable tissue [12] [4].

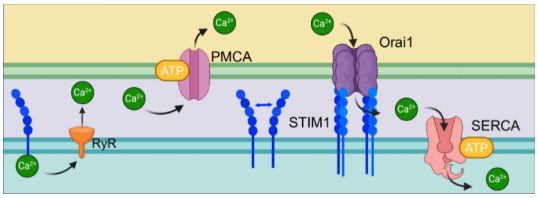

Fig. 6.1: Reactions relevant in previous models of calcium dynamics and reactions across the PM and ER membrane. Adapted from Fig. 1 in [2].

The necessary additional calcium (Ca^{2+}) influx occurs through store-operated calcium entry (SOCE). This is the process by which the depletion of calcium in the ER triggers an influx of calcium through the PM, effectively coupling the two pathways for calcium store refilling [7] [2] [3]. A representation of the main actors participating in SOCE is shown in Figure 6.1. Once ER calcium channels such as the RyR or inositol 1,4,5-trisphosphate (IP_3) receptor open, Ca^{2+} flows along its electrochemical gradient into the cytosol. This causes a rapid depletion of ER calcium, which initiates SOCE. Stromal interaction molecule 1 (STIM1) located in the ER membrane acts as a sensor for calcium concentration within the ER. When Ca^{2+} concentration in the ER is high, the ER luminal tail of STIM1 is bound to calcium. However, as the concentration decreases, the complex unbinds

leading to the oligomerization of STIM1 and a change in its conformation. In its oligomerized conformation, STIM1 extends towards the PM, dramatically increasing the probability of STIM1-Orai1 binding. The calcium selective ion channel Orai1 is distributed on the PM and opens following STIM1 binding, allowing an influx of calcium to the cytosol from the extracellular space. Once the Ca^{2+} concentration is high enough the SERCA pumps activate and push calcium out of the cytosol back into the ER [4] [7] [13]. Store-operated calcium channels are expressed in various regions of the nervous system [8] [9]. Given the relevance of calcium as a second messenger in neuronal transmission, SOCE could play a relevant role in synaptic transmission, neuronal excitability, plasticity and dendritic spine formation. Dendritic spines, are bulbous protrusions from the dendritic shaft that take a variety of shapes that receive and integrate input from surrounding neurons via intracellular signaling events [8] [6]. More specifically, dendritic spines are the first point of entry for signals from surrounding axons into the neuron; at these locations the role of SOCE remain unclear. Furthermore, mutations in ER proteins in dendrites are associated with various neuropathologies, including cognitive dysfunction, familial Alzheimer's, and epilepsy, which often manifest as changes to the structure of the ER [6].

Recently, Benedetti et al. accurately resolved ER structures in dendrites using a combination of multi-color super-resolution microscopy and focused ion beam scanning electron microscopy (FIB-SEM) [6]. Researchers were able to identify a series of junctions between the PM and ER membrane periodically distributed along the membrane. ER-PM junctions are protrusions in the ER membrane that extend towards the PM, effectively reducing the ER-PM gap. Calcium channels concentrate at these locations during synaptic activation and support the rapid influx of calcium. Other studies [14] [15] have also concluded that ER geometry has a relevant role in SOCE within dendritic spines; however, difficulties related to experimental observation of this phenomenon have hindered the understanding of this relationship. Additionally, most models of calcium signaling in dendrites do not include SOCE. The ER is a highly dynamic organelle [16] with narrow tubules of significant length [17] [18], making electro-microscopic analysis of the ER all the more complex, both from a structural and functional point of view. In this regard, computational studies have been an important step forward, especially when combined with advances in super-resolution microscopy, allowing researchers to simulate complex physiological processes on realistic geometries [19] [2] [20].

Spatial Modeling Algorithms for Reactions and Transport in biological cells (SMART) is an open-source software package that offers new opportunities to implement spatial models of cell signaling [19]. SMART uses the FEniCS [21] finite element library and provides the user with the possibility of including several spatial domains (intracellular volumes and membranes) and various molecules within models of subcellular signaling. Moreover, by utilizing meshes derived from electron micrograph images and conditioned using software such as Blender and the Geometry-preserving Adaptive MeshER (GAMer2) library [20], SMART extends the simulation to realistic cellular geometries. In this paper, we build upon the work by Francis et al. [19] on calcium dynamics to evaluate the effect of ER geometry

on SOCE. As a first step we expanded on the initial model to include store-operated calcium channels. Secondly, we included periodically distributed ER-PM junctions, measured by Benedetti et al. [6], to assess the effect of complex geometries on SOCE. Finally, we examined the predictions of our model in a realistic dendritic spine geometry from Hayworth et al. [22].

6.2 Methods

6.2.1 Geometry

We first assessed the effects of ER-PM junctions in idealized geometries, shown in Figure 6.2a. These meshes were created in Gmsh [23] and subsequently imported into the simulation code. The two volumes, cytosol and ER lumen, were represented by rectangular prisms, where the size and location of the ER were scaled to more accurately match the physiological scenario. First, we created a set of geometries where the ER-PM gap varied from within the values of 0.05 μm and 0.20 μm, with an interval of 0.05 μm. Following this first control scenario, we implemented the ER-PM junctions as cylindrical protrusions on the ER upper surface, creating 3 new sets of geometries with small (0.05 μm), intermediate (0.10 μm), and tall junctions (0.15 μm). Within each of these sets, we considered different symmetric grids of protrusions (1, 9, 16, or 25). An example of this geometry is shown in Figure 6.2a. Finally, we created a homogeneous mesh throughout both volumes.

Figure 6.2b shows the realistic mesh that we used as a validation for our idealized results. The mesh was obtained from segmentation of volume electron microscopy images of neuronal dendrites and was conditioned in GAMer2 [20]. The mesh represents a single dendritic spine head containing a section of the spine apparatus in red.

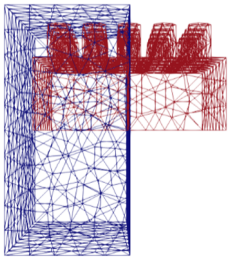

(a) Simplified mesh geometry including a cutaway of the cytosol (blue) and ER with cylindrical ER-PM junctions (red)

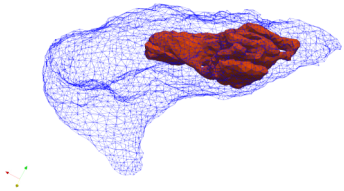

(b) Single dendritic spine head containing a section of the spine apparatus

Fig. 6.2: Representative meshes used in simulations where the cytosol mesh is shown in blue and the ER mesh is shown in red.

6.2.2 Mathematical Modeling

As described in the previous section, we divide our geometry into four domains. The cytosol (Ω^{Cyto}) and ER (Ω^{ER}) are modeled as volumes, while the PM (Γ^{PM}) and ER membrane (Ω^{ERm}) are represented as surfaces embedded in 3D space. In our simplified geometry, PM corresponds only to the top face of the box containing the cytosol, while the rest of the boundary is assigned a no-flux boundary condition. We can interpret this as considering only a segment of a neuron. A schematic representation of the reactions represented in the model can be seen in Figure 6.3.

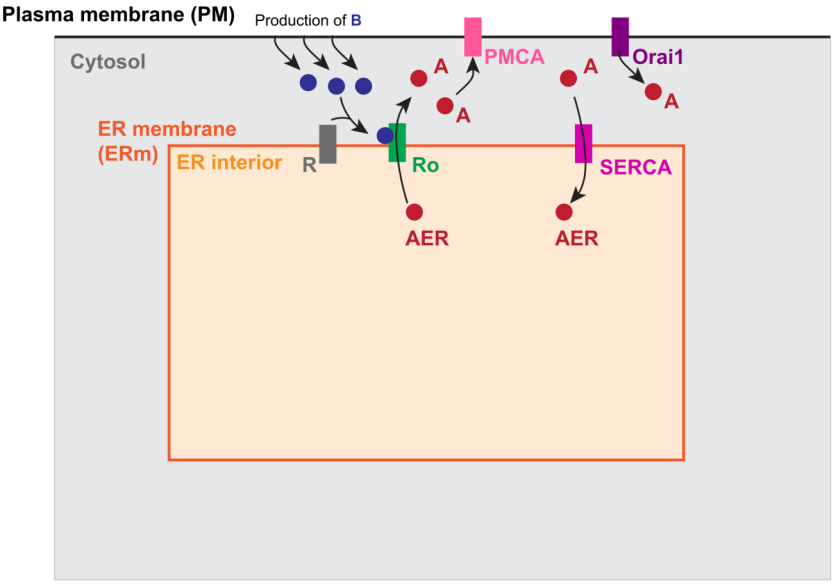

Fig. 6.3: Diagram of reactions simulated in the simple SOCE model.

We track the concentrations of six species: A, B, A_{ER}, Orai1, R, and R_o, which are distributed across the domains as follows:

$$
\begin{aligned}
A, B &\text{ in } \Omega^{Cyto},\\
A_{ER} &\text{ in } \Omega^{ER},\\
\text{Orai1} &\text{ on } \Gamma^{PM},\\
R_o, R &\text{ on } \Gamma^{ERm}.
\end{aligned}
$$

A version of this model without Orai1 was originally developed as a toy model for use in the SMART documentation [24] as a minimal model that recapitulates some basic

features of Ca^{2+} signaling networks. In this treatment, the quantity A (resp. A_{ER}) represents Ca^{2+} ions in the cytosol (resp. ER). B and R play similar role to IP_3 and the IP_3R, and will hereafter be referred to as such. Orai1 denotes the open store-operated calcium channels on the PM, which allow the influx of calcium from the extracellular space. Lastly, R (resp. R_o) represents IP_3R in its closed (resp. open) state, which mediates calcium release from the ER. We use $u_{species}$ to denote concentrations of volume species and $v_{species}$ to denote surface densities of membrane-associated species.

Building on the original model [24], we describe the evolution of each species, and then present the corresponding differential equations that formalize these dynamics. In the following, we will use $\mathbf{n}$ and $\boldsymbol{\nu}$ to denote outer normals of Ω^{Cyto} and Ω^{ER} respectively. Within the cytosol, the species B diffuses with diffusion coefficient D_B and is degraded at the rate k_{2f}. At the PM, we prescribe an influx of B given by an impulse

$$j_1[t] = \frac{mV_{max}}{1 + m^2(t - t_0)^2}, \tag{6.1}$$

where V_{max} sets the maximal scale of the signal, t_0 is the onset time and m controls the steepness of the impulse spike. On the ER membrane, B is consumed when binding to the closed receptor (with the rate k_{3f}) and released when unbinding from an open receptor (with the rate k_{3r}). The following equations mathematically capture these processes:

$$\begin{aligned} \partial_t u_B - D_B \nabla^2 u_B + k_{2f} u_B &= 0 && \text{in } \Omega^{Cyto}, \\ D_B \nabla u_B \cdot \mathbf{n} - j_1[t] &= 0 && \text{on } \Gamma^{PM}, \\ D_B \nabla u_B \cdot \mathbf{n} + k_{3f} v_R u_B - k_{3r} v_{Ro} &= 0 && \text{on } \Gamma^{ERm}. \end{aligned} \tag{6.2}$$

We now describe the dynamics of the cytosolic calcium concentration. Inside the cytosol, A diffuses with diffusion coefficient D_A, but does not undergo any degradation (this is a simplifying assumption). Its concentration changes are governed by fluxes across the PM and the ER membrane. At the plasma membrane, A is extruded from the cytosol by PMCA at a rate modeled by a first-order Hill equation, and replenished by SOCE with the flux proportional to the fraction of open channels Orai1 and flux rate j_0. In the ER membrane, calcium is released from the ER through open channels R_o driven by the calcium gradient between the ER and the cytosol with a maximal rate $k_{4,Vmax}$, and actively transported back into the ER by SERCA pumps, modeled as a second-order Hill equation. We can thus write:

$$\begin{aligned} \partial_t u_A - D_A \nabla^2 u_A &= 0 && \text{in } \Omega^{Cyto}, \\ D_A \nabla u_A \cdot \mathbf{n} - \frac{k_{6f} u_A}{u_A + k_{6m}} + v_{Orai1} j_0 &= 0 && \text{on } \Gamma^{PM}, \\ D_A \nabla u_A \cdot \mathbf{n} - k_{4,Vmax} v_{Ro} (u_{AER} - u_A) + \frac{k_{5f} u_A^2}{u_A^2 + k_{5m}^2} &= 0 && \text{on } \Gamma^{ERm}. \end{aligned} \tag{6.3}$$

Within the ER, calcium diffuses with rate D_{AER}. On the ER membrane, calcium leaves the ER through R_o channels with a maximal rate $k_{4,Vmax}$, and it is replenished by SERCA pumps that actively transport cytosolic calcium.

$$\partial_t u_{AER} - D_{AER}\nabla^2 u_{AER} = 0 \qquad \text{in } \Omega^{ER}, \quad (6.4)$$

$$D_{AER}\nabla u_{AER}\cdot \boldsymbol{\nu} + k_{4,Vmax} v_{Ro}(u_{AER} - u_A) - \frac{k_{5f}u_A^2}{u_A^2 + k_{5m}^2} = 0 \qquad \text{on } \Gamma^{ERm}.$$

We next describe the dynamics of open Orai1 channels at the plasma membrane, which mediate SOCE. The open channel concentration relaxes towards its steady-state value ρP_{inf}, where ρ denotes the total density of channels and

$$P_{inf} = \frac{1 - \tanh(s\cdot(d - d_0))}{1 + \tanh(s\cdot d_0)} \cdot \frac{1}{1 + \left(\frac{c}{c_0}\right)^4} \quad (6.5)$$

denotes the steady-state channel open probability. The constitutive relation for P_{inf} combines two regulatory effects. The first factor models the dependence on the distance to the closest point on the ERm (d), where d_0 denotes the critical distance above which the channel cannot open, and s controls the steepness of the open-close transition. The second part accounts for calcium-dependent Hill-type inhibition where the concentration c is measured at the closest point of the ER. The Hill coefficient comes from previous experimental measurements [4], and has been used in previous studies [7]. The time evolution of the open-channel density is then governed by the following equation:

$$\partial_t v_{Orai1} - \frac{\rho P_{inf} - v_{Orai1}}{\tau} = 0 \qquad \text{on } \Gamma^{PM}. \quad (6.6)$$

Finally, we describe the dynamics of the ER membrane receptors, R and R_o. The unbound (closed) receptor, R, can bind B at rate k_{3r}, converting into the open receptor state R_o, while R_o can unbind at rate k_{3r} to return to the closed state R. Both receptor states can also diffuse along the ER membrane, with rates D_R and D_{Ro}, respectively:

$$\partial_t v_R - D_R\nabla^2 v_R - k_{3f} v_R u_B + k_{3r} v_{Ro} = 0 \qquad \text{on } \Gamma^{ERm}, \quad (6.7)$$

$$\partial_t v_{Ro} - D_{Ro}\nabla^2 v_{Ro} + k_{3f} v_R u_B - k_{3r} v_{Ro} = 0 \qquad \text{on } \Gamma^{ERm}. \quad (6.8)$$

In Table 6.1, we provide the units and the values for each parameter consistent with our code. This overview allows comparison with experimentally measured or previously reported values in similar neuronal calcium signaling models (see, e.g., Supplemental Tables S4 and S5 in [2] to compare the magnitude of the SOCE flux).

Table 6.1: Model parameters with units and values used in the code

Parameter	Units	Value in Code
D_A	μm^2/s	1.0
D_{AER}	μm^2/s	5.0
D_B	μm^2/s	1.0
D_R	μm^2/s	0.02
D_{Ro}	μm^2/s	0.02
k_{2f}	1/s	10.0
k_{3r}	1/s	100.0
k_{3f}	1/(μM·s)	100.0
$k_{4,Vmax}$	1/(μM·s)	2000.0
k_{5f}	molecule/(μm^2· s)	18000.0
k_{5m}	μM	0.27
k_{6f}	molecule/(μm^2· s)	1000.0
k_{6m}	μM s	0.1
V_{max}	molecule/(μ m^2·s)	500.0
t_0	s	0.1
m	-	200.0
j_0	1/s	10^4
ρ	molecule/μm^2	1.0
τ	s	1.0
s	1/ μm	200.0
d_0	μm	0.1
c_0	μM	100.0

6.3 Results

6.3.1 Channel Behavior

We first investigated how the level of channel activation of IP_3R and Orai1 varied with different mesh geometries. Both IP_3R and Orai1 facilitate the entry of Ca^{2+} into the cytosol. We began our simulations with an impulse of IP_3 from the PM, which diffuses across the cytosol to the ER membrane where it can bind to and activate IP_3R channels. We observed that a greater number of IP_3R channels opened when there was a higher density of ER-PM junctions (Fig. 6.4). Since the IP_3R channels are ligand-activated, the higher number of ER-PM junctions increases the probability of channel activation due to their close proximity to the PM where IP_3 is released. Similarly, Orai1 activation was also greater in conditions with a higher density of ER-PM junctions (Fig. 6.4). Orai1 activation is dependent on the distance between the ER and PM as an implicit model of STIM1 molecules binding to Orai1 to form an ER-PM junction (Eq. 6.5). The presence of a greater number of ER-PM junctions in the mesh also increases the total surface area of high probability Orai1 activation, resulting in an overall higher level of Orai1 activation. Additionally, refilling of ER Ca^{2+} due to SERCA activation results in an eventual decline in Orai1 activity (Fig. 6.5).

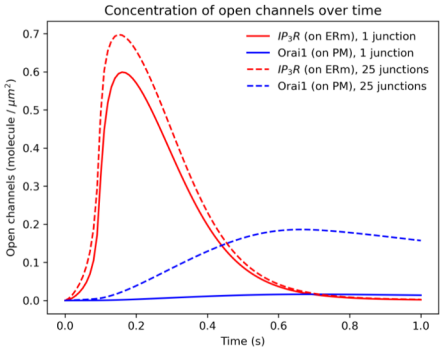

Fig. 6.4: Evolution of IP_3R and Orai1 channel activation over time for simulation conditions with 1 and 25 ER-PM junctions.

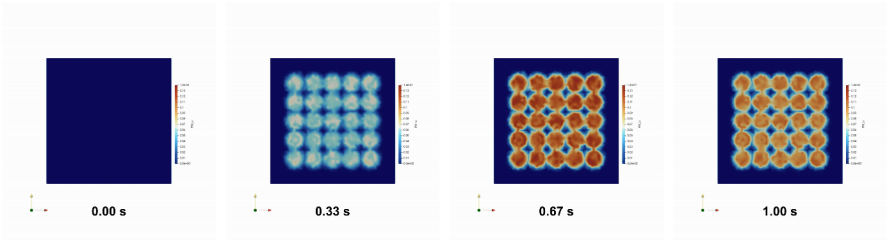

Fig. 6.5: Representative snapshots of Orai1 channel activation for the 25 ER-PM junction condition at 0.00 s, 0.33 s, 0.67 s, and 1.00 s.

6.3.2 Calcium Dynamics

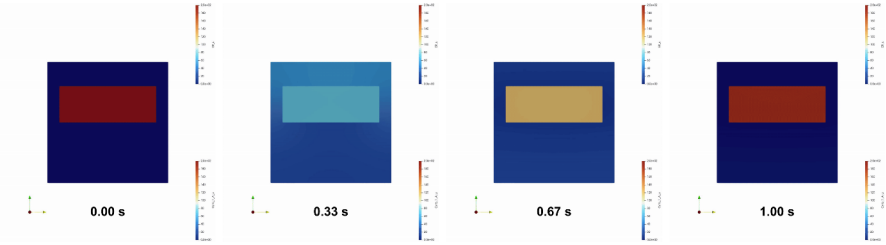

(a) Ca^{2+} concentration for a simulation condition without ER-PM junctions (ER-PM gap of 0.20 µm).

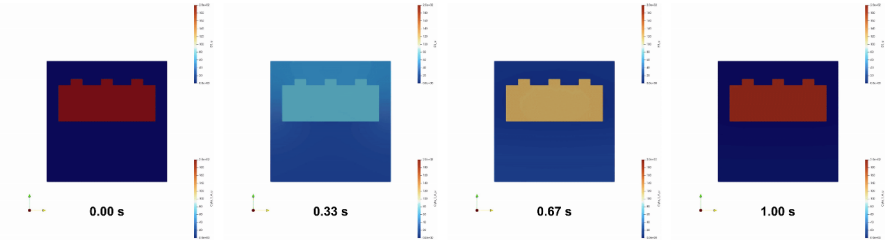

(b) Ca^{2+} concentration for a simulation condition with 9 short ER-PM junctions (height of 0.05 µm).

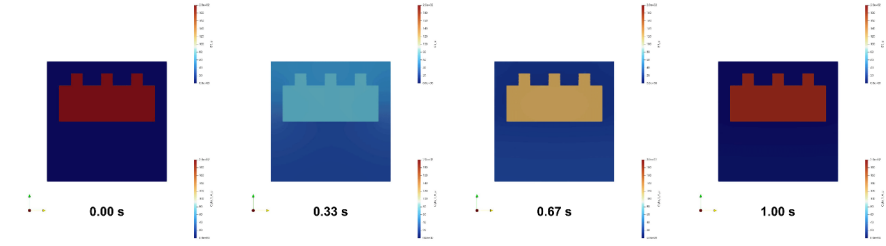

(c) Ca^{2+} concentration for a simulation condition with 9 medium-sized ER-PM junctions (height of 0.10 µm).

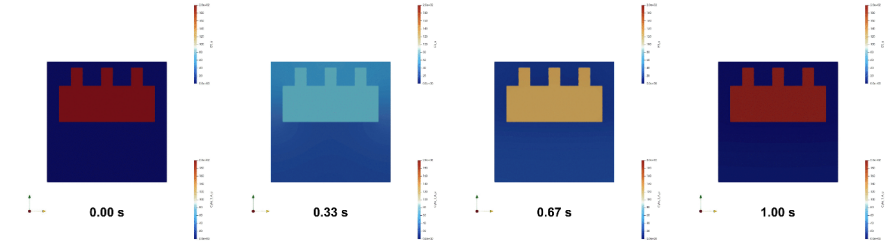

(d) Ca^{2+} concentration for a simulation condition with 9 tall ER-PM junctions (height of 0.15 µm).

Fig. 6.6: Representative snapshots of Ca^{2+} concentration for the various simulated conditions at 0.00 s, 0.33 s, 0.67 s, and 1.00 s.

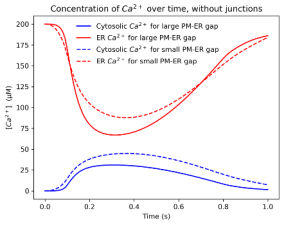

(a) Ca^{2+} concentration for simulation conditions without ER-PM junctions with large (0.20 μm) and small (0.05 μm) ER-PM gaps.

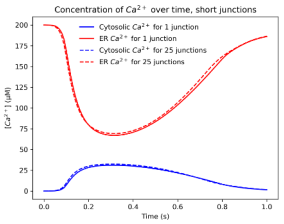

(b) Ca^{2+} concentration for simulation conditions with 1 and 25 short ER-PM junctions (height of 0.05 μm).

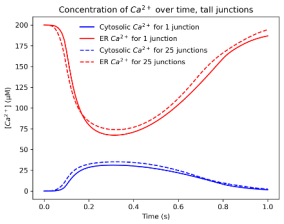

(c) Ca^{2+} concentration for simulation conditions with 1 and 25 tall ER-PM junctions (height of 0.15 μm).

Fig. 6.7: Evolution of cytosolic and ER calcium concentration over time on different idealized geometries.

As the primary ion of interest in SOCE, we next investigated how Ca^{2+} concentration varied over time in the cytosol and the ER. To establish a baseline, we first simulated SOCE with geometries that lack specific ER-PM junctions, instead providing a planar ER surface to interface with the PM with a set ER-PM gap (Fig. 6.6a). In each condition, we observed an initial release of Ca^{2+} from the ER accompanied by an influx of Ca^{2+} into the cytosol, followed by a gradual efflux of Ca^{2+} from the cytosol and reuptake of Ca^{2+} into the ER to restore initial conditions (Fig. 6.7a). When the ER-PM gap was large (0.20 μm), ER Ca^{2+} concentration decreased much more (by up to about 25 μM) than with a small ER-PM gap (0.05 μm). Despite the difference in ER Ca^{2+} release, cytosolic Ca^{2+} concentration increased more for the small ER-PM gap condition. A smaller ER-PM gap allows for faster activation of IP_3R channels, hence the quicker initial release of Ca^{2+} from the ER. However, a smaller ER-PM gap also supports greater Orai1 channel activation, leading to increased Ca^{2+} influx. Elevated Orai1 channel activity increases cytosolic Ca^{2+} concentration. Since SERCA pump activity is dependent on cytosolic Ca^{2+} concentration, elevated Orai1 channel activity also leads to elevated SERCA pump activity. Overall, ER Ca^{2+} stores are consistently being refilled due to Ca^{2+} influx through Orai1 channels and then SERCA pumps, thus supporting sustained ER Ca^{2+} release. Upon the addition of simple junctions to the idealized cell geometry, we observed similar trends for both short junctions (Fig. 6.6b), medium-sized (Fig. 6.6c), and tall junctions (Fig. 6.6d). For conditions with a single junction, the time series profiles of Ca^{2+} concentration closely resembled those for the large ER-PM gap conditions without junctions (Fig. 6.7). As the number, and thus density, of junctions increased, the time series profile of Ca^{2+} concentration trended toward those for the small ER-PM gap conditions without junctions, although the difference between 1 and 25 junctions was relatively small. As the density of junctions increases, the surface area of ER membrane near the PM also increases. This increased surface area supports greater Orai1 activation and thus extracellular Ca^{2+} entry to the cytosol to support reuptake of Ca^{2+} into the ER.

6.3.3 Realistic Geometry

Finally, we investigated how Ca^{2+} concentration varied over time when using a realistic dendritic spine geometry. We used this realistic mesh to evaluate how well the idealized geometries captured changes in Ca^{2+} concentration using a very simple implementation of SOCE. Compared with the idealized geometries, the realistic geometry followed a similar overall profile of ER and cytosolic Ca^{2+} concentration over time, although more Ca^{2+} left the ER and less Ca^{2+} entered the cytosol (Fig. 6.8). Additionally, calcium concentration had more spatial variation throughout the cytosol in the realistic dendrite geometry (Fig. 6.9). The difference in magnitudes of Ca^{2+} concentration between the real and ideal geometries could be due to differences in the surface area to volume ratio of the ER. Other potential explanations could be smaller distances between the ER membrane and PM or differences in overall simulated volume. We then decided to investigate how the length of the ER-PM gap could change Ca^{2+} release and SOCE. However, instead of altering the ER-PM gap in the realistic dendrite as we did in the idealized geometry, we altered the reference distance (d_0) used for the simulated Orai1 opening probability in the SOCE reaction. By decreasing the reference distance from 0.1 µm to 0.05 µm, we observed a small decrease in the Ca^{2+} concentration over time in both the cytosol and the ER (Fig. 6.8), consistent with our previous observations. Decreasing the reference distance has the effect of reducing SOCE activation over the entire geometry; therefore, this indicates that the ER was unable to refill its Ca^{2+} stores effectively without robust activation of SOCE.

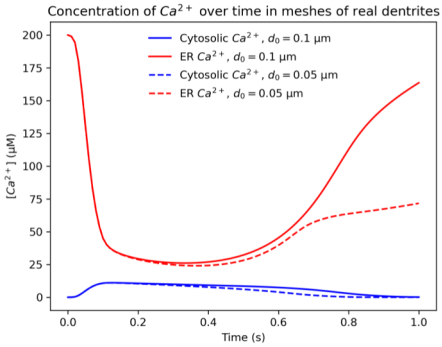

Fig. 6.8: Evolution of cytosolic and ER calcium concentration over time in a realistic geometry for simulation conditions with reference distances of 0.1 µm and 0.05 µm.

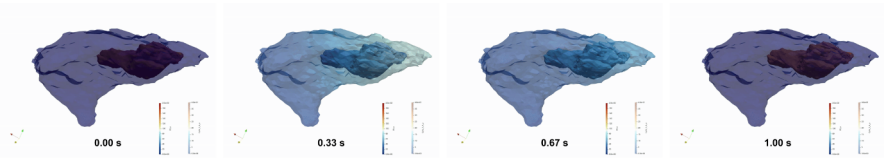

Fig. 6.9: Representative snapshots of Ca^{2+} concentration for the realistic dendrite geometry at 0.00 s, 0.33 s, 0.67 s, and 1.00 s.

6.4 Conclusion

Our results demonstrate that ER geometry, particularly the presence and density of ER-PM junctions, plays a critical role in the dynamics of store-operated calcium entry (SOCE). Using both idealized and realistic geometries, we show that increased ER-PM junction density enhances IP_3R and Orai1 activation, supporting greater calcium influx into the cytosol and rapid refilling of ER calcium stores. Notably, small ER-PM gaps and greater membrane contact area facilitate localized calcium signaling and sustain SOCE, highlighting the importance of spatial organization in cellular signaling networks. Moreover, the calcium concentration is highly dependent on SOCE parameters such as reference distance.

Our minimal model recapitulates key features of SOCE and channel behavior, accurately capturing spatially localized activation and time-dependent calcium concentration changes. Furthermore, in realistic dendritic spine geometries, we observe that tuning parameters such as the Orai1 activation distance can significantly impact calcium homeostasis, potentially suppressing SOCE and limiting ER calcium recovery. In terms of computational time and accuracy, it would be possible and interesting to improve the idealized geometry mesh. The current mesh has the same element size throughout the mesh, but adaptively refining the mesh near regions of interest such as the ER-PM junctions would improve computational time and accuracy of the results. Additionally, introducing SOCE within a more realistic and complete model of calcium signaling would provide validation of our predictions.

6.5 Acknowledgments

We would like to thank Hanieh Falahati for providing the data for the realistic dendrite geometry, Shravya Bharathwaj and Nikhil Srinivasan for constructing the mesh for the realistic dendrite geometry, and the Rangamani Lab at UCSD for giving us access to computational resources for this project.

References

1. M. Endo. Calcium ion as a second messenger with special reference to excitation-contraction coupling. Journal of Pharmacological Sciences, 100(5):519–524, 2006. Epub 2006 May 13.
2. Emmet A. Francis, Juliette Hamid, Anusha Kumar, and Padmini Rangamani. Systems modeling reveals that store-operated calcium entry modulates force and fatigue during exercise. bioRxiv, 2025.
3. Andrew T. Dolan and Scott L. Diamond. Systems modeling of Ca2+ homeostasis and mobilization in platelets mediated by IP3 and store-operated Ca2+ entry. Biophysical Journal, 106(9):2049–2060, May 2014.
4. Riina M. Luik, Bin Wang, Murali Prakriya, Minnie M. Wu, and Richard S. Lewis. Oligomerization of STIM1 couples ER calcium depletion to CRAC channel activation. Nature, 454(7203):538–542, 2008.
5. Kanishka Basnayake, David Mazaud, Lilia Kushnireva, Alexis Bemelmans, Nathalie Rouach, Eduard Korkotian, and David Holcman. Nanoscale molecular architecture controls calcium diffusion and er replenishment in dendritic spines. Science Advances, 7(38), September 2021.
6. Lorena Benedetti, Ruolin Fan, Aubrey V. Weigel, Andrew S. Moore, Patrick R. Houlihan, Mark Kittisopikul, Grace Park, Alyson Petruncio, Philip M. Hubbard, Song Pang, C. Shan Xu, Harald F. Hess, Stephan Saalfeld, Vidhya Rangaraju, David E. Clapham, Pietro De Camilli, Timothy A. Ryan, and Jennifer Lippincott-Schwartz. Periodic ER-plasma membrane junctions support long-range Ca2+ signal integration in dendrites. Cell, 188(2):484–500.e22, January 2025. Epub 2024 Dec 20.
7. E.È. Saftenku. Simulation of store-operated calcium entry in neurons. Neurophysiology, 54(1):14–24, 2022.
8. M. J. Higley and B. L. Sabatini. Calcium signaling in dendritic spines. Cold Spring Harbor Perspectives in Biology, 4(4):a005686, April 2012.
9. Jana Hartmann, Rosa M. Karl, Ryan P. D. Alexander, Helmuth Adelsberger, Monika S. Brill, Charlotta Rühlmann, Anna Ansel, Kenji Sakimura, Yoshihiro Baba, Tomohiro Kurosaki, Thomas Misgeld, and Arthur Konnerth. STIM1 Controls Neuronal Ca^{2+} Signaling, mGluR1-Dependent Synaptic Transmission, and Cerebellar Motor Behavior. Neuron, 82(3):635–644, 2014.
10. Jasmin Lalonde and et al. Store-operated calcium entry promotes the degradation of the transcription factor Sp4 in resting neurons. Science Signaling, 7:ra51, 2014.
11. Samira Samtleben, Britta Wachter, and Robert Blum. Store-operated calcium entry compensates fast ER calcium loss in resting hippocampal neurons. Cell Calcium, 58(2):147–159, 2015.
12. Jen Liou, Marc Fivaz, Takanari Inoue, and Tobias Meyer. Live-cell imaging reveals sequential oligomerization and local plasma membrane targeting of stromal interaction molecule 1 after Ca2+ store depletion. PNAS, 104(22):9301–9306, 2007.
13. P. J. Hoover and R. S. Lewis. Stoichiometric requirements for trapping and gating of Ca2+ release-activated Ca2+ (CRAC)channels by stromal interaction molecule 1 (STIM1). Proceedings of the National Academy of Sciences of the United States of America, 108(32):13299–13304, 2011.
14. M. Matsuzaki, G. Ellis-Davies, T. Nemoto, et al. Dendritic spine geometry is critical for AMPA receptor expression in hippocampal CA1 pyramidal neurons. Nature Neuroscience, 4:1086–1092, 2001.
15. Kanishka Basnayake, David Mazaud, et al. Nanoscale molecular architecture controls calcium diffusion and ER replenishment in dendritic spines. Science Advances, 7(38):eabh1376, 2021.
16. Jonathon Nixon-Abell et al. Increased spatiotemporal resolution reveals highly dynamic dense tubular matrices in the peripheral ER. Science, 354:aaf3928, 2016.
17. Mark Terasaki. Axonal endoplasmic reticulum is very narrow. Journal of Cell Science, 131(4):jcs210450, 2018.
18. Patrick C. Hoffmann, Stefano L. Giandomenico, Iva Ganeva, Michael R. Wozny, Magdalena Sutcliffe, Madeline A. Lancaster, and Wanda Kukulski. Electron cryo-tomography reveals the subcellular architecture of growing axons in human brain organoids. eLife, 10:e70269, 2021.

19. Emmet A. Francis, Justin G. Laughlin, Jørgen S. Dokken, Henrik N. T. Finsberg, Christopher T. Lee, Marie E. Rognes, and Padmini Rangamani. Spatial modeling algorithms for reactions and transport in biological cells. Nature Computational Science, 5(1):76–89, 2025.
20. Christopher T. Lee, Justin G. Laughlin, Nils Angliviel de La Beaumelle, Rommie E. Amaro, J. Andrew McCammon, Ravi Ramamoorthi, Michael Holst, and Padmini Rangamani. 3D mesh processing using GAMer 2 to enable reaction-diffusion simulations in realistic cellular geometries. PLOS Computational Biology, April 2020.
21. Martin Alnæs, Jan Blechta, Johan Hake, August Johansson, Benjamin Kehlet, Anders Logg, Chris Richardson, Johannes Ring, Marie E. Rognes, and Garth N. Wells. The FEniCS project version 1.5. Archive of Numerical Software, 3(100):1–23, 2015.
22. Kenneth Hayworth, Chun-Chung Xu, Zhiyuan Lu, Graham Knott, Richard Fetter, Juan Carlos Tapia, Jeff W Lichtman, and Harald Hess. Ultrastructurally smooth thick partitioning and volume stitching for large-scale connectomics. Nature Methods, 12(4):319–322, 2015.
23. Christophe Geuzaine and Jean-François Remacle. Gmsh: A 3-D finite element mesh generator with built-in pre- and post-processing facilities. International Journal for Numerical Methods in Engineering, 79(11):1309–1331, 2009.
24. Justin Laughlin, Emmet A. Francis, Henrik Finsberg, Jørgen Schartum Dokken, Yuan Gao, Marie E. Rognes, Christopher Lee, Will Xu, and JJ. RangamaniLabUCSD/smart, August 2025. doi: 10.5281/zenodo.10019463.

Chapter 7
Statistical Atlas-Based Surrogate Model of Biventricular Wall Mechanics

Raksha Konanur, Alejandra Robles, Anna Qi, Henrik Finsberg, Joakim Sundnes, and Andrew D. McCulloch

Abstract Here we use a statistical atlas of end-diastolic (ED) and end-systolic (ES) biventricular shapes – previously derived from the UK Biobank imaging substudy – to generate meshes for finite element (FE) simulations of ventricular wall mechanics. The models used the Holzapfel–Ogden constitutive law for passive material properties and a time-varying elastance model of systolic tension development. Simulated ED and ES deformations were projected onto the shape atlas and the principal components were used to train a multi-layer perceptron as a surrogate model. The input layer included shape modes of the unloaded ventricular geometry, and material parameters and ventricular pressures at ED and ES. After training with 444 simulations, the surrogate model achieved a mean square error in predicted displacements of < 2 mm and volumetric overlaps with FE-predicted deformed shapes $> 97\%$, demonstrating good fidelity to the simulated ground truth. This approach may enable accurate prediction of ventricular wall mechanics without computationally expensive finite element analysis, offering a more feasible method for rapid, subject-specific cardiac modeling.

Raksha Konanur
Department of Mechanical Engineering, University of California Berkeley, USA

Alejandra Robles
Department of Bioengineering, University of California San Diego, USA

Anna Qi
Department of Bioinformatics, University of California San Diego, USA

Henrik Finsberg
Department of Computational Physiology, Simula Research Laboratory, Norway

Joakim Sundnes (Corresponding author)
Department of Computational Physiology, Simula Research Laboratory, Norway e-mail: sundnes@simula.no

Andrew D. McCulloch
Department of Bioengineering and Department of Medicine, University of California San Diego, USA

K. J. McCabe, *Computational Physiology*, Simula SpringerBriefs on Computing 20, https://doi.org/10.1007/978-3-032-28826-4_7

Keywords: Ventricular mechanics, statistical shape atlas, principal components, finite element method, Holzapfel-Ogden law, surrogate model, machine learning

7.1 Introduction

Passive and active myocardial material properties are key determinants of regional ventricular wall mechanics and global pump function. Changes in material properties are important markers of cardiovascular aging, disease risk and progression [1, 2, 3]. However, because these properties cannot be measured directly, healthcare workers have used inverse models of ventricular biomechanics to estimate them.

Advances in medical imaging and inverse finite element (FE) modeling enable the construction of subject-specific models ("digital twins") of ventricular biomechanics. These advances allow us to estimate quantities that cannot be measured clinically including regional wall stress, strain distributions, and mechanical properties. Cardiac magnetic resonance imaging (MRI) and computed tomography resolve cardiac geometry throughout the cardiac cycle, including at end-diastolic (ED) and end-systolic (ES) states. Automated pipelines now allow these image volumes to be segmented and meshed into FE models automatically. The models can then simulate ventricular wall mechanics in these geometries given material properties and hemodynamic boundary conditions. Constitutive models have also been derived from in-vitro measurements in cardiac muscle. However, identifying patient-specific parameters typically requires costly inverse optimizations, which are performed by minimizing the residuals between model-predicted and observed wall displacements [4, 1, 5].

Material parameter optimization of FE models typically requires numerous iterations of large, nonlinear, 3D forward FE simulations. We aim to overcome this limitation by using deep learning to train a network that can serve as a surrogate FE model. However, since typical cardiac FE models can require tens of thousands of degrees of freedom to model ventricular shape and wall motion, the computations needed to train such a surrogate model could be computationally prohibitive.

Here we take advantage of statistical atlases of biventricular shape and wall motion derived using principal component analysis (PCA) from large databases of cardiac MRI exams, such as the UK Biobank Imaging Substudy [6, 7, 8]. These atlases greatly reduce dimensionality while preserving the features that explain variation across the population. The atlas can also be used to generate statistically representative synthetic geometries that can be shared publicly without the need for additional protections of individual health data. The atlas used here was derived from 38,858 UK Biobank cardiovascular MRI studies in healthy and diseased volunteers that includes both ED and ES biventricular shapes. The first 25 shape modes explained more than 90% of the shape variance across the cohort [8].

In this paper, we use finite element meshes generated from the UK Biobank biventricular atlas to generate synthetic, statistically representative data linking geometry, pressure, and material parameters. With the atlas as a latent space, FE solutions

resolved into shape modes were used to train and validate a surrogate model for predicting deformed deformed shapes of the heart given an unloaded geometry, chamber pressures, and material properties. Even with a modestly sized training set, the surrogate model predicted FE-computed deformed geometries with average errors under 1 mm and maximum errors less than 2 mm.

7.2 Methods

We developed a computational pipeline to simulate biventricular wall mechanics using a population-derived virtual cohort. Statistically representative geometries were obtained from pseudo-random samples of the first 25 modes of ED/ES shapes in a biventricular shape atlas derived from imaging substudy volunteers in UK Biobank [8]. Because FE models require an unloaded stress-free reference geometry, sampled ED shapes were adjusted with a heuristic to match extrapolated unloaded ventricular volumes. These unloaded geometries were then generated and meshed, assigned myocardial fiber architecture, and used for FE simulations of passive diastolic filling and active systolic contraction for physiologically relevant ranges of ventricular ED and ES pressures. Next, simulated deformed geometries were mapped back into atlas space, and used to train surrogate machine learning models. The full workflow is shown in Fig. 7.1.

7.2.1 Geometry and Hemodynamic Sampling

The biventricular meshes were generated from sampling the UK Biobank [9] and extracting the distribution of chamber volumes. Then using the first 25 shape modes of a biventricular statistical atlas of ED and ES shapes [6, 8], a synthetic cohort with PC scores representative of the aforementioned distribution was generated. A single set of PC scores, when projected back to the atlas, results in point clouds corresponding to RV and LV epicardial and endocardial surfaces at both ED and ES. Using arterial systolic pressures from the UKB cohort, plausible systolic blood pressures were sampled and used as LV ES pressures. LV and RV ED pressures were selected from normal values in human hearts [10]. Finally right ventricular ES pressures were computed by assuming a 9:4 ratio between the LV and RV respectively. This ratio was chosen based on the average ED pressure in the LV and RV. This ensured that the generated simulated hearts had LV to RV chamber volumes consistent with experimental data.

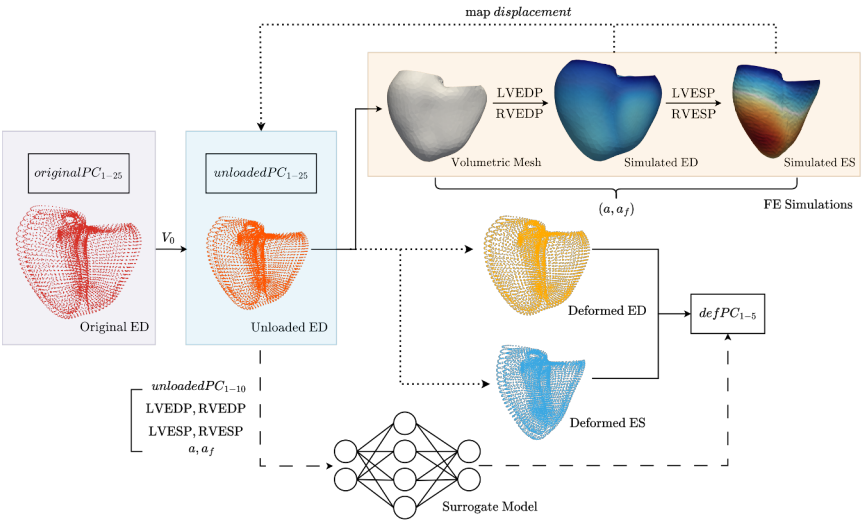

Fig. 7.1: Complete workflow beginning with the original PC scores from sampled atlas data to determining the deformed PC scores, then training and validating the surrogate model. Randomly sampled shape modes ($originalPC_{1-25}$) are adjusted to $unloadedPC_{1-25}$ via a heuristic to reduce ventricular size so that LVEDV approximates estimates unloaded volume V_0. Using this unloaded ED geometry, a volumetric FE mesh is constructed and deformed to ED given prescribed filling pressures (LVEDP, RVEDP) and to ES with prescribed systolic pressures (LVESP, RVESP) for ranges of passive and active stiffness scaling coefficients. Simulated ED and ES deformed geometry pairs are projected on to the atlas, resulting in the $defPC_{1-5}$. A MLP surrogate model was trained with inputs $unloadedPC_{1-10}$, pressures, and material properties and outputs $defPC_{1-5}$.

7.2.2 Generation of Unloaded Biventricular Meshes

To estimate the unloaded shape, we first determined the unloaded volume, V_0, of the LV. For the UK Biobank participants, V_0 was obtained by fitting the Klotz curve [11] to LVEDP and LVEDV. We then established a linear relationship (7.1) between V_0 and LVEDV with an $r^2 = 0.9968$.

$$V_0 = 0.5025\,\text{LVEDV} + 5.7574, \tag{7.1}$$

Using this estimated unloaded volume V_0, we used iterative gradient descent to find modified values of the shape mode scores of the model that reduced ED LV chamber volume to $V_0 \pm 0.1$ mL. LV volumes were computed from shape PCs using the Biventricular Modeling Pipeline (`biv-me`) [12]. The PC scores at the end of the optimization were assumed to correspond to subject-specific unloaded geometry at zero pressure.

The modified shape modes were projected back to the atlas and used to generate ED surface point clouds assumed to correspond to an equivalent unloaded geometry making use of the the `ukb-atlas` repository. Then, using `meshio` [13], surface meshes corresponding to the aortic valve (AV), mitral valve (MV), pulmonary valve (PV), tricuspid valve (TV), LV, RV, RV free wall, and the epicardium were constructed [14]. With `gmsh` [15], an unstructured volumetric mesh was constructed from these surfaces with a fixed characteristic length of 5.0 mm.

Fiber architecture was assigned to the unloaded meshes using the Laplace Dirichlet Rule-Based algorithm [16]. The myofiber helix angle was assumed to vary from +60° at the endocardium to −60° at the epicardium on both the LV and RV.

7.2.3 Myocardial Mechanics

Passive Properties

To describe the passive material properties of the myocardium, we used a transversely isotropic version of the hyperelastic strain energy function proposed by Holzapfel and Ogden (2009) [17]:

$$\Psi(F) = \frac{a}{2b}\left(e^{b(I_1-3)} - 1\right) + \frac{a_f}{2b_f}\left(e^{b_f(I_{4f_0}-1)^2} - 1\right), \tag{7.2}$$

where a, a_f, b, b_f are material parameters and the invariants I_1 and I_{4f_0} are defined as

$$I_1 = \mathrm{tr}(C), \qquad I_{4f_0} = f_0 \cdot (C f_0), \tag{7.3}$$

with C denoting the right Cauchy–Green tensor and f_0 the myocardial fiber direction. The myocardium is assumed to be incompressible, which we enforce with a Lagrange multiplier representing the hydrostatic pressure p in an augmented Lagrangian formulation [18, 19].

Constants b and b_f were set to 9.726 and 15.779 respectively based on biaxial testing data [20]. The parameters a and a_f, scaling the isotropic stress and the fiber stress, were varied as follows to generate six parameter combinations for each simulation: $a = 0.50$ and 1.28 kPa and $a_f = 1.7$, 10.0 and 20.0 kPa. These values were based on previous estimates for healthy myocardium [21] and biaxial testing [20].

Active Properties

Active contraction of the myocardium was represented using the formulation by Nash and Hunter (2000) [22]:

$$\sigma_a = T_a\left((f \otimes f) + \eta\,(I - f \otimes f)\right), \tag{7.4}$$

where T_a is the magnitude of the active fiber stress and η controls the proportion of active fiber tension generated in the transverse directions. Following previous studies, we assumed the transverse isotropy and fixed η to 0.2. T_a was set to 0.0 during the initial loading phase from unloaded to ED, and ramped up linearly 0.0 at ED to 200.0 kPa at ES.

7.2.4 FE Implementation

Simulations were performed in `FEniCSx` [19] with toolboxes for cardiac geometries and atlas meshing [23, 14]. The nonlinear solver uses Newton iterations with appropriate stabilization and convergence criteria. Taylor-Hood elements were used for pressures and displacements, with first-order Lagrange elements used for pressure and second-order Largrange elements for displacements.

Boundary Conditions

All valves (AV, MV, PV, TV) were assigned fixed Dirichlet boundary conditions, with the displacements set to zero. Neumann boundary conditions were used to impose the pressures in the left and right ventricles, similar to a previous study [24].

Loading

Loading was divided into two phases: passive loading of the unloaded geometry to ED pressure with no active stress, and the active loading of the ED geometry to ES with a linearly ramped active stress and pressure. The prescribed ED and ES pressures applied are summarized in Table 7.1.

Table 7.1: Pressure and active tension cases.

	Unloaded → ED (kPa)			ED → ES (kPa)		
Case	LV_{EDP}	RV_{EDP}	T_a	LV_{ESP}	RV_{ESP}	T_a
LOW	0.80	0.356	0.0	14.0	2.0	200.0
NORMAL	1.20	0.533	0.0	18.0	3.0	200.0
HIGH	1.60	0.711	0.0	25.0	4.0	200.0

Three sets of ED pressure were simulated: low, medium, and high. Applied LVESP were based on the distribution of systolic blood pressures in the UK Biobank cohort. The meshes were deformed from unloaded to ED by linearly load-stepping from unloaded to ED. No active stress was applied during the filling phase.

For each ED load, three sets of ES pressure pressures were applied to simulate systole corresponding to low, medium, and high ES pressures. In the ejecting phase,

an active tension (T_a) (refer Eq. 7.4) of 200.0 kPa was applied by linearly loadstepping from ED to the lowest ES case. While maintaining constant T_a, ES pressures were further increased to medium and then high cases. The final displacements at each pressure case for both ED and ES were saved. Thus, each combination of material parameters for each geometry resulted in 9 different ED-ES combinations.

7.2.5 Mapping to Atlas Space

To recover the PC scores from the deformed FE meshes, the deformed coordinates must be of expected length and order. This is required as the atlas expects coordinates in a particular order to maintain connectivity. However, since the simulations were performed on unstructured volumetric meshes, neither the order nor the connectivity is maintained. The mapping between the original coordinates and the nodes in the volumetric meshes is also unclear. To solve this problem, ED and ES displacements were mapped using a distance-weighted interpolation of the nearest 4 unloaded coordinates back to the original ED point cloud derived from the atlas and used to generate the unloaded mesh. These interpolated displacements were added to the coordinates of the point cloud corresponding to the unloaded atlas PCs. This preserves the ordering and number of the original coordinates, which can then be projected back onto the atlas to recover the PC scores for simulated deformed ED and ES pairs. Chamber volumes corresponding to the solutions were extracted from these point clouds using the `biv-me` package [12].

7.2.6 Surrogate Model

We trained a feedforward neural network to predict deformed principal component ($defPC$) scores from unloaded shape scores, ventricular pressures and material parameters.

Data preparation

Fifty sampled geometries were separated into 40 for training and 10 for testing. The input layer consisted of the first 10 shape modes ($unloadedPC_{1-10}$) of the unloaded geometry, LV and RV pressures at end-diastole and end-systole (LVEDP, LVESP, RVEDP, RVESP), and two material parameters (a, a_f), resulting in a 16-dimensional input vector. The active stress was not included in the training data as it was constant both at ED and at ES across all simulations. The target outputs were the first five principal components of the defomed meshes ($defPC_{1-5}$).

Model architecture

The machine learning model was a multilayer perceptron (MLP) with two hidden layers of 128 and 64 units, implemented using `PyTorch` [25]. Each hidden layer used a ReLU activation followed by dropout regularization ($p = 0.1$). The output layer was a fully connected linear mapping with 5 units (corresponding to $defPC_{1-5}$). In total, the network contained 10,757 trainable parameters. The architecture is summarized in Table 7.2.

Table 7.2: Architecture of the MLP used for defPC prediction.

Layer	Input size	Output size	Parameters
Linear + ReLU + Dropout	16	128	2,176
Linear + ReLU + Dropout	128	64	8,256
Linear (output)	64	5	325
Total	–	–	**10,757**

Training

The network was trained to minimize the mean squared error (MSE) between predicted and simulated deformed shape scores. Formally, for a batch of size N with predictions $\hat{\mathbf{y}}_i$ and targets $\mathbf{y}_i$, the loss function is:

$$\mathcal{L} = \frac{1}{N} \sum_{i=1}^{N} \|\hat{\mathbf{y}}_i - \mathbf{y}_i\|_2^2$$

This loss was minimized using the AdamW optimizer [26] with a learning rate of 5×10^{-6} and weight decay of 10^{-2}. Training was performed for up to 10,000 epochs using mini-batches of size 32. At each epoch, both training and validation losses were monitored, different hyperparameters were tested and the network state corresponding to the lowest validation loss was saved for evaluation.

Model Evaluation

Model performance was quantified using mean squared error (MSE) and the coefficient of determination (R^2), computed per $defPC$ component.

Geometric validation metrics

To quantitatively assess the geometric accuracy of the predicted deformations, reconstructed meshes from the predicted and true $defPC$ scores were compared using several metrics:

- **Hausdorff distance:** The maximum distance from any point on the predicted mesh to its nearest neighbor on the true mesh, and vice versa. This measures the largest local discrepancy between two surfaces.
- **Average point-to-point distance (AvgDist):** The mean Euclidean distance from each point on the predicted mesh to the closest point on the true mesh. This quantifies the overall surface deviation.
- **Point-cloud overlap percentage (Overlap):** The proportion of points on the predicted mesh that lie within a 2 mm threshold of the nearest point on the true mesh. This metric indicates the fraction of the predicted surface that closely matches the true geometry.

Hausdorff distance, average point-to-point distance, and point-cloud overlap were computed using nearest-neighbor queries implemented via `cKDTree` from `SciPy` [27]. All metrics were computed separately for end-diastolic (ED) and end-systolic (ES) meshes and summarized as mean ± standard deviation across the test set. These measures complement volumetric comparisons and provide a detailed assessment of local and global geometric fidelity. To compare these measurements to the displacements of the models, the mean and maximum of the absolute displacements were recorded for each simulation run at both ED and ES with respect to the original shape. The average of both of these values was reported.

7.3 Results

7.3.1 Simulation Workflow

An example result of the FEM simulations is given in Fig 7.2. On the left is the volumetric mesh of the unloaded geometry. The mesh is then loaded with LVEDP = $1.20kPa$, RVEDP = $0.533kPa$ to ED and then from ED to ES with LVESP = $18.0kPa$, RVESP = $3.0kPa$ with a linearly ramped active tension set to $200.0kPa$. The material properties were set to $a = 1.28kPa$, $a_f = 1.69kPa$.

7.3.2 Hemodynamic Distributions

The physiological plausibility of the generated training data was assessed by comparing their density distribution with that of the metrics sampled from the UK Biobank. In Fig. 7.3, the simulated, sampled and UK Biobank population distributions of

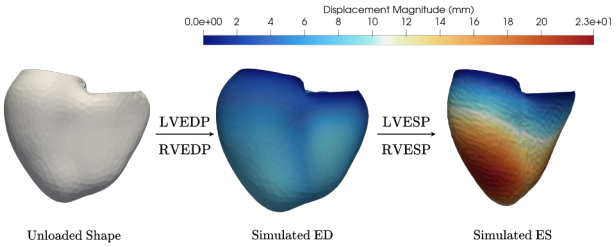

Fig. 7.2: Simulation workflow from unloaded volumetric mesh to ED, and finally ES. Magnitude of the deformations are given in millimeter.

LVED and LVES volumes are compared showing reasonable overlap, the simulated ED volumes tended to have lower values than population values. Similarly, since we generated solutions for high ES pressures, ejection fractions skewed lower than the data but simulations covered all but the highest values above 65%.

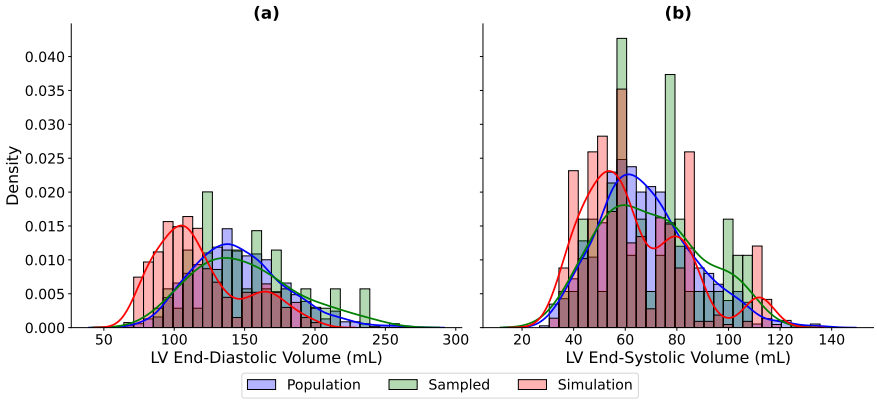

Fig. 7.3: Comparison of left ventricular (LV) end-diastolic (ED) and end-systolic (ES) volume distributions between the population, sampled and simulation cohort. Histograms show the empirical volume distributions, while the solid lines represent smoothed kernel density estimates (KDEs) for the population (blue), sampled (green), and simulations (red). Panel (a) shows the distributions at ED, with means at 145.83, 150.35, and 118.49 mL for the population, sampled, and simulated cohorts, respectively. Panel (b) shows the distributions at ES with means at 67.95, 69.94, and 63.53 mL for the population, sampled, and simulated cohorts, respectively.

To better assess the function of the simulated hearts, the ejection fractions (EFs) of the population, sampled and simulated data were compared, as seen in Fig. 7.4a. The simulation results fall in the range of the atlas cohort. The EF of the simulation results were further analyzed by looking at the distribution broken down by prescribed

LVESP. For the simulation, we used three conditions for LVESP as seen in Table 7.1, and these groups can be seen via Fig. 7.4b.

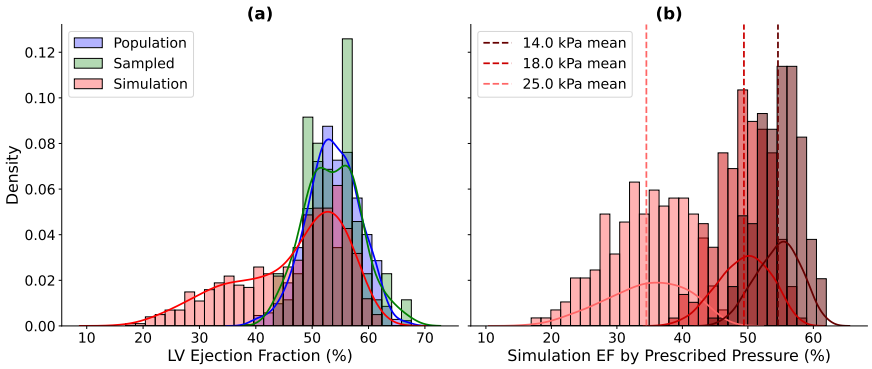

Fig. 7.4: Comparison of left ventricular (LV) ejection fraction (EF) distributions. Histograms show the empirical EF distributions, while the solid lines represent smoothed kernel density estimates (KDEs) for the population (blue), sampled (green), and simulations (red). Panel (a) compares the three cohorts with means at 53.68%, 53.68% and 46.23% for the population, sampled and simulation cohort, respectively. Panel (b) shows simulation EF distributions grouped by prescribed end-systolic pressure (LVESP), with mean EF values marked as dashed vertical lines: 54.60% at 14 kPa, 49.40% at 18 kPa, and 34.50% at 25 kPa.

7.3.3 Training Set

The final count of simulations achieved can be seen in Tables 7.3 and 7.4 using the pressure conditions described in Table 7.1 and material properties (7.2.3), respectively. Overall, unloaded geometries corresponding to 50 different sampled cases were used to create the simulation data. The same unloaded geometries were repeated with different end-diastolic pressures and material properties to achieve a total 576 simulations. Additional unloaded geometries were incorporated into the training set by running select material parameter combination (e.g. $a = 1.28, a_f = 1.7$) without having to cycle through all combinations. Since simulations with higher stiffness a converged more quickly, these material properties were somewhat over-represented in the final training set.

[1] A combination of both values was included due to user error.

[2] This value was discontinued after one run due to issues with convergence, but was still included in the training set.

Table 7.3: Simulation counts by LV/RV pressure (kPa)

PLVES	PLVED	PRVES	PRVED	Count
14	0.8	2	0.36	55
14	1.2	2	0.53	79
14	1.6	2	0.71	59
18	0.8	3	0.36	55
18	1.2	3	0.53	79
18	1.6	3	0.71	59
25	0.8	4	0.36	55
25	1.2	4	0.53	78
25	1.6	4	0.71	57
			Total Count	576
			Total Geometries	50

Table 7.4: Simulation counts by material properties (kPa)

a	a_f	Count
0.50	1.68/1.69[1]	80
0.50	10.0	69
0.50	20.0	60
1.28	1.00[2]	3
1.28	1.68/1.69[1]	185
1.28	10.0	89
1.28	20.0	90
	Total Count	576

7.3.4 Surrogate Performance

For both the training and validation groups, mean squared errors decreased monotonically with epochs (Fig. 7.5). Validation loss stabilized right before 3000 epochs, and the model with the lowest validation loss was selected as the best-performing model and retained for evaluation.

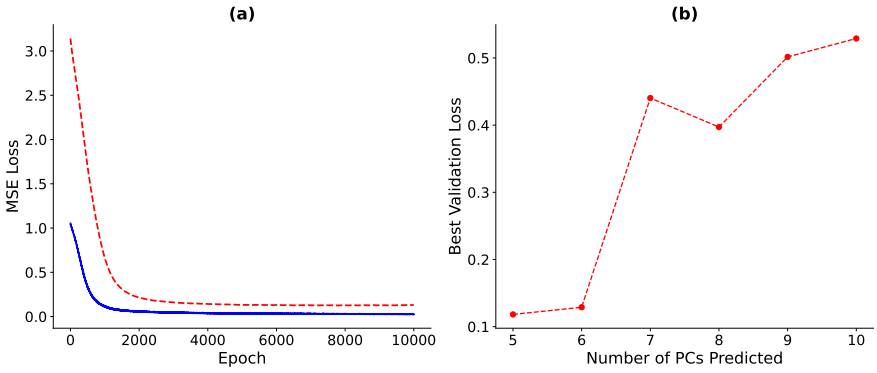

Fig. 7.5: Training dynamics of the multilayer perceptron (MLP). (a) The figure shows mean squared error (MSE) loss across epochs for both the training (blue) and validation (red) datasets for predicting 5 PCs. (b) Best validation loss (MSE) as a function of the number of predicted principal components (PCs), shown in red.

Scatter plots of predicted versus true values were used to visualize the performance of MLP for each deformed principal component ($defPC_{1-5}$) (Fig. 7.6). The scatter plots show most blue dots within their approximate 95% prediction intervals of

the line of identity: ±0.49 ($defPC_1$), ±1.40 ($defPC_2$), ±0.41 ($defPC_3$), ±0.42 ($defPC_4$), and ±1.07 ($defPC_5$). Discrepancies were greatest for $defPC_2$.

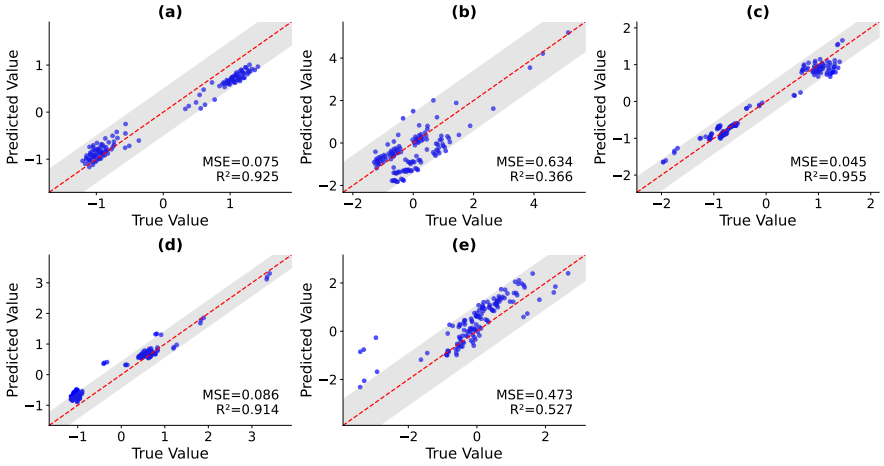

Fig. 7.6: Scatter plots of predicted versus true values for each deformed PC ($defPC_{1-5}$) in the test set. Panel a-e correspond to $defPC_{1-5}$, respectively. Each plot shows predicted PCs on the y-axis vs. true values on the x-axis, with a red dashed line indicating the line of unity. The shaded gray region indicates the 95% prediction interval. The MSE and R^2 values for each component are reported in the plot.

The performance of the trained model was also validated using geometric comparisons with ground truth simulation data (7.2.6). RMS Geometric prediction errors were < 1 mm, worst-case errors (Hausdorff distance) were around 2 mm, and volumetric overlaps between predicted and ground truth deformed geometries were > 97% (Table 7.5). In comparison, the average mean and maximum absolute displacements of the training data from unloaded to ED and then to ES were 2.4 and 4.0 mm, and 10.7 and 18.2 mm, respectively.

Table 7.5: Geometric validation metrics of predicted vs true meshes. Values are reported as mean ± standard deviation. Distances are in millimeters (mm) and overlap in percent (%).

Metric	**Mean ± Std**	Unit
Hausdorff_ED	1.69 ± 0.79	mm
Hausdorff_ES	1.81 ± 0.88	mm
AvgDist_ED	0.78 ± 0.37	mm
AvgDist_ES	0.77 ± 0.31	mm
Overlap_ED	97.58 ± 5.70	%
Overlap_ES	97.99 ± 4.18	%

7.4 Discussion

7.4.1 Key Findings

We found that a multilayer perceptron trained on PCA-based biventricular representations accurately predicts cardiac deformations, providing a fast and reliable surrogate for computationally expensive finite element simulations. This model was made possible by first developing a simulation workflow capable of producing physiologically plausible shapes, Fig. 7.2. As shown in Fig. 7.3, the simulated LV volumes fall within the range of the population. The mean simulated volumes, 119 mL and 64 mL, were slightly lower than the sampled population means of 146 mL and 68 mL for ED and ES, respectively. This difference may reflect the method used to compute the initial unloaded volumes (7.2.2) and the bias towards stiffer parameters in the training data (7.3.3). Exploring alternative approaches to defining the unloaded state or modifying material parameters could improve volume estimates; however, there are also many simulation constraints that can be fine-tuned.

The effect of simulation inputs is also evident in ejection fraction (EF) distributions (Fig. 7.4). While the overall EF distribution spans the sampled population's range of roughly 10–70%, it is not unimodal (Fig. 7.4a) like the population and sampled cohort. However, when grouping simulations by prescribed LVESP—14, 18, and 25 kPa(Fig. 7.4b)—the distributions within each cohort become unimodal, highlighting the strong dependence of EF on LVESP, with mean EF progressively decreasing as pressures rise, from 54.6% at 14 kPa to 49.4% at 18 kPa and 34.5% at 25 kPa, respectively. This trend falls in line with the expectation that a decrease in ES pressure will result in more ejection from the ventricle. This also suggests that producing additional simulations by linearly sweeping LVESP could improve robustness and better capture physiological variability.

However, it should be noted that the intention behind choosing the pressure and material parameters is not to match the training distributions of the population data, but to also span a wider range of pressures, volumes, and EFs. This broader coverage

is necessary because the sampled data was based on data from volunteers who were mostly healthy.

Using 50 unloaded geometries sampled from the population distribution, the surrogate model was trained to predict deformed shapes from input parameters. Fig. 7.5a illustrates the minimization of mean squared error (MSE) for both training and validation datasets when predicting $defPC_{1-5}$, which plateaued after approximately 3000 epochs, indicating convergence. Fig. 7.5b shows that as the number of $defPC$s included in the prediction increases, the best validation loss also increases even after 10,000 epochs. This trend suggests that the available dataset is insufficient to accurately predict higher-order PCs. While the validation loss remains below 0.2 for five and six $defPC$s, model performance is notably variable. A marked increase in loss occurs between predicting six and seven $defPC$s, indicating the onset of overfitting. Additionally, fluctuations in loss across predictions of $defPC_{1-8}$ highlight the sensitivity of the small dataset to local minima. Overall the model showed good training and validation loss with predicting $defPC_{1-5}$. Though insufficient for capturing the full extent of cardiac mechanics, it is a good start at understanding the range of data that will be needed to train a more extensive model.

When evaluating the ability of the model to predict $defPC_{1-5}$ (Fig. 7.6), the model shows the highest correlation, R^2, with $defPC_1$ at 0.94. This score corresponds to the size of the heart [6], and thus the model seems to be able to accurately predict the size of the heart. We see the worst correlation, R^2 of 0.451, with $defPC_2$. This PC score is associated with apex-base height. The range for $defPC_2$ in our simulated results was -5 to -1, which does not span the typical range of PC scores from about -3 to 3. This decreased correlation may be a result of the simulation parameters fixing the base's displacement inadvertently affecting the $defPC_2$ score. Because the atlas is built from real human data, it would be valuable to investigate the constraints placed on the bases in the simulations. Overall the mean R^2 of the model with all $defPC_{1-5}$ was 0.7864 with a mean RMSE of 0.2114. Clearly this is skewed down by $defPC_2$; however, this shows promising results that the model is performing well and with more training data it may improve.

The predicted and true $defPC_{1-5}$ scores were also evaluated by translating the scores back into 3D geometries. This showed with sub-millimeter average surface errors compared to the average displacements of 2.4 and 10.7 mm at ED and ES and volumetric overlaps above 97%, demonstrating high fidelity to the simulated ground truth (Table 7.5).

7.4.2 Limitations

Despite promising overall performance, the surrogate model shows residual variability in certain PC modes, reflecting sensitivity to training data diversity and the limited size of the validation cohort. Due to the small training set, the model was trained only on the first 10 PC scores and predicts the first 5 PC scores, which explains only 78.2% and 63.5% of the total shape variability, respectively. Thus, its

ability to reconstruct shapes corresponding to personalized data is currently truncated. These first 5 PC scores also may not be able to capture potentially important features of regional wall mechanics. The slightly lower simulated volumes compared to the sampled population suggest that both the method for calculating the unloaded state and the number of runs per condition may influence model fidelity. The unloaded shape was approximated using a simple linear heuristic. Although this may not significantly bias the surrogate model, subject-specific optimization will require a more accurate way of computing unloaded geometries consistent with the optimal material properties. This is an inverse dual problem itself. Additionally, reliance on prescribed LVESP for EF distributions indicates that the surrogate's predictive accuracy is partially dependent on the range and density of simulation inputs. The simulations were also only optimized on two global passive material parameters (a and a_f), whereas realistic optimizations would require spatially varying material properties, especially those corresponding to active contractile parameters.

Biases in the training data were also due to computational constraints. Simulations with stiffer material properties converged quickly and are therefore overrepresented, whereas less stiff material properties were excluded entirely due to the probative cost of smaller load steps. Thus, this resulted in a bias towards smaller geometries, stiffer hearts, and smaller EFs.

Finally, the boundary conditions applied on the tracts may have resulted in additional artifacts. The fixed Dirichlet boundary conditions (7.2.4) may be too restrictive, further resulting in smaller ED volumes and non-physiological deformations.

7.4.3 Future Work

Future work could expand the range of simulation conditions, including material properties, loading, and constraints, to increase the breadth of training simulations. The method of extracting the unloaded geometries could also be improved to be more consistent with the subject's unique material properties. A more diverse and expanded training set would enable the development of models with additional unloaded and deformed PC scores, helping to improve the realism of the reconstructed models. It could also be trained as an inverse model and used to predict material properties from deformed PC scores.

7.5 Conclusion

These results demonstrate that machine learning surrogates can generate physiologically realistic cardiac deformations at a fraction of the computational cost of full finite element simulations. This approach promises to enable rapid subject-specific optimization and supports large-scale virtual studies, reducing the need for repeated full-scale simulations. This lays the foundation to using machine learning to solve

the costly inverse challenge of determining material properties from biventricular end-diastolic and end-systolic geometries.

Data Availability

Code is available upon request.

Acknowledgments

We gratefully acknowledge the use of the cardiac atlas developed by Burns et al. [6]. AR was supported by the NIH grant NHLBI T32HL160507.

References

1. Sachin Govil, Nickolas Forsch, Sara Salehyar, Kathleen Gilbert, Avan Suinesiaputra, Sanjeet Hegde, James C. Perry, Alistair A. Young, Jeffrey H. Omens, and Andrew D. McCulloch. Morphological Markers and Determinants of Left Ventricular Systolic Dysfunction in Repaired Tetralogy of Fallot. In Volume 5: Biomedical and Biotechnology, page V005T05A033, Virtual, Online, November 2021. American Society of Mechanical Engineers.
2. Michael R. Zile, Catalin F. Baicu, John S. Ikonomidis, Robert E. Stroud, Paul J. Nietert, Amy D. Bradshaw, Rebecca Slater, Bradley M. Palmer, Peter Van Buren, Markus Meyer, Margaret M. Redfield, David A. Bull, Henk L. Granzier, and Martin M. LeWinter. Myocardial Stiffness in Patients With Heart Failure and a Preserved Ejection Fraction. Circulation, 131(14):1247–1259, April 2015. Publisher: American Heart Association.
3. Computational quantification of patient-specific changes in ventricular dynamics associated with pulmonary hypertension.
4. Oscar O. Odeigah, Ethan D. Kwan, Kristen M. Garcia, Henrik Finsberg, Daniela Valdez-Jasso, and Joakim Sundnes. A computational study of right ventricular mechanics in a rat model of pulmonary arterial hypertension. Frontiers in Physiology, 15, March 2024. Publisher: Frontiers.
5. Adarsh Krishnamurthy, Christopher Villongco, Amanda Beck, Jeffrey Omens, and Andrew McCulloch. Left Ventricular Diastolic and Systolic Material Property Estimation from Image Data. Statistical atlases and computational models of the heart. STACOM (Workshop), author, 8896:63–73, January 2015.
6. Richard Burns, William J. Young, Nay Aung, Luis R. Lopes, Perry M. Elliott, Petros Syrris, Roberto Barriales-Villa, Catrin Sohrabi, Steffen E. Petersen, Julia Ramírez, Alistair Young, and Patricia B. Munroe. Genetic basis of right and left ventricular heart shape. Nature Communications, 15(1):9437, November 2024.
7. Charlène Mauger, Kathleen Gilbert, Aaron M. Lee, Mihir M. Sanghvi, Nay Aung, Kenneth Fung, Valentina Carapella, Stefan K. Piechnik, Stefan Neubauer, Steffen E. Petersen, Avan Suinesiaputra, and Alistair A. Young. Right ventricular shape and function: cardiovascular magnetic resonance reference morphology and biventricular risk factor morphometrics in UK Biobank. Journal of Cardiovascular Magnetic Resonance, 21(1):41, July 2019.
8. Richard Burns, Laura Dal Toso, Charlène A. Mauger, Alireza Sojoudi, Avan Suinesiaputra, Steffen E. Petersen, Julia Ramírez, Patricia B. Munroe, and Alistair A. Young. Relationships between heart shape, function, and disease in 38,858 UK biobank participants. Journal of Cardiovascular Magnetic Resonance, 27(2):101919, December 2025.
9. Collins: UK biobank: protocol for a large-scale prospecti... - google scholar.
10. MSD Manuals. Normal pressures in the heart and great vessels, 2025. MSD Manual Professional Version, Merck & Co., Inc.
11. Stefan Klotz, Ilan Hay, Marc L. Dickstein, Geng-Hua Yi, Jie Wang, Mathew S. Maurer, David A. Kass, and Daniel Burkhoff. Single-beat estimation of end-diastolic pressure-volume relationship: a novel method with potential for noninvasive application. American Journal of Physiology. Heart and Circulatory Physiology, 291(1):H403–412, July 2006.
12. Joshua R Dillon, Charlène Mauger, Debbie Zhao, Yu Deng, Steffen E Petersen, Andrew D McCulloch, Alistair A Young, and Martyn P Nash. An open-source end-to-end pipeline for generating 3d+ t biventricular meshes from cardiac magnetic resonance imaging. In International Conference on Functional Imaging and Modeling of the Heart, pages 372–383. Springer, 2025.
13. Nico Schlömer. meshio: Tools for mesh files, 2018. Version archived on Zenodo.
14. Henrik Finsberg and Lisa R Pankewitz. Uk biobank atlas - mesh generation, 2024.
15. Christophe Geuzaine and Jean-François Remacle. Gmsh: a three-dimensional finite element mesh generator with built-in pre- and post-processing facilities. International Journal for Numerical Methods in Engineering, 79(11):1309–1331, 2009.
16. J. D. Bayer, R. C. Blake, G. Plank, and N. A. Trayanova. A Novel Rule-Based Algorithm for Assigning Myocardial Fiber Orientation to Computational Heart Models. Annals of biomedical engineering, 40(10):2243–2254, October 2012.

17. Gerhard A. Holzapfel and Ray W. Ogden. Constitutive modelling of passive myocardium: a structurally based framework for material characterization. Philosophical Transactions of the Royal Society A: Mathematical, Physical and Engineering Sciences, 367(1902):3445–3475, September 2009. Publisher: Royal Society.
18. A Gerhard Holzapfel. Nonlinear solid mechanics. John Wiley & Sons, Inc., 2000.
19. Henrik Finsberg. pulse: A python package based on FEniCS for solving problems in cardiac mechanics. Journal of Open Source Software, 4(41):1539, September 2019.
20. Socrates Dokos, Bruce H. Smaill, Alistair A. Young, and Ian J. LeGrice. Shear properties of passive ventricular myocardium. American Journal of Physiology-Heart and Circulatory Physiology, 283(6):H2650–H2659, December 2002. Publisher: American Physiological Society.
21. H. Gao, W. G. Li, L. Cai, C. Berry, and X. Y. Luo. Parameter estimation in a Holzapfel–Ogden law for healthy myocardium. Journal of Engineering Mathematics, 95(1):231–248, 2015.
22. M. P. Nash and P. J. Hunter. Computational Mechanics of the Heart. Journal of elasticity and the physical science of solids, 61(1):113–141, July 2000.
23. Henrik Finsberg. Releases · ComputationalPhysiology/cardiac-geometries.
24. Henrik Finsberg, Ce Xi, Ju Le Tan, Liang Zhong, Martin Genet, Joakim Sundnes, Lik Chuan Lee, and Samuel T. Wall. Efficient estimation of personalized biventricular mechanical function employing gradient-based optimization. International Journal for Numerical Methods in Biomedical Engineering, 34(7):e2982, 2018. _eprint: https://onlinelibrary.wiley.com/doi/pdf/10.1002/cnm.2982.
25. Adam Paszke, Sam Gross, Soumith Chintala, Gregory Chanan, Edward Yang, Zachary DeVito, Zeming Lin, Alban Desmaison, Luca Antiga, and Adam Lerer. Automatic differentiation in pytorch. In NIPS-W, 2017.
26. Diederik P. Kingma and Jimmy Ba. Adam: A Method for Stochastic Optimization, January 2017. arXiv:1412.6980 [cs].
27. Pauli Virtanen, Ralf Gommers, Travis E. Oliphant, Matt Haberland, Tyler Reddy, David Cournapeau, Evgeni Burovski, Pearu Peterson, Warren Weckesser, Jonathan Bright, Stéfan J. van der Walt, Matthew Brett, Joshua Wilson, K. Jarrod Millman, Nikolay Mayorov, Andrew R. J. Nelson, Eric Jones, Robert Kern, Eric Larson, C J Carey, İlhan Polat, Yu Feng, Eric W. Moore, Jake VanderPlas, Denis Laxalde, Josef Perktold, Robert Cimrman, Ian Henriksen, E. A. Quintero, Charles R. Harris, Anne M. Archibald, Antônio H. Ribeiro, Fabian Pedregosa, Paul van Mulbregt, and SciPy 1.0 Contributors. SciPy 1.0: Fundamental Algorithms for Scientific Computing in Python. Nature Methods, 17:261–272, 2020.

Chapter 8
Comparing the Hopfield Network and Sparse Distributed Memory Model in Pattern Completion

Anna Mihály, Morgan Fitzgerald, Henrik Formoe, and Nicolai Haug

Abstract Pattern completion, the ability to retrieve a complete memory from a partial cue, is a fundamental cognitive process. To explore its underlying neural computations, we compared two canonical associative memory models: the Hopfield network and the Sparse Distributed Memory (SDM) model. Using a binarized version of the MNIST handwritten digit dataset, we tested each model's ability to reconstruct original patterns from cues degraded by varying levels of pixel-flip noise. Our results revealed distinct performance profiles. The Hopfield network demonstrated high fidelity recall under low-to-moderate noise but failed abruptly when noise levels became too high. Conversely, the SDM model's performance gradually decreased with increased noise. The SDM model preserved partial features of the original memory even under significant noise, though it never achieved perfect reconstruction. These findings demonstrate two complementary strategies for associative memory: the Hopfield network's attractor dynamics favor accuracy within a limited stability region, whereas the SDM's distributed architecture promotes robustness at the cost of precision. This dichotomy highlights how different computational principles may map onto different functional roles of brain regions, such as the high fidelity pattern completion of the hippocampus and the robust, feature based retrieval of cortical memory systems.

Anna Mihály
Institute of Basic Medical Sciences, Department of Molecular Medicine, University of Oslo, Norway

Morgan Fitzgerald
Department of Neuroscience, University of California San Diego, USA

Henrik Formoe
Department of Psychology, University of Oslo, Norway

Nicolai Haug (corresponding author)
Department of Numerical Analysis and Scientific Computing, Simula Research Laboratory, Norway and Department of Physics, University of Oslo, Norway. e-mail: nicolaih@simula.no

K. J. McCabe, *Computational Physiology*, Simula SpringerBriefs on Computing 20, https://doi.org/10.1007/978-3-032-28826-4_8

8.1 Introduction

Memory is the ability by which the brain encodes, stores, and retrieves information. This complex process serves as a record of experience that is essential for learning, guiding present actions, and planning for the future. Located deep within the brain's medial temporal lobes, the hippocampal formation is one of the most studied neuronal systems and has long been a central focus in memory research [1]. Its critical role was famously and tragically illustrated by the case of patient H.M., who, after surgical removal of the hippocampus, was left with an inability to form new long-term memories [2]. This case provided the foundational evidence that the hippocampus is essential for transforming fleeting short-term experiences into lasting memories, a process known as memory consolidation. The hippocampus is now understood to be critical for both episodic memory—the rich, contextual record of personal experiences—and spatial memory, which involves creating cognitive maps of the environment [3]. To accomplish these functions, the hippocampus performs complementary computations linked to different hippocampal subfields. It uses pattern separation to store similar experiences as distinct memories, preventing interference, and pattern completion to retrieve a full memory from a partial or noisy cue [4].

A central challenge in neuroscience is understanding precisely how neural circuits like the hippocampus perform these computations. To explore this question, researchers use computational models to simulate and test theories of memory. This project focuses on two influential models of associative memory: the Hopfield network [5] and Sparse Distributed Memory (SDM) [6]. By implementing and comparing these two architectures on a pattern completion task, we aim to explore different computational strategies for memory retrieval and shed light on the principles that may underlie biological memory systems.

8.2 Methods

8.2.1 The Hopfield Network

One of the earliest and most influential computational models of memory is the Hopfield network, introduced by John Hopfield in 1982 [5]. The Hopfield network functions as a form of content-addressable memory, meaning it can retrieve a full memory based on the content of a partial or noisy cue. The network operates in two phases. In the storage phase, memories are encoded into the synaptic weights according to a Hebbian-like principle ("neurons that fire together, wire together"), establishing each pattern as a stable attractor state in the network's dynamics. Subsequently, in the retrieval phase, the network dynamically converges to the nearest attractor state when presented with a partial or noisy cue, thereby completing the pattern and recalling the full memory.

The Hopfield network is a fully connected recurrent network consisting of N McCulloch-Pitts neurons [7], that is, binary threshold neurons. Each neuron i is characterized by a state, denoted by

$$s_i = \begin{cases} +1 & \text{active,} \\ -1 & \text{inactive.} \end{cases}$$

Which value the state takes on is determined by whether the neuron's input exceeds its threshold θ_i. The network's dynamics evolves in discrete time with time steps Δt. There is no refractoriness, and the duration of a time step is typically not specified. However, if we take $\Delta t = 1\,\text{ms}$, $s_i(t) = +1$ can be interpreted as neuron i firing an action potential at time t [8]. The strength of the connection between neuron i and neuron j is defined by a synaptic weight, w_{ij}. In the classical Hopfield network, these connections are symmetric ($w_{ij} = w_{ji}$) and neurons do not connect to themselves ($w_{ii} = 0$). The state of each neuron i is updated based on the weighted input from other neurons:

$$s_i\,(t + \Delta t) = \operatorname{sgn}\left(\sum_j w_{ij} s_j(t) - \theta_i\right) \equiv \operatorname{sgn}\left[h_i(t)\right]. \tag{8.1}$$

In this project, we follow the typical convention of setting $\Delta t = 1$ and $\theta_i = 0$, such that Equation 8.1 becomes

$$s_i\,(t + 1) = \operatorname{sgn}\left(\sum_j w_{ij} s_j(t)\right) \equiv \operatorname{sgn}\left[h_i(t)\right]. \tag{8.2}$$

Here, $\operatorname{sgn}(h)$ is the signum function

$$\operatorname{sgn}(h) = \begin{cases} +1, & h \geq 0, \\ -1, & h < 0. \end{cases}$$

Figure 8.1 illustrates the computation of a McCulloch-Pitts neuron. Note that the computation of Equation 8.2 is performed synchronously, that is, all neurons are updated at the same time in parallel. Updates in the Hopfield network can also be performed asynchronously, that is, only one neurons is updated at a time. We only consider synchronous updates in this project.

The Hopfield network's dynamics are determined by an energy function, $E\,(\boldsymbol{s})$, which is defined for a state vector $\boldsymbol{s} = (s_1, s_2, ..., s_N)$. If there are no self-connections and the connections are symmetric, the Hopfield network has the energy function

$$E\,(\boldsymbol{s}) = -\frac{1}{2}\sum_{i,j} w_{ij} s_i s_j - \sum_i \theta_i s_i. \tag{8.3}$$

The update rule in Equation 8.1 is derived from minimizing the energy function given by Equation 8.3. The quantity in Equation 8.3 is called "energy" because it either decreases or stays the same upon network neurons being updated. The

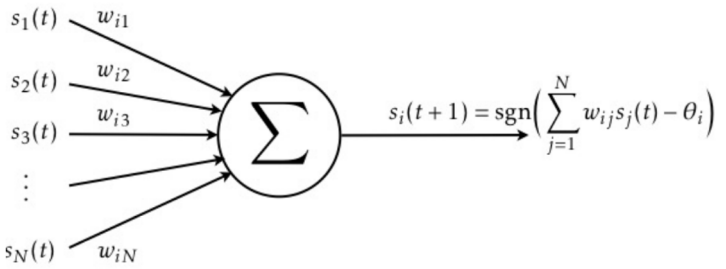

Fig. 8.1: Schematic diagram of the computation of a McCulloch-Pitts neuron. Retrieved from [9].

constraint that weights are symmetric guarantees that the energy function decreases monotonically while following the update rule (Equation 8.1).

To store a set of P memory patterns, $\{\boldsymbol{\xi}^{\mu}\}_{\mu=1}^{P}$, the synaptic weights are set according to the Hebbian learning rule. This rule strengthens the connection between any two neurons that are in the same state within a given pattern:

$$w_{ij} = \frac{1}{N} \sum_{\mu=1}^{P} \xi_i^{\mu} \xi_j^{\mu} \qquad (i \neq j). \tag{8.4}$$

This process shapes an "energy landscape" where the desired memory patterns become stable local minima, see Figure 8.2. Because the Hebbian storage rule makes the target memories local minima of the energy landscape, the network's evolution naturally performs memory recall. When presented with a distorted input, the network simply follows its dynamics toward the nearest energy minimum, which corresponds to the most similar stored memory. This process of energy minimization is the mechanism of associative recall in the Hopfield network.

8.2.2 Sparse Distributed Memory

Sparse distributed memory was proposed by Pentti Kanerva in 1988 as a model for human long-term memory [6]. It is an associative memory model that operates in a very high-dimensional binary space. Instead of converging to a single, perfect state like an attractor network, the system produces an averaged reconstruction of similar past inputs, making its recall inherently robust but approximate.

The SDM architecture is defined by three key components:

1. **Address Space:** A high-dimensional binary vector space $\{0, 1\}^N$, where N is typically large (e.g., $N = 1000$). Each possible input pattern corresponds to a point in this space.

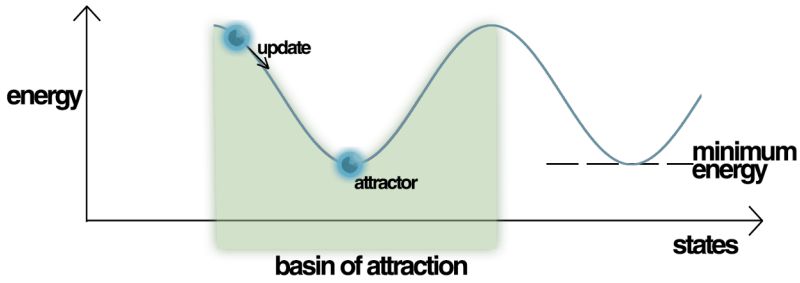

Fig. 8.2: The energy landscape of a Hopfield network. The current state is at a high energy level. The network's update rule guarantees that the state will move "downhill" toward a lower energy configuration, eventually settling in a stable attractor state (a local minimum). The green shaded area represents the basin of attraction for that particular memory. Retrieved from [10].

2. **Hard Locations:** A fixed, randomly chosen set of M memory locations, $\{\boldsymbol{a}^k\}_{k=1}^{M}$, where each $\boldsymbol{a}^k \in \{0,1\}^N$ is a "hard address". The number of hard locations M is large, but sparse relative to the size of the address space ($M \ll 2^N$).
3. **Memory Contents:** An $M \times D$ matrix of integer counters, C, where D is the dimension of the data vectors being stored. Each row $\boldsymbol{c}^k$ corresponds to a hard location $\boldsymbol{a}^k$ and contains D counters, one for each dimension of the data.

Activation of hard locations is determined by the Hamming distance, $d_H(\boldsymbol{x}, \boldsymbol{y})$, which counts the number of differing bits between two binary vectors $\boldsymbol{x}$ and $\boldsymbol{y}$. A hard location $\boldsymbol{a}^k$ is considered active for a given input address $\boldsymbol{x}$ if it lies within a specified access radius r:

$$d_H(\boldsymbol{x}, \boldsymbol{a}^k) \leq r. \tag{8.5}$$

To store a D-dimensional binary data vector $\boldsymbol{d} \in \{0,1\}^D$ at a given address $\boldsymbol{x} \in \{0,1\}^N$, the system first identifies all active hard locations. For the update, the binary values are treated as bipolar signals ($1 \rightarrow +1$, $0 \rightarrow -1$). For each active location k, its counter vector $\boldsymbol{c}^k$ is updated as follows for each dimension j:

$$c_j^k \leftarrow c_j^k + (2d_j - 1) \, \forall k \text{ s.t. } d_H(\boldsymbol{x}, \boldsymbol{a}^k) \leq r. \tag{8.6}$$

This increments the corresponding counter for a '1' bit and decrements it for a '0' bit. Because multiple addresses activate an overlapping set of hard locations, a single data pattern is distributed across many rows of the memory matrix C.

To retrieve a memory from a cue address $\boldsymbol{x'}$, the system again identifies all hard locations activated by $\boldsymbol{x'}$. The contents of these active locations are then pooled by summing their counter vectors into a single D-dimensional sum vector, $\boldsymbol{h}$:

$$\boldsymbol{h} = \sum_{k \text{ s.t. } d_H(\boldsymbol{x}', \boldsymbol{a}^k) \leq r} \boldsymbol{c}^k. \tag{8.7}$$

The final reconstructed binary data vector, $\hat{\boldsymbol{d}}$, is obtained by thresholding the sum vector at zero:

$$\hat{d}_j = \begin{cases} 1, & \text{if } h_j \geq 0, \\ 0, & \text{if } h_j < 0. \end{cases} \tag{8.8}$$

This pooling and thresholding process averages the contributions from many similar stored patterns, leading to robust but approximate recall. Figure 8.3 illustrates the SDM model.

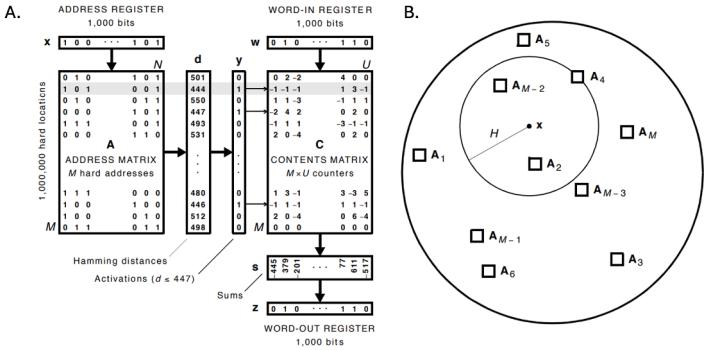

Fig. 8.3: Illustration of the sparse distributed memory. **A.** Structure of the model, the grey shade indicates the first selected memory location. **B.** Illustration of the address space. The set of activated cells indicated by x, H is the Hamming distance (radius) of activation. Retrieved from [11].

8.3 Results

We implemented and compared the Hopfield network and Sparse Distributed Memory (SDM) model to evaluate their pattern completion capabilities using the MNIST dataset. We systematically corrupted test images with noise to measure how accurately each model could recall the original patterns from these degraded cues.

8.3.1 Experimental Design, Data Preparation, and Performance Metrics

The original MNIST dataset consists of 60,000 training and 10,000 test images of 28x28 pixel grayscale images of handwritten digits (0-9). Each image is labeled with the corresponding digit. The pixel values in the original dataset range from 0 to 255, representing the intensity of grayscale. Because the Hopfield network and SDM model operates on binary patterns, the grayscale MNIST images were first normalized to the range $[0, 1]$ and then binarized.

For the Hopfield network, we used a bipolar encoding where all pixel values greater than or equal to 0.5 were set to 1 (white), while values below 0.5 were set to -1 (black). To lessen the computational burden, we used a subset of the dataset (digits 0-4) and downsampled the images from 28×28 to 20×20 pixels via nearest-neighbor interpolation, see Figure 8.4. This reduction preserved the essential shape of the digits while lowering the Hopfield network's state size.

For the SDM model, we again applied the threshold pixel value at 0.5 but with a binary encoding with 1 (white) and 0 (black). We did not apply downsampling for the SDM model, thus the input dimensionality was preserved at 28x28 = 784 pixels. We also used the same subset of the MNIST dataset (digits 0-4).

To evaluate recall robustness, we introduced pixel-flip noise to the test images. Each pixel's value was inverted with a probability p, where p ranged from 0.0 (no noise) to 0.70 in 0.05 increments (Figure 8.4). This procedure allowed us to simulate increasingly degraded cues and systematically probe the stability of each model's memory states.

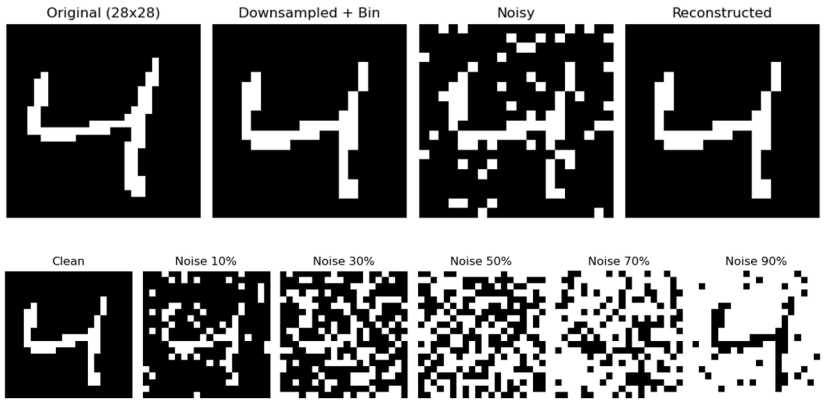

Fig. 8.4: Data preprocessing and noise protocol for a sample MNIST digit. The original image is downsampled and binarized, after which pixel-flip noise is applied at increasing levels of probability.

We quantified reconstruction quality using pixel accuracy, defined as the fraction of identical pixels between the clean, original image pattern x and the reconstructed image pattern $\hat{x}$:

$$\text{Accuracy}\,(x, \hat{x}) = \frac{1}{N} \sum_{i=1}^{N} 1\,\{x_i = \hat{x}_i\}\,. \tag{8.9}$$

We used the Hamming loss to measure the fraction of mismatched pixels:

$$\text{HammingLoss}\,(x, \hat{x}) = \frac{1}{N} \sum_{i=1}^{N} 1\,\{x_i \neq \hat{x}_i\} = 1 - \text{Accuracy}\,(x, \hat{x})\,. \tag{8.10}$$

8.3.2 Hopfield Network Performance

In our experiments with the Hopfield network, we performed ten synchronous update steps per trial. As shown in Figure 8.5, the Hopfield network successfully performed pattern completion, demonstrating high tolerance to noise up to a critical threshold. At low noise levels ($p < 0.5$), the network's recall accuracy was high and stable, plateauing at approximately 82%. This ceiling below 100% is not a model failure but a consequence of generalization. The network was evaluated on a set of digit patterns withheld during the training phase. Therefore, the digit patterns used for evaluation were not identical to the stored patterns. The plateau at about 82%, even in the absence of noise, reflects the baseline similarity between unseen and stored digit patterns. Performance remained robust until the noise level approached $p \approx 0.5$. In this regime, the corrupted inputs were still within the basin of attraction of the correct memory, allowing the network to reliably converge to the target pattern. However, as noise increased beyond this point, performance dropped sharply. At $p = 0.6$, mean accuracy fell from over 80% to below 20%, indicating that the network was converging to an incorrect attractor or a spurious state. This sharp transition is a hallmark of attractor networks. Recall is highly effective within the attractor's basin but fails abruptly once a corrupted cue falls outside this boundary. This behavior illustrates how a recurrent network can achieve precise recall but at the cost of a limited operational range.

8.3.3 Sparse Distributed Memory Model Performance

Our SDM was implemented using the `torchhd` Python library [12], specifically the module `torchhd.memory. SparseDistributed`. We configured the model with a hypervector dimension of $N = 2,000$ and a memory size of $M = 100,000$ hard locations. Instead of a fixed Hamming radius, the activation was determined by a

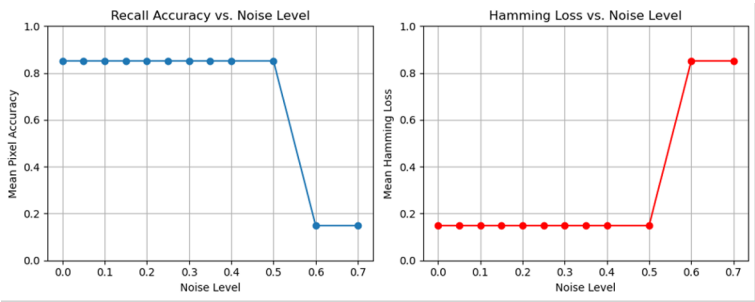

Fig. 8.5: Recall performance of the Hopfield network. Left panel: Mean pixel accuracy is plotted against increasing levels of pixel-flip noise, illustrating a stable performance plateau followed by a sharp decline. Right panel: Similar to the left panel, but shows the Hamming loss (inverted pixel accuracy) to visualize the level of pixel mismatch.

sparsity parameter $p = 0.005$. For any given input cue, this method activates the $k = p \times M = 500$ hard locations with the smallest Hamming distance for both reading and writing. This approach ensures a consistent number of locations are accessed for each operation, providing a stable balance between specificity and robustness.

The SDM's performance, shown in Figure 8.6, contrasted sharply with the Hopfield network. Instead of an abrupt failure, the SDM exhibited a graceful degradation as noise increased. Accuracy was never perfect, starting at approximately 70% for clean inputs and declining smoothly as corruption was added. Qualitatively, reconstructions retained a blurred but recognizable outline of the digit at moderate noise levels, only becoming an indistinct average under heavy corruption. This demonstrates a "something-is-better-than-nothing" approach, which is fundamentally different from the Hopfield network's all-or-none behavior.

This result stems from the SDM's architecture. Where the Hopfield network forces a convergence to a single, discrete attractor, the SDM retrieves an average of all memories stored within a given neighborhood of the cue. This distributed retrieval process guarantees robustness against catastrophic failure but inherently sacrifices the potential for perfect, high-fidelity recall.

8.4 Discussion

Our comparative analysis of the Hopfield network and Sparse Distributed Memory (SDM) model reveals two fundamentally different strategies for pattern completion. While both models successfully reconstructed corrupted MNIST digits, their distinct recall dynamics and failure modes underscore a classic tradeoff between precision

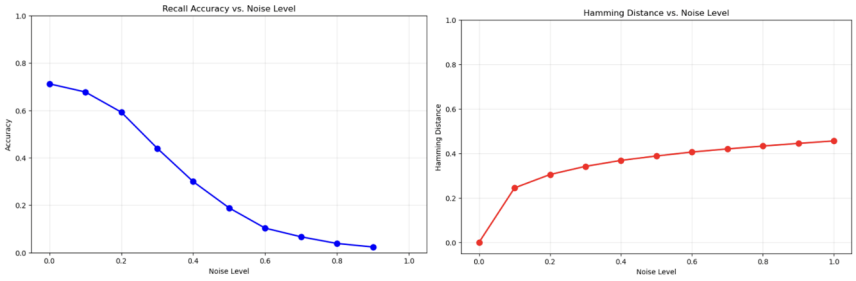

Fig. 8.6: Recall performance of the Sparse Distributed Memory model. Left panel: Mean pixel accuracy is plotted against increasing levels of pixel-flip noise, showing a gradual and continuous decline. Right panel: Similar to the left panel, but shows the Hamming loss (inverted pixel accuracy) to visualize the level of pixel mismatch.

and robustness in associative memory. This difference is rooted in their underlying architectural principles.

The Hopfield network demonstrated a clear all-or-none behavior. It achieved high recall accuracy, holding steady around 82% even when inputs were distorted with up to 50% noise. This is a result of the network's design as a content-addressable memory. Each stored digit creates a stable attractor state in the network's energy landscape, similar to a valley in a topographical map. When a noisy input is presented, the network's dynamics guide the pattern toward the bottom of the nearest valley, which restores the original memory. The network's accuracy peaked at 82% for two main reasons. First, the model was evaluated on an unseen test set, so it had to generalize from the patterns it learned during training. Since the test digits were not identical to the training examples, a perfect 100% score was not expected. Second, different handwritten digits can be highly correlated. For instance, a '7' can closely resemble a '1', or a '3' can look like an '8'. This similarity between patterns creates crosstalk in the memory, where the network can retrieve a similar but incorrect digit, further limiting its overall accuracy.

In contrast, the SDM exhibited a gradual decline in recall accuracy with increasing noise. Its accuracy was never perfect, starting at 70% with no noise and declining smoothly to 60% at 20% noise, and down to just 10% at 60% noise. This behavior is a direct result of its distributed architecture, which was inspired by the vast, sparse connectivity of the brain's cerebellum. In an SDM, a single memory is not stored in one location. Instead, it is written across thousands of different memory locations that are "close enough" to the input pattern. Recall is a collective process. The system retrieves and effectively averages the data from all the relevant storage locations. Consequently, the reconstructed digits were often blurry composites of multiple memory traces, becoming averaged shapes at high noise levels. The SDM consistently provides an approximate answer, even from a heavily corrupted cue. It

sacrifices the potential for perfect accuracy in exchange for exceptional robustness against complete failure.

The contrasting behaviors of the Hopfield network and the SDM model provide a useful computational metaphor for understanding biological memory systems. Hopfield-like attractor dynamics are consistent with the function of the hippocampal CA3 subfield, where extensive recurrent excitatory connections support rapid and discrete pattern completion. For this reason, the Hopfield network has long been considered a foundational model for understanding how the hippocampal CA3 subfield might support memory retrieval [4]. While the Hopfield network has limitations, such as a finite storage capacity and difficulty distinguishing between similar patterns, its principles remain fundamental for illustrating how associative memory can emerge from recurrent circuits. SDM-like distributed averaging, on the other hand, resembles cortical memory, where overlapping representations support generalization and robustness to noise at the cost of exact recall. This comparison suggests that biological memory systems evolved different neural architectures to balance precision and robustness. By specializing different brain regions for each strategy, the brain creates a division of labor that allows it to operate effectively in various situations.

8.5 Conclusion

In this project we implemented and compared two canonical models of associative memory: the Hopfield network and the Sparse Distributed Memory (SDM). Both models successfully demonstrated pattern completion, but with distinct behaviors. The Hopfield network demonstrated high fidelity recall under low-to-moderate noise but failed abruptly when noise levels became too high. SDM demonstrates how distributed storage leads to robust memory. While it does not achieve the absolute, all or nothing retrieval of Hopfield's attractor network, SDM's key feature is gradual decrease of recall accuracy in the face of increasing noise. Viewed in a biological context, these models may capture different aspects of memory processing across brain regions. The hippocampal CA3 may prioritize high-fidelity pattern completion through discrete attractor dynamics, while cortical networks likely favor distributed, feature-based retrieval for its robustness.

Both the Hopfield network and SDM model are limited by their assumption on simple, binary data, which is rarely the case in real-world applications. Future work should therefore focus on scaling these principles of precision and robustness to more complex memory tasks, for instance by using modern continuous-state Hopfield networks [13, 14] or Kanerva machines [15]. By comparing models of associative memory in a controlled setting, we can gain deeper insights into how precision and robustness emerge from different neural architectures in both biological and artificial systems.

References

1. J. J. Knierim. The hippocampus. Current Biology, 25(23):R1116–R1121, 2015.
2. W. B. Scoville and B. Milner. Loss of recent memory after bilateral hippocampal lesions. Journal of Neurology, Neurosurgery, and Psychiatry, 20(1):11–21, 1957.
3. N. Burgess, E. A. Maguire, and J. O'Keefe. The human hippocampus and spatial and episodic memory. Neuron, 35(4):625–641, 2002.
4. E. T. Rolls. The mechanisms for pattern completion and pattern separation in the hippocampus. Frontiers in Systems Neuroscience, 7:74, 2013.
5. J. J. Hopfield. Neural networks and physical systems with emergent collective computational abilities. Proceedings of the National Academy of Sciences, 79(8):2554–2558, 1982.
6. P. Kanerva. Sparse Distributed Memory. MIT Press, 1 edition, 1988.
7. W. S. McCulloch and W. Pitts. A logical calculus of the ideas immanent in nervous activity. The bulletin of mathematical biophysics, 5(4):115–133, 1943.
8. W. Gerstner, W. M. Kistler, R. Naud, and L. Paninski. Neuronal dynamics : from single neurons to networks and models of cognition. Cambridge University Press, Cambridge, United Kingdom, 1 edition, 2014.
9. B. Mehlig. Machine learning with neural networks : an introduction for scientists and engineers. Cambridge University Press, Cambridge, United Kingdom, 1 edition, 2022.
10. Wikimedia Commons. Energy landscape of a hopfield network, 2013. File: Energy_landscape.png.
11. P. Kanerva. Sdm and related models. In M. H. Hassoun, editor, Associative Neural Memories: Theory and Implementation, chapter 3, pages 50–76. Oxford University Press, New York, 1 edition, 1993.
12. Mike Heddes, Igor Nunes, Pere Vergés, Denis Kleyko, Danny Abraham, Tony Givargis, Alexandru Nicolau, and Alex Veidenbaum. Torchhd: An open source python library to support research on hyperdimensional computing and vector symbolic architectures. Journal of Machine Learning Research, 24(255):1–10, 2023.
13. D. Krotov and J. J. Hopfield. Dense associative memory for pattern recognition. In D. Lee, M. Sugiyama, U. Luxburg, I. Guyon, and R. Garnett, editors, Advances in Neural Information Processing Systems, volume 29, 2016.
14. H. Ramsauer, B. Schäfl, J. Lehner, P. Seidl, M. Widrich, T. Adler, L. Gruber, M. Holzleitner, M. Pavlović, G. K. Sandve, V. Greiff, D. P. Kreil, M. K. Kopp, G. Klambauer, J. Brandstetter, and S. Hochreiter. Hopfield networks is all you need. In ICLR, 2021.
15. Y. Wu, G. Wayne, A. Graves, and T. and Lillicrap. The Kanerva machine: A generative distributed memory. In ICLR, 2018.